STM probe on the surface electronic states of spin-orbit coupled materials

Author: Wenwen Zhou

Boston College

The Graduate School of Arts and Sciences

Department of Physics

STM PROBE ON THE SURFACE ELECTRONIC STATES OF SPIN-ORBIT COUPLED MATERIALS

a dissertation

by

WENWEN ZHOU

submitted in partial fulfillment of the requirements

for the degree of

Doctor of Philosophy

September 2014

STM probe on the surface electronic states of spin-orbit coupled materials

Wenwen Zhou

Dissertation advisor: Vidya Madhavan

Abstract

Spin-orbit coupling (SOC) is the interaction of an electron's intrinsic angular momentum (spin) with its orbital momentum. The strength of this interaction is proportional to Z^4 where Z is the atomic number, so generally it is stronger in atoms with higher atomic number, such as bismuth ($Z = 83$) and iridium ($Z = 77$). In materials composed of such heavy elements, the prominent SOC can be sufficient to modify the band structure of the system and lead to distinct phase of matter. In recent years, SOC has been demonstrated to play a critical role in determining the unusual properties of a variety of compounds. SOC associated materials with exotic electronic states have also provided a fertile platform for studying emergent phenomena as well as new physics. As a consequence, the research on these interesting materials with any insight into understanding the microscopic origin of their unique properties and complex phases is of great importance. In this context, we implement scanning tunneling microscopy (STM) and spectroscopy (STS) to explore the surface states (SS) of the two major categories of SOC involved materials, Bi-based topological insulators (TI) and Ir-based transition metal oxides (TMO). As a powerful tool in surface science which has achieved great success in wide variety of material fields, STM/STS is ideal to study the local density of states of the subject material with nanometer length scales and is able to offer detailed information about the surface electronic structure.

In the first part of this thesis, we report on the electronic band structures of three-dimensional TIs Bi_2Te_3 and Bi_2Se_3. Topological insulators are distinct quantum states of matter that have been intensely studied nowadays. Although they behave like ordinary insulators in showing fully gapped bulk bands, they host a topologically protected surface state consisting of two-dimensional massless Dirac fermions which exhibits metallic behavior. Indeed, this unique gapless surface state is a manifestation of the non-trivial topology of the bulk bands, which is recognized to own its existence to the strong SOC. In chapter 3, we utilize quasiparticle interference (QPI) approach to track the Dirac surface states on Bi_2Te_3 up to ~800 meV above the Dirac point. We discover a novel interference pattern at high energies, which probably originates from the impurity-induced spin-orbit scattering in this system that has not been experimentally detected to date. In chapter 4, we discuss the topological SS evolution in $(Bi_{1-x}In_x)_2Se_3$ series, by applying Landau quantization approach to extract the band dispersions on the surface for samples with different indium content. We propose that a topological phase transition may occur in this system when x reaches around 5%, with the experimental signature indicating a possible formation of gapped Dirac cone for the surface state at this doping.

In the second part of this thesis, we focus on investigating the electronic structure of the bilayer strontium iridate $Sr_3Ir_2O_7$. The correlated iridate compounds belong to another domain of SOC materials, where the electronic interaction is involved as well. Specifically, the unexpected Mott insulating state in 5*d*-TMO Sr_2IrO_4 and $Sr_3Ir_2O_7$ has been suggested originate from the cooperative interplay between the electronic correlations with the comparable SOC, and the latter is even considered as the driving force for the extraordinary ground state in these materials. In chapter 6, we carried out a comprehensive examination of the electronic phase transition from insulating to metallic in $Sr_3Ir_2O_7$ induced by chemical doping. We observe the

subatomic feature close to the insulator-to-metal transition in response with doping different carriers, and provide detailed studies about the local effect of dopants at particular sites on the electronic properties of the system.

Additionally, the basic experimental techniques are briefly described in chapter 1, and some background information of the subject materials are reviewed in chapter 2 and chapter 5, respectively.

Contents

Acknowledgements

First of all, I want to thank my advisor Professor Vidya Madhavan, for her constant help in developing the research ideas, teaching me important lessons on the process of scientific studies, as well as her ongoing guidance over the past five years.

I am also appreciative to my wonderful labmates in the STM group, Yoshinori Okada, Daniel Walkup and Ilija Zeljkovic. They were always willing to give me assistance in my laboratory experiments and I have benefited a great deal from my enlightening discussions with them.

I am thankful to Chetan Dhital, Zhensong Ren, Tom Hogan and Xiang Chen for providing me with nice single crystal samples. I give special thanks to Professor Stephen Wilson for his inspiring advice and suggestions related to my research.

I would like to express my gratitude to Dr. Hsin Lin and Professor Ying Ran as well, for their great theoretical ideas and cooperation.

I am grateful to Nancy Chevry for helping me deal with the relevant administrative issues. I also would like to thank Paul Dee in the machine shop and Richard Pijar in the electronics shop for their kind assistance with fixing my instruments.

I am very much indebted to my parents and my family, who gave me continuous support and encouragement to pursue my graduate study in the U.S. I owe my success of being able to attain a PhD in physics to them.

List of Figures

Chapter 1

Experimental techniques: scanning tunneling microscopy and spectroscopy

The scanning tunneling microscope (STM) was invented in 1982 by Gerd Binnig and Heinrich Rohrer [1][2], for which they won half of the 1986 Nobel Prize in physics. As a revolutionary technique, STM allowed the direct surface measurements of real space images down to the atomic level.

1.1 Tunneling theory

The key concept underlying STM is the phenomenon of quantum tunneling [3]. In quantum mechanics, a particle can traverse a potential barrier with less energy than required by the barrier, which is known as quantum tunneling or tunneling. The probability of such a process is of course very sensitive to the barrier thickness and is typically zero for barriers thicker than a few Angstroms. The scanning tunneling microscope, which is the focal experiment of this thesis, is an instrument which counts the quantum tunneling events by bringing a sharp conducting tip in a close proximity with a flat conducting sample.

When a bias voltage V is applied between the tip and sample, a tunneling current will flow through the vacuum barrier between them. By using time-dependent perturbation theory, this tunneling current can be expressed as

$$I \sim \int_{-eV}^{0} |M|^2 \rho_s(\varepsilon)\rho_t(\varepsilon + eV)(f(\varepsilon) - f(\varepsilon + eV))d\varepsilon \quad (1.1)$$

where $|M|^2$ is the matrix element for tunneling across the barrier, $\rho_s(\varepsilon)$ and $\rho_t(\varepsilon)$ are the density of states (DOS) of the sample and tip respectively, and $f(\varepsilon)$ is the Fermi-Dirac distribution

$$f(\varepsilon, T) = \frac{1}{1+\exp\left[(\varepsilon-\varepsilon_F)/k_B T\right]} \quad (1.2)$$

which has a small effect of thermal smearing with $\sim k_B T$ [4].

This calculation can be physically understood from the schematic sketch in figure 1.1. With a negative voltage $-V$ applied to the sample, the Fermi level of the sample electrons is effectively raised by eV with respect to the tip. At extremely low temperature, the elastic tunneling of electrons would only correspond to the range of energies, eV, encompassed by the displaced Fermi levels. The integral represents the number of available filled states of the sample and empty sates of the tip respectively for the tunneling process.

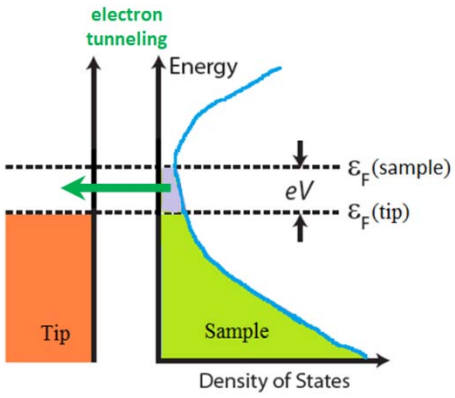

Figure 1.1: Schematic of the tunneling process between tip and sample. The sample Fermi level is effectively raised by eV with respect to the tip, by applying a bias voltage $-V$. Electrons

tunneling from the filled states of the sample to the empty states of the tip generate the tunneling current I.

We can choose a tip material which has a relatively flat DOS in this energy range, so that $\rho_t(\varepsilon)$ can be treated as a constant and taken out of the integral

$$I \sim \int_{-eV}^{0} |M|^2 \rho_s(\varepsilon) d\varepsilon \tag{1.3}$$

In practice, there are several suitable tip materials for this purpose. The data reported in this thesis were obtained with tungsten tips.

Bardeen first laid out a basic theory for vacuum tunneling in 1961 [5] and he showed that under the realistic assumption, the matrix element for tunneling is virtually independent of the energy difference between the two sides of the barrier. So to a reasonable approximation we can take it as a constant in the tunneling theory [6]. We can further describe the matrix element as an energy-independent square barrier under the WKB approximation [7][8],

$$|M|^2 = \exp\left(-2\frac{z}{\hbar}\sqrt{2m\phi}\right) \equiv \exp\left(-2\kappa z\right) \tag{1.4}$$

where m is the electron mass, z is the width of the barrier (tip-sample separation), and ϕ is the barrier height which is actually some mixture of the work functions of the tip and sample. The typical magnitude of ϕ is found to be around 3-4 eV.

In summary, the tunneling current can be reduced to

$$I \sim \exp\left(-2\kappa z\right) \int_{-eV}^{0} \rho_s(\varepsilon) d\varepsilon \tag{1.5}$$

It is exponentially sensitive to the distance between tip and sample, and linearly sensitive to the integral of the sample DOS from Fermi level to the bias energy. The former is in fact the key ingredient to the success of STM. With this exponential dependence of the tunneling current responding to the small changes in height, resolving and imaging atoms become feasible.

1.2 Measurement types

The standard operation mode of STM is as follows. The tip is attached to a piezo-tube scanner whose length can be regulated by a voltage V_Z applied between its inner and outer surfaces (figure 1.2). There are four quadrants $\pm X$ and $\pm Y$ on the outside and a single electrode for Z on the inside, which can control the tip motion in three directions with sub-Angstrom precision. In our experiments, the bias voltage is always applied on the sample and the tunneling current is measured from the tip. We also employ a feedback loop which controls V_Z to keep the tunneling current constant at a fixed bias voltage. The feedback loop takes the deviation of the tunneling current from the set-point current as an input and gives out appropriate V_Z that would compensate the error.

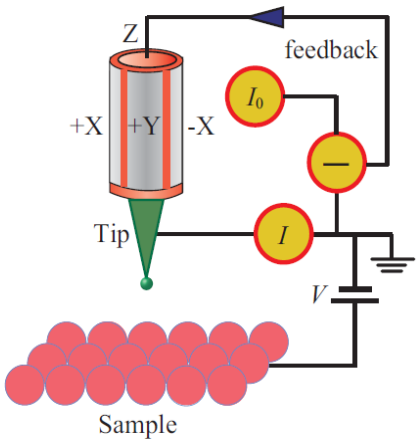

Figure 1.2: Schematic representation of an atomically sharp tip scanning at an atomically flat surface. Practically the atom situated closest to the sample contributes the most to the tunneling process. Tip is mounted on a piezo tube and it moves under the control of a constant current feedback loop.

Topography

A topographic image is obtained by measuring the magnitude of V_Z as a function of position (figure 1.3(a)). For a given bias voltage, the STM tip moves up and down across the sample surface in order to keep the current constant with the feedback loop. The relative variation of the tip height is taken as image variable in this mode. By recording the voltage on the Z piezo, one can effectively plot the z-motion of the tip and map the topography of the surface. In general routine, we obtain a good topographic image with atomic resolution as the first step when we approach on a new sample with a fresh tip in order to ensure the data quality.

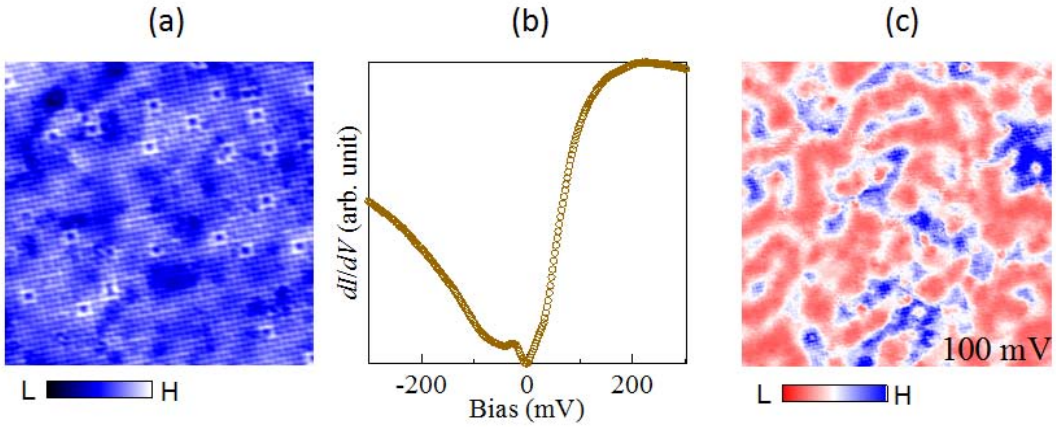

Figure 1.3: Typical ways of viewing STM measurement modes. (a) A topography acquired on $(Sr_{1-x}La_x)_3Ir_2O_7$ (x=0.04) showing the square lattice in 200 Å field-of-view, with $V = +300$ mV and $I =$

100 pA. (b) A $\mathrm{d}I/\mathrm{d}V$ spectrum taken on the clean spot in (a). (c) LDOS map at +100 mV over a 300 Å field-of-view.

$\mathbf{d}I/\mathbf{d}V$ spectrum

Using the STM in spectroscopy mode, we can also measure the differential conductance $\mathrm{d}I/\mathrm{d}V$ to get the local density of states (LDOS) of the sample in a given (x, y) location. From equation (1.5) we know that the tunneling current is proportional to the integrated LDOS if the tip sample separation z is constant,

$$I = I_0 \int_{-eV}^{0} \rho_s(\varepsilon) d\varepsilon \tag{1.6}$$

Therefore the derivative of the tunneling current with respect to the bias voltage will yield the LDOS,

$$\frac{\mathrm{d}I}{\mathrm{d}V} \propto \mathrm{LDOS}(eV) \tag{1.7}$$

In practice, a lock-in amplifier is used to measure $\mathrm{d}I/\mathrm{d}V$ directly. A voltage modulation $\mathrm{d}V$ is applied to the bias, and a resulting response in current modulation $\mathrm{d}I$ is measured at the same frequency. So by varying bias V one can map out an entire LDOS curve or so-called $\mathrm{d}I/\mathrm{d}V$ spectrum (figure 1.3(b)).

DOS map

Besides recording the spectrum at a single location, there is another way to represent the DOS which is more common and popular. Since we can control the (x, y) motion of the tip by using the piezo-tube scanner, we can get a series of LDOS-vs-energy curves at each point in the XY

plane ($\mathrm{d}I/\mathrm{d}V$-map), or a series of two-dimensional DOS maps at each energy eV (topo-map), as shown in figure 1.3(c). DOS maps (conductance maps) are very useful to visualize the spatial inhomogeneities for some materials, such as high-T_C superconductors [9][10] and 5*d*-iridate $Sr_3Ir_2O_7$ which will be discussed in Chapter 6.

Usually a detailed DOS map with both high spatial resolution and energy resolution will be desired in a STM experiment and it is the main type of data set in this thesis. We will also present some high quality line cuts which is the measurement of DOS spectra at equally spaced points along a straight line.

1.3 Quasiparticle interference and Landau quantization as *k*-space probes

In addition to its spatial and spectroscopic sensitivity, STM can also provide momentum space (*k*-space) information through two kinds of observed phenomena – quasiparticle interference (QPI) resulted from the scattering of electron waves by impurities and steps, and Landau quantization of the DOS in the presence of a magnetic field.

Quasiparticle interference

QPI arises due to the elastic scattering of electronic quasiparticles from a point impurity or step edge, and manifests as a standing wave pattern [11][12], which comes from the interference between incoming and outgoing waves associated with quasiparticle states (figure 1.4(a)).

The electrons in an ideal metal where the LDOS is homogeneous are described with Bloch states, $\Psi_{\mathbf{k}}(\mathbf{r}) = e^{i\mathbf{k}\mathbf{r}}u_{\mathbf{k}}(\mathbf{r})$. With impurities in the material, however, mixed Bloch states with the same energy at momenta $\mathbf{k}_i$ and $\mathbf{k}_f$ will lead to spatial variations in the form of interference patterns, with the periodicity $\lambda = 2\pi/\boldsymbol{q}$, $\boldsymbol{q} = \mathbf{k}_f(\varepsilon) - \mathbf{k}_i(\varepsilon)$. In theoretical model, the scattering intensity of $\boldsymbol{q}$ vector can be calculated from autocorrelation.

By imaging the standing wave patterns, STM can directly visualize the LDOS oscillations in the conductance maps (figure 1.4(b)). Furthermore, one can also measure the dispersion of $\boldsymbol{q}$ vectors as a function of energy. With consulting the constant energy contour (CEC) in *k*-space, this gives the information of the electronic band dispersion in the material studied (figure 1.4(c)). Therefore QPI approach can serve as an ideal complement to ARPES to explore the band structure.

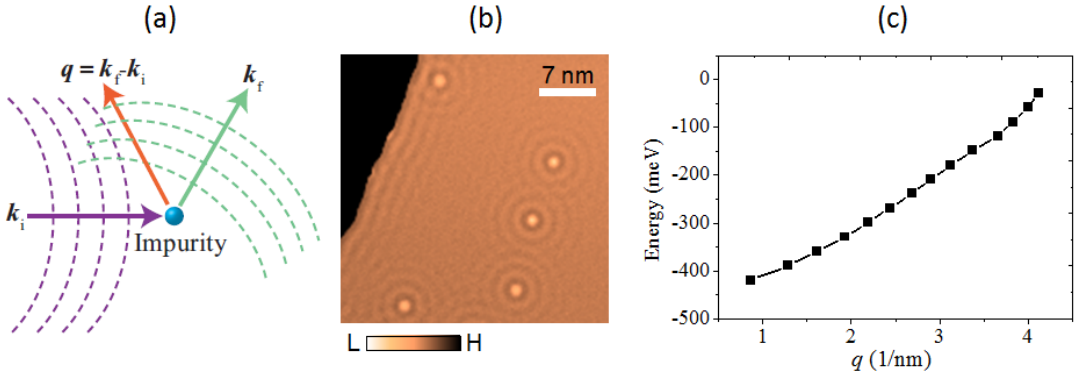

Figure 1.4: Quasiparticle interference induced by elastic scattering. (a) A cartoon illustration of QPI around a point impurity. (b) Standing wave patterns formed due to the quasiparticle scattering from impurities and steps, as observed in STM topography on Cu (111) surface. V = -100 mV and I = 800 pA. (c) The quasiparticle dispersion of Cu (111) calculated from catching the $\boldsymbol{q}$ vectors in Fourier space with different energy layers of conductance maps.

Landau quantization

In the semiclassical picture, electrons under magnetic field will experience the Lorentz force and their motions are described with circular cyclotron orbits [13]. The quantization of these cyclotron orbits are known as Landau levels (LLs). LLs of free fermions in 2D are equally spaced with energy separation $\hbar\omega_c$, where ω_c is the cyclotron frequency [14]. For 2D massless Dirac fermions, however, the linear energy-momentum dispersion leads to unequally spaced LLs with the 0th LL located at the Dirac point [15] (figure 1.5(a)).

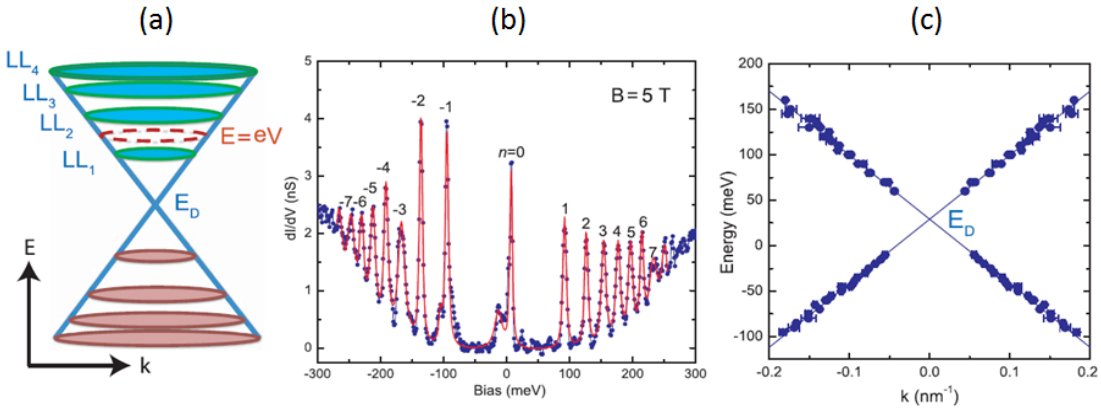

Figure 1.5: STM measurements of the Landau spectroscopy and 2D band structure in epitaxial graphene. (a) Schematic illustration of the quantized LLs in a magnetic field which correspond to closed CECs. The red dashed line indicates the energy at bias V in the $\mathrm{d}I/\mathrm{d}V$ measurement. (b) LL spectra measured at 5 T in multilayer graphene, with LL indices marked from 0 to $\pm$7. (c) The extracted energy-momentum dispersion (symmetrized about k=0) from gathering field dependent LL spectra. Adapted from [16].

In spectroscopic STM, LLs manifest as peaks in the $\mathrm{d}I/\mathrm{d}V$ spectra (figure 1.5(b)). According to the Bohr-Sommerfeld quantization condition, the area of the nth Landau orbit along the CEC in k-space is given by

$$A_n = \pi k_n^2 = (n + \gamma)\, 2\pi eB/\hbar \tag{1.8}$$

The phase factor γ is determined to be 1/2 for a conventional free electron and 0 for a Dirac fermion [17]. With specified n and B from a series of field-dependent LL spectra, we can acquire both the momenta k_n and the energy E_n of the nth LL. As a consequence, the energy-momentum dispersion relation can be extracted. The LL dispersion of graphene is plotted in figure 1.5(c) [16].

In real STM experiments, only a limited number of LLs can be possibly detected because of the intrinsic disorder in the materials. Landau quantization is sensitive to the defect scattering which will increase as the spatial extend of LLs increases, and is demonstrated to be largely suppressed with the presence of impurities [18].

1.4 STM setup

STM is a surface sensitive technique which requires clean and flat surfaces for effective study. To satisfy this, the sample is cleaved in ultra-high vacuum (UHV) environment with the vacuum better than 3E-10 Torr. Cleaving is a simple mechanical procedure. We glue a small piece of sample (1-2 mm) to the copper plate attached to the sample holder, and glue an aluminum rod to the other side of the sample. Then we load the sample holder into the system and just knock off the rod in the vacuum. Right after a successful cleavage, the sample is immediately inserted into the STM head which is at cryogenic temperature.

There are two STM systems at Boston College, a commercial one from Unisoku and a home-built one. These two systems share a lot in common. We will look into the basic instrumentation of our commercial STM system where the data in this thesis were taken from.

The design consists of a STM head with Pan style [19] walker, which employs a modified "stick-slip" coarse approach mechanism and has the ability to do in-situ tip and sample exchange (figure 1.6). The STM head is placed in a UHV can which is isolated by exchange gas serving as the thermal medium, and surrounded by a dewar equipped with a 7.5 T magnet.

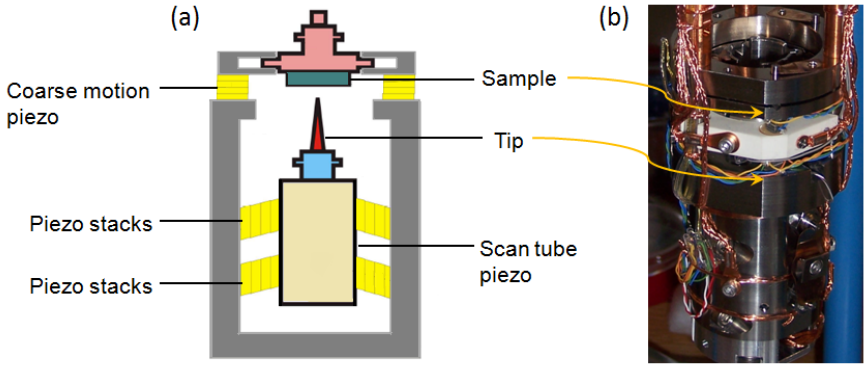

Figure 1.6: STM head with Pan style walker. (a) Schematic of the STM head with the in-situ exchangeable tip and sample fitted with Pan's configuration. (b) A photograph of the STM head used to perform the experiments described in this thesis.

Base temperature is around 4.5 Kelvin (liquid helium temperature) and it depends on the exchange gas pressure which is usually around 5E-2 Torr. The UHV is maintained by two ion pumps with two turbo pumps for initial evacuation, plus a cryo-pump which makes the pressure of STM head to be even better.

The cleaving unit is capable of both nitrogen temperature (cold) and room temperature (warm) cleaves. Compare to warm cleaving, cold cleaving has the advantage of lowering the atoms' mobility during and after the cleavage. This can improve the quality of the sample surface and has been proved necessary for some materials such as the iron pnictide and the iridate [20] which is one of the main topics in this thesis.

In addition, the commercial STM can be operated to run at variable temperatures. Temperatures below 4 K are achieved by continuously flowing liquid helium from the dewar into a 2K-pot which is designed for pumping down the helium vapor. Evacuating the exchange gas creates an isolated environment such that the STM can be cooled down to 2K without warming up by the outside dewar of atmospheric liquid helium.

The STM is controlled by the commercial controller and software which are products from RHK Technology. Another important component in STM electronics is a high-gain low-noise current pre-amplifier, which is utilized to convert the tunneling current (usually <1 nA) into voltage and amplify its magnitude.

Figure 1.7 and figure 1.8 are photos of the two STM systems in our lab. Both of them are located inside the sound proof rooms.

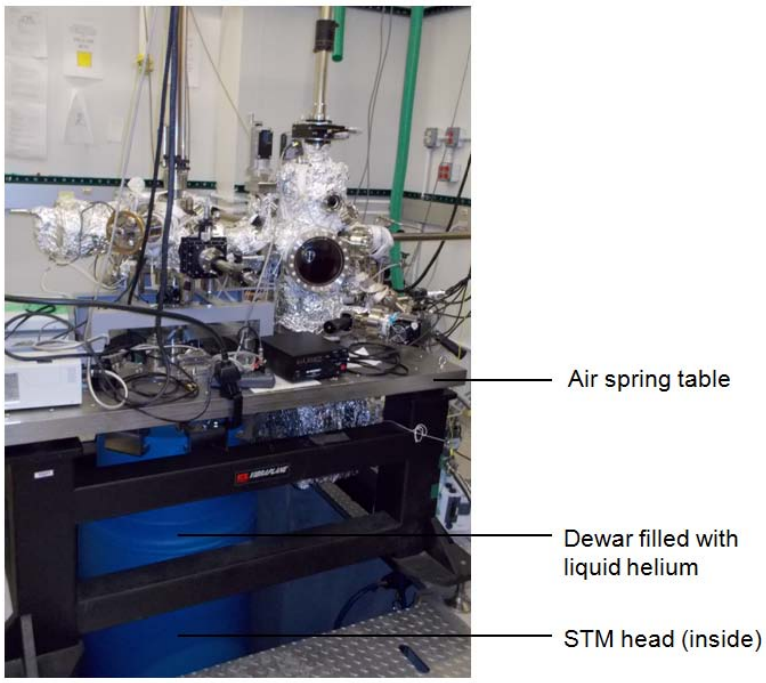

Figure 1.7: Photograph of the commercial STM system.

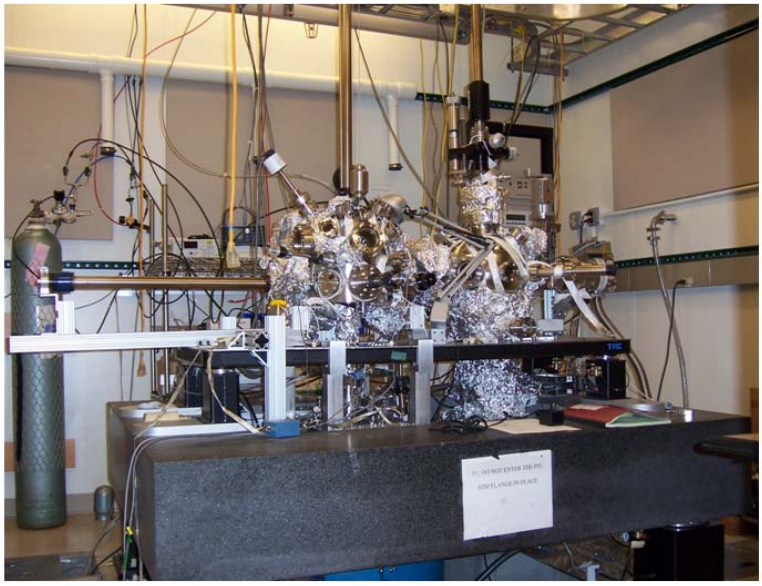

Figure 1.8: Photograph of the home-built STM system.

Chapter 2

Introduction to topological insulators

The search for new states of matter with distinctive order has been a constant theme and driving force in condensed matter physics. Before the 1980s, Landau's approach, which classifies states in terms of spontaneous symmetry breaking, was generally sufficient to model the macroscopic properties of phases and their continuous phase transitions in most systems. For example, a crystal breaks the continuous translation symmetry; a ferromagnet breaks the continuous rotation symmetry; and a superconductor breaks the local gauge symmetry [21]. Each of these broken symmetries is associated with a local order parameter, which is nonzero in an ordered phase but vanishes in a disordered phase [22].

However, with the discovery of integer [23] and fractional [24] quantum Hall effects in the 1980s, new phases of quantum matter, the "topological phases" were uncovered. These topological phases do not exhibit any broken symmetries or conventional order parameters [25]. They are different from the ordinary phases in the sense that some fundamental properties such as the quantized value of Hall conductance are invariant under smooth changes in material parameters until a quantum phase transition is reached.

2.1 Quantum Hall state

Quantum Hall (QH) state occurs when electrons confined to a 2D interface between two semiconductors are subjected to a strong magnetic field (figure 2.1(a)). In quantum mechanics, magnetic field makes the electrons experience the Lorentz force and the quantization of the electrons' cyclotron orbits leads to Landau levels with quantized energies.

However, a QH state is distinguished from a conventional insulator by the quantized Hall conductivity,

$$\sigma_{xy} = ne^2/h \tag{2.1}$$

with a high precision of 1 part in 10^9 [26]. This property is independent of the materials, geometry, or the microscopic details of the sample. Instead, it is actually a manifestation of the topological property of the band structure. We will see below that the integer n is connected to the topological nature of the QH state and is in fact a topological invariant which can be calculated from the microscopic properties of the system.

In the early 1980s Thouless, Kohmoto, Nightingale, and den Nijs (TKNN) proposed a deeper interpretation of QH effect in terms of the topology of the system [27]. In the TKNN theory, the gapped band insulators can be classified topologically by n, which is called the Chern number, to the equivalence classes that can be continuously deformed into one another without gap closing. The quantized Hall conductivity σ_{xy} is robust because the Chern number n is a topological invariant. Therefore systems characterized by different n are in different phases and cannot be

adiabatically connected, and n can only change at a phase transition point where the energy gap goes to zero.

By physically associating n with the Berry phase [28] and using $|u_m(\mathbf{k})\rangle$ as the m^{th} occupied bulk Bloch wavefunction, n is expressed as

$$n = \frac{1}{2\pi}\int_{BZ} d^2\,\mathbf{k}[\nabla_k \times \mathrm{A}(k_x, k_y)] \tag{2.2}$$

$$\mathrm{A} = \sum_{m=1}^{N}\langle u_m(\mathbf{k})|-i\nabla_k|u_m(\mathbf{k})\rangle \tag{2.3}$$

where N is the number of the occupied bands in the Brillouin zone. Thus the Hall conductivity is exclusively determined by the occupied bulk states.

On the other hand, a bulk property is manifested on the surface, which can be topologically classified by their genus g (number of holes). In this simple analogy, an orange has $g = 0$, whereas a bagel has $g = 1$. The chern number that distinguishes the two states ($n = 0$ in a trivial insulator and $n = 1$ in a QH state) is similar to the genus and analogously, it is impossible to deform the bagel into an orange without closing the hole.

The QH state features stable gapless conducting edge states [29], which is because of the skipping orbits of the electrons at the boundary of the system (figure 2.1(b)). This leads to electronic states that propagate along the edge in one direction only (termed “chiral”) and are localized in the presence of disorder given the fact that there are no backward moving modes. The existence of such chiral edge states is in turn related to the bulk topological invariant [30]. In this regard, the edge states are protected by the bulk topology. In practice, the

"dissipationless" transport by the edge states is of high interest for the anticipated future applications to solve the challenge of decoherence in quantum electronics.

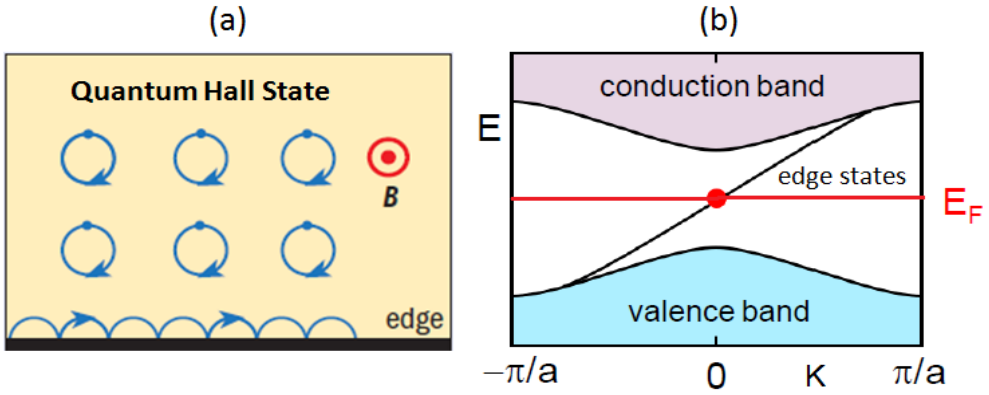

Figure 2.1: Quantum Hall state and gapless edge states. (a) Schematic representation of a quantum Hall state in real space. (b) The energy spectrum of the edge states as a function of momentum along the edge. Adapted from [30].

2.2 Quantum spin Hall state

In QH state, the non-zero Hall conductivity is induced with the presence of an external magnetic field. In 2005 Kane and Mere [25][31] and Bernevig and Zhang [32] theoretically predicted a new state of matter, the quantum spin Hall (QSH) state or 2D topological insulator (TI), in the absence of a magnetic field. In this new state, spin-orbit coupling (SOC), which is the interaction of electron's intrinsic spin with the orbital motion of the electrons, can behave like a magnetic field for the QH state. In other words, SOC is responsible for generating an effective spin-dependent "magnetic field", which is in the opposite direction for spin-up and spin-down electrons. Indeed a QSH state can be simply thought of as a superposition of two QH states that are time reversed partners of each other. In such a state the time reversal symmetry (TRS) is not

broken [31]. Time reversal invariance is preserved since applying the time reversal operator switches the direction of the magnetic field and flips the spin simultaneously.

Unlike the single chiral edge state in QH state, a QSH state consists of a pair of edge states moving in opposite directions and with opposite spins [31] (figure 2.2). The resulting edge states are termed "helical" [33], because spin is correlated with the direction of propagation. Although electrons are allowed to travel both forwards and backwards in this case, the backscattering is still suppressed as in the QH edge states but with more subtle reasons. An electron needs to flip its spin in order to backscatter, which requires the breaking of TRS. If time reversal invariance is preserved (with no magnetic impurities), back scattering is then prohibited. In this sense, the gapless edge states are protected by the TRS. As will be seen below, TRS also plays a fundamental role in guaranteeing the topological stability of these edge states and their robustness against disorder.

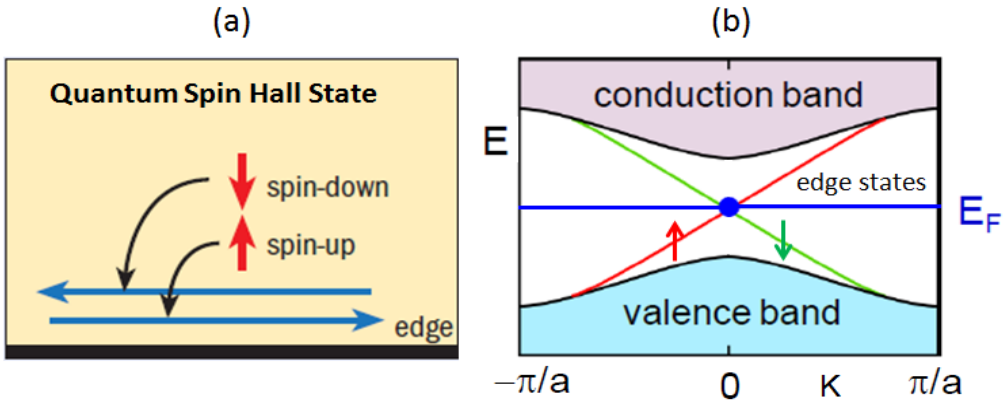

Figure 2.2: Quantum spin Hall state and gapless edge states. (a) Schematic representation of a quantum spin Hall state in real space. (b) The energy spectrum of the edge states as a function of momentum along the edge. Adapted from [30].

Since the spin-up and spin-down electrons cancel each other, the Hall conductance of the QSH state vanishes which means the Chern number $n = 0$. However, a new topological invariant was found to characterize such time reversal invariant band structures, which is valued in the $\mathbb{Z}_2$ group containing only two quantities, $\nu = 0$ or 1 [25]. This new invariant distinguishes the topologically nontrivial QSH insulator ($\nu = 1$) from the ordinary insulator ($\nu = 0$).

A physical intuition for the $\mathbb{Z}_2$ topological invariant can be understood via the notion of a Kramers pair of the edge states. Kramers' theorem is known as a fundamental property in quantum mechanics which states that all eigenstates of a time reversal invariant Hamiltonian are at least twofold degenerate [30]. The two edge states of a QSH insulator at momentum k and $-k$ form such a Kramers pair. Since the crystal is $2\pi/a$ periodic, momentum 0 and π/a are two special time reversal invariant momenta which are invariant under $k \to -k$. Kramers' theorem requires that the edge states must be twofold degenerate at $k = 0$ and $k = \pi/a$ (or $k = -\pi/a$) if they exist, whereas the SOC will split the degeneracy at other values of k. As a consequence, TRS will protect the edge states of a QSH insulator by assuring the two branches cross at a particular edge momentum $k = 0$ [25], and thereby guarantees the topological stability of the robust edge states.

As illustrated in figure 2.3, there are only two patterns of edge states that Kramers pair at $k = 0$ and $k = \pi/a$ can connect and these two patterns cannot deform into each other in the presence of TRS [34]. Case (a) occurs in a QSH insulator in which the edge states connect the conduction and valence band in a zigzag way. Here the edge states are robust and the bands intersect Fermi energy an odd number of times. Case (b) occurs in an ordinary insulator in which

the edge states connect pairwise. Here the edge states can be eliminated by pushing all of the bound states out of the gap and the bands intersect Fermi energy an even number of times. This is the physical origin of the $\mathbb{Z}_2$ topological invariant.

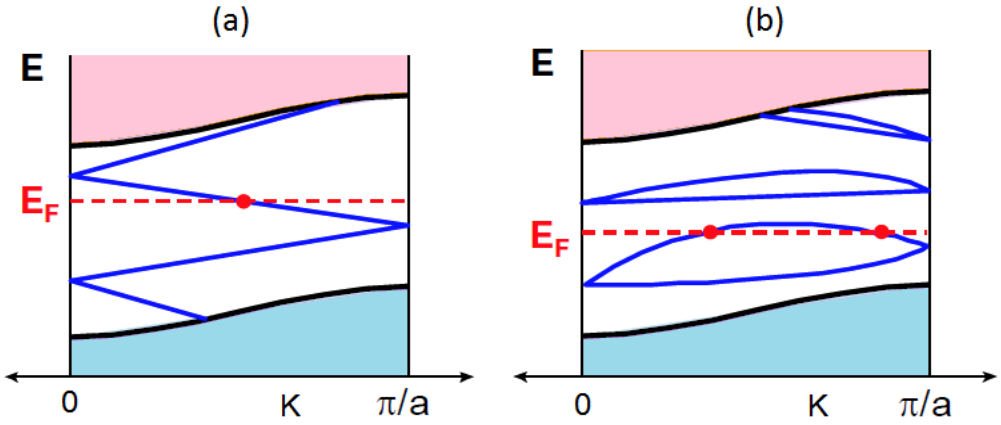

Figure 2.3: Schematic representation of the electronic dispersion connecting the Kramers pair at $k = 0$ and $k = \pi/a$ along the edge. (a) There is an odd number of crossings between edge states and the Fermi energy. (b) There is an even number of crossings. Adapted from [34].

2.3 Three dimensional topological insulators

An important theoretical development in 2006 was the discovery that the topological characterization of the QSH state has a natural generalization to three dimensions [34][35][36]. A 3D topological insulator has unique gapless states bound to the sample surface as a consequence of the topological order in the bulk [34]. These surface states strongly resemble the edge states of a 2D topological insulator. As in the 2D case, the direction of electron motion along the surface of a 3D TI is locked to the spin direction which now varies continuously (figure 2.4). The surface states of a 3D TI therefore form a unique 2D topological metal [37] which are like half of an ordinary 2D conductor since they are not spin degenerate as in an ordinary metal.

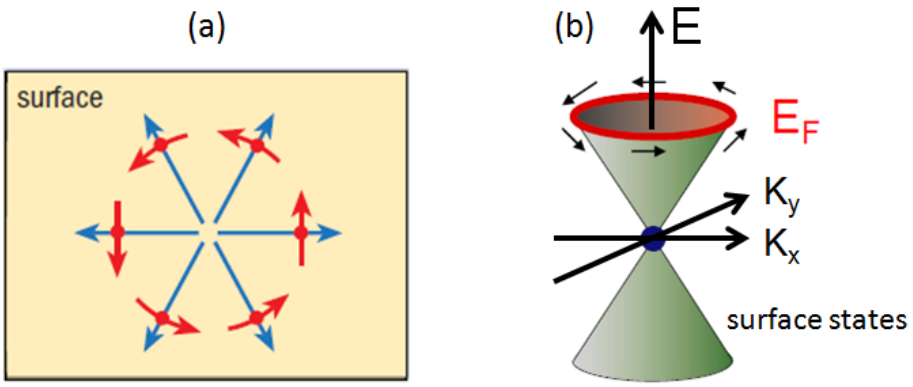

Figure 2.4: Surface states of a 3D topological insulator. (a) The surface of a 3D topological insulator with locked spin and momentum. (b) The 2D energy-momentum dispersion of the surface states forming a "Dirac cone" structure. Adapted from [38].

The 3D topological insulator is characterized by four $\mathbb{Z}_2$ topological invariants ν_0; $(\nu_1\nu_2\nu_3)$, and there are four independent time reversal invariant momenta $\Lambda_{1,2,3,4}$ in the surface Brillouin zone. The surface states must be Kramers degenerate at these special points, which as a result form 2D Dirac points in the surface band structure (figure 2.5(a)). Electrons in the surface bands of a topological insulator behave like 2D Dirac fermions and can be described by a 2D Dirac equation [34].

Now let's consider how the Kramers pairs at these four Dirac points Λ_i connect to each other. There are two ways of surface band connectivity just resemble figure 2.3, with the alternative determined by the four bulk $\mathbb{Z}_2$ invariants. The most important one among the four invariants, ν_0, identifies two distinct categories of topological insulators. When ν_0 is equal to 0, the system is a weak topological insulator with an even number of Dirac points enclosed by the surface Fermi arc (figure 2.5(b)). When ν_0 is equal to 1, the system is a strong topological insulator with

an odd number of Dirac points enclosed by the surface Fermi arc (figure 2.5(c)). In the simplest case the Fermi surface encloses one single Dirac point and this leads to a nontrivial π Berry phase. In fact, the π Berry phase, which protects electrons from being localized in the presence of disorder and may give rise to the weak antilocalization [39], is found to be a universal feature of the strong topological insulators. In this regard, the surface states are topologically protected against backscattering.

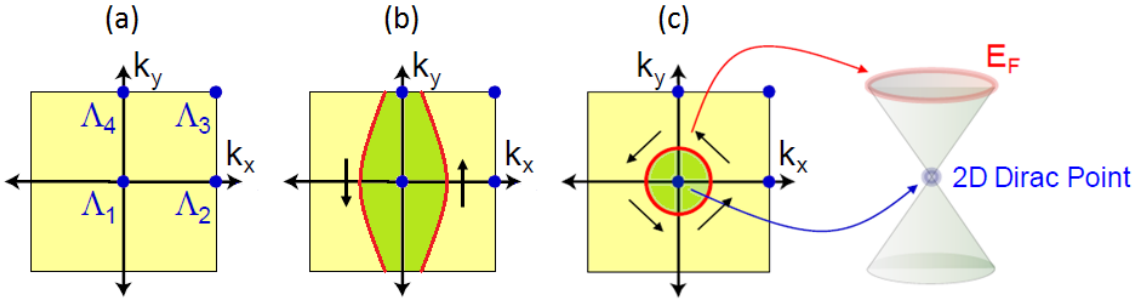

Figure 2.5: Strong topological insulator with a single Dirac cone. (a) The surface Brillouin zone of a 3D topological insulator with four time reversal invariant momenta Λ_i. (b) The surface Fermi arc in a weak topological insulator. (c) The surface Fermi arc in a strong topological insulator which encloses a single 2D Dirac point. Adapted from [37].

Although a 3D weak topological insulator can be formed by stacking layers of 2D QSH insulator, similar to a construction for 3D QH states [40], the resultant surface states are unstable to disorder. The reason is that a dislocation (a line-like defect in the crystal) will be associated with the 1D helical edge states [41]. However, a 3D strong topological insulator is not layered and is topologically nontrivial. It is this strong topological insulator that possesses protected metallic surfaces and has been the focus subject of experimental investigations.

To mathematically evaluate the value of $\mathbb{Z}_2$ topological invariants in both 2D and 3D topological insulators, Fu established a formula with the knowledge of the occupied Bloch wavefunctions [42]. In 3D systems, the $\mathbb{Z}_2$ invariant ν_0 is expressed by

$$(-1)^{\nu_0} = \prod_{i=1}^{8} \delta_i \tag{2.4}$$

The calculation can be simplified if the crystal has extra symmetry [37]. For instance, if the crystal has inversion symmetry, the computation of ν_0 can be reduce with

$$\delta_i = \prod_{m=1}^{N} \xi_{2m}(\Lambda_i) \tag{2.5}$$

where $\xi_{2m}(\Lambda_i) = \pm 1$ is the parity eigenvalue of the $2m^{th}$ band at Λ_i and the product is over the Kramers pairs of occupied bands. So with the presence of inversion symmetry, ν_0 can be determined by the parity of the occupied band eigenstates at the eight (or four in 2D cases) time reversal invariant momenta in Brillouin zone.

This parity approach has proven useful for identifying the candidate TI materials from band structure calculations. By applying this topological band theory to many real systems, Fu and Kane have predicted several candidates that may host strong topological insulating phases [37], and some of them were subsequently confirmed in experiments.

2.4 Experimental discovery

Topological insulators in both 2D and 3D are topological in the same sense as QSH effect, with topologically protected edge or surface states that result from strong SOC. Clearly, the search for topological insulator phases in real systems should be conducted in materials with

considerable SOC which can induce the band inversion, made from heavy elements. In 2006, Bernevig, Hughes and Zhang theoretically proposed that a QSH phase would be realized in CdTe/HgTe/CdTe quantum wells [43], with an inverted band structure existing in HgTe. Later this prediction was demonstrated by measuring the transport properties of such structures [44].

The first 3D topological insulator discovered experimentally was the semiconducting alloy bismuth antimonide $Bi_{1-x}Sb_x$ for a certain range of composition x, by the angle resolved photoemission spectroscopy (ARPES) [45]. ARPES uses high-energy photons to eject electrons from the sample, and the surface or bulk electronic structure as well as the spin polarization of the surface states can be directly determined by analyzing the energy, momentum and spin of the emitted electrons.

Bi is a semimetal with strong spin-orbit interactions and its band structure features an indirect negative gap with the overlap of conduction and valence bands (figure 2.6) [46]. At the L point, the valence and conduction bands are derived from antisymmetric (L_a) and symmetric orbitals (L_s) respectively, and the states near L are found to have a linear Dirac-like dispersion [47].

By substituting Bi with Sb in certain concentrations, the gap between L_a and L_s closes and reopens with an inverted symmetry ordering, and a massless 3D Dirac point is realized. There is no overlap between the valence band at T and the conduction band at L as in the pure Bi, and the material thus becomes an inverted band insulator.

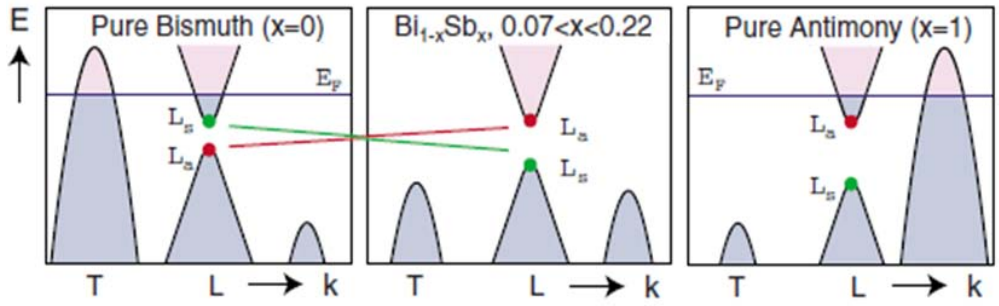

Figure 2.6: Schematic representation of the band structure of $Bi_{1-x}Sb_x$. The conduction band and valence band are inverted around x~0.04. Adapted from [30].

The Dirac-like band structure of $Bi_{0.9}Sb_{0.1}$ was established by ARPES experiments afterwards [45], with the observation of a bulk energy gap associated with the L point and several nondegenerate surface states that span the bulk gap (figure 2.7(a)). The demonstrated five surface band crossings (an odd number) between time reversal invariant points Γ and M indicates the topologically protected nature of these surface states and supports the strong topological insulator scenario in this material.

The topological property of this material is further confirmed by the measurements of the spin textures on the surface states [48], which provide the first direct evidence for the π Berry phase with the spin polarization rotating by 360° around the Fermi surface (figure 2.7(b)).

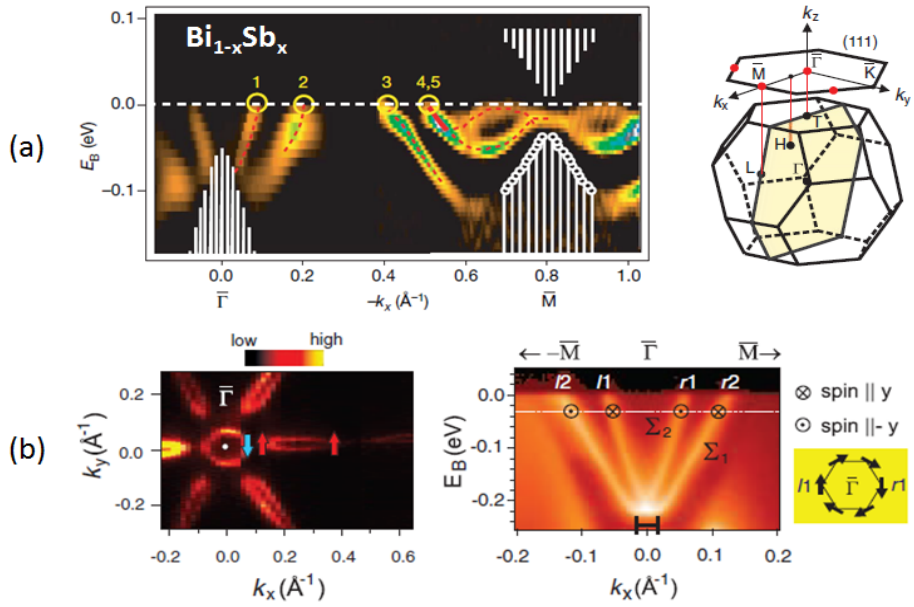

Figure 2.7: Topological surface states of $Bi_{0.9}Sb_{0.1}$ observed by ARPES. (a) ARPES data on the (111) surface of $Bi_{0.9}Sb_{0.1}$ shows that there are five Fermi crossings of the surface bands between the time reversal invariant points Γ and M, indicating that these surface states are topologically nontrivial. Shown in the right-hand diagram is a schematic of the bulk Brillouin zone and its (111) surface projection. Adapted from [45]. (b) Spin textures on the surface states of $Bi_{0.91}Sb_{0.09}$ at Fermi energy. A vortexlike pattern around Γ point is created by the spin chirality. Adapted from [48].

Besides ARPES, Scanning Tunneling Microscopy (STM) is another suitable tool to probe the topological character of the surface states in TIs. Distinct from trivial surface states, the topological surface states are expected to be robust in the presence of disorder since the TRS forbids the elastic backscattering between states of opposite momentum and opposite spin. STM study on the surface of $Bi_{0.92}Sb_{0.08}$ [49] has successfully demonstrated the absence of $\vec{\mathbf{k}}$ to $-\vec{\mathbf{k}}$ backscattering which suggests the chiral nature of the protected surface states (figure 2.8).

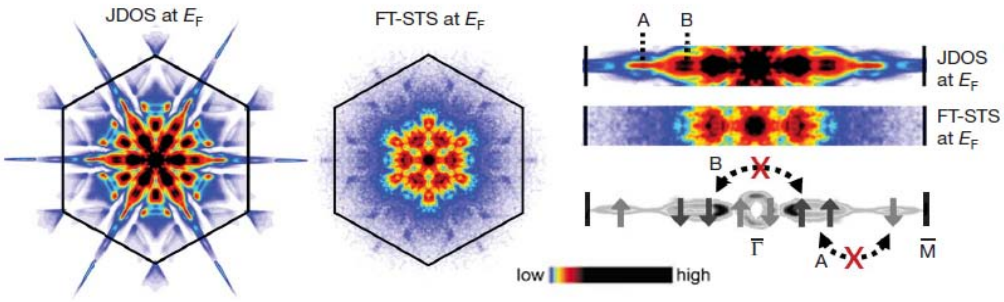

Figure 2.8: STM observations on the surface of $Bi_{0.92}Sb_{0.08}$ exhibiting the absence of backscattering. By comparing the quasiparticle interference patterns from joint density of states (JDOS) calculated from ARPES data and Fourier transform scanning tunneling spectroscopy (FT-STS) at Fermi energy along the Γ-M direction, it was discovered that the scattering which involves opposite spins and are present in JDOS are in fact absent in FT-STS. Adapted from [49].

However, the surface structure of the alloy $Bi_{1-x}Sb_x$ was found to be complex and the band gap was small. The search for better candidate materials for experiments has led to the discovery of the "second generation" of 3D topological insulators [38], typically bismuth selenide Bi_2Se_3 and bismuth telluride Bi_2Te_3 [50][51]. The new class of TI materials, which are well-known semiconductors with strong SOC, are able to exhibit topological insulator behavior at room temperature owing to the relatively large band gap of 0.35 eV and 0.18 eV respectively. They also feature the simplest possible surfaces state pattern with only one single Dirac cone on the surface. More details regarding to these two compounds will be discussed in Chapter 3 and Chapter 4.

Chapter 3

Visualizing the high-energy band structure in 3D topological insulator Bi_2Te_3

Topological insulators have surface states with unique spin texture. With impurities on the surface, the QPI caused by impurity scattering is an effective way to reveal the topological nature of the surface states in 3D TIs, which can be probed by STM. In this chapter, we use Fourier-transform scanning tunneling spectroscopy (FT-STS) to yield simultaneous real-space and momentum-space information in the topological insulator Bi_2Te_3. Particularly, we successfully follow the evolution of its Dirac surface states up to ~800 meV above the Dirac point, and discover a novel interference pattern at high energies, which probably originates from the impurity-induced spin-orbit scattering in this system that has not been experimentally detected to date.

3.1 3D Topological insulator Bi_2Te_3

3D topological insulator (TI) is a representative class of materials that exhibit topological phases and have a number of unusual optical, electrical, and magnetic properties [48][52][53][54][55][56]. The first 3D TI is $Bi_{1-x}Sb_x$ alloy [45], which was found to be with rather complicated surface structure and small band gap. A new family of 3D TIs including the semiconductors Bi_2Se_3 and Bi_2Te_3 were recently shown to have a larger band gap [57] and simpler surface spectrum with one single Dirac cone. The large band gap in Bi_2Se_3 and Bi_2Te_3

(approximately 0.35 eV [58] and 0.18 eV [59], respectively) guarantees their topological behavior at room temperature and zero magnetic field. Soon after the theoretical calculation which predicted the existence of single Dirac cone in these compounds [51], ARPES experiments observed the surface states (SS) with locked spin-momentum and the helical spin texture of the massless Dirac fermion in both Bi_2Se_3 and Bi_2Te_3 [60][50], thereby confirmed their topological band structures.

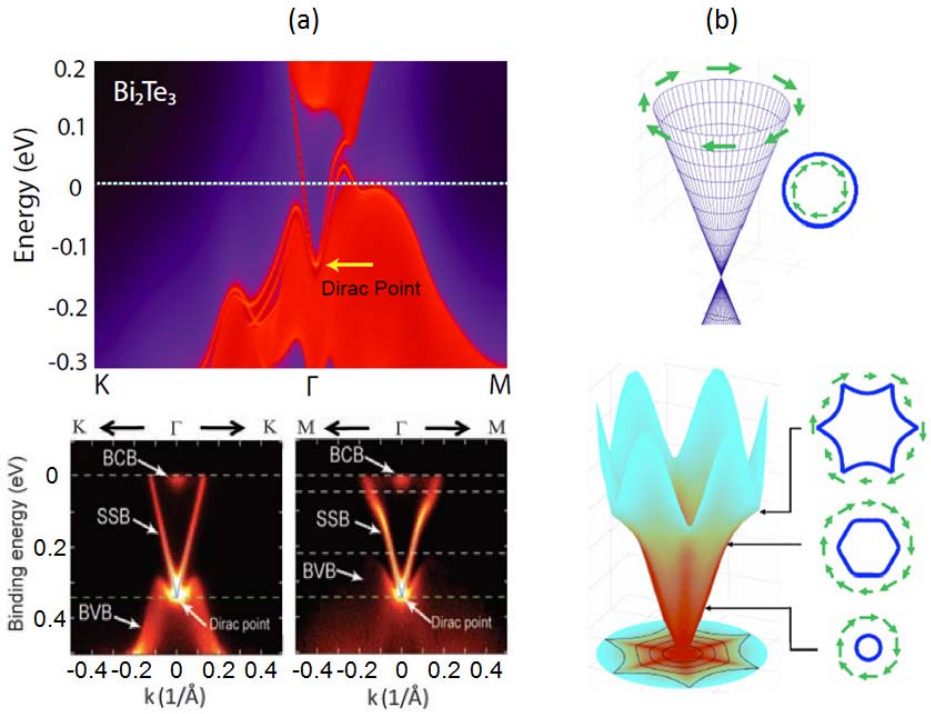

Figure 3.1: Dirac surface states on Bi_2Te_3. (a) Theoretical calculations of the electronic band structure in Bi_2Te_3 on its (111) surface, predicting the existence of simple SS consisting of a single Dirac cone at the Γ point. ARPES measurements of the surface band dispersions along Γ-K and Γ-M directions are shown in the lower panel. (b) Schematic of warped Dirac cone in Bi_2Te_3 obtained by first-principle computation and the corresponding constant energy surfaces evolving from circle to snowflake, compared to the simplest form of a Dirac cone with circular

Fermi surfaces only. Adapted from [51][60][61].

Bi_2Te_3 has a rhombohedral structure, in which Bi and Te atoms are stacked as quintuple layers in the sequence of Te(1)-Bi-Te(2)-Bi-Te(1) [62]. Since a band inversion occurs at the Γ point due to the strong SOC, Bi_2Te_3 is a strong topological insulator. In figure 3.1(a), ARPES experiments revealed the detailed surface electronic band dispersion in Bi_2Te_3 along the Γ-K and Γ-M directions. Although the SS in Bi_2Te_3 consist of only one single Dirac cone at the Γ point, the linear-dispersed surface band features a Dirac point buried inside the bulk valence band. Moreover, in Bi_2Te_3 the SS exhibit large deviations from the simplest form of a Dirac spectrum, with a hexagonal deformation as illustrated in figure 3.1(b). While the constant energy contour (CEC) of the SS is circular as close to the Dirac point, it displays a snowflake shape further away. This Fermi surface shape was explained with including a hexagonal warping term in the surface Hamiltonian, which can be connected with some surface properties in Bi_2Te_3 [61][63]. Previous STM studies have uncovered an enhanced LDOS oscillation as the CEC becomes non-convex, which was suggested to come from the hexagonal warping Fermi surface of Bi_2Te_3 [64][65][66]. All these pioneering works inspired much of the subsequent exploration on this material both in theory and experiment.

3.2 Challenge of understanding electronic structure in high-energy regime

While intensive ARPES and STM studies have been done on the gapless SS in multiple TI systems [60][50][67][68][49], and many of the fundamental properties such as the chiral spin texture, linear energy-momentum dispersion and the absence of backscattering have been well

demonstrated, some important questions remain. One question for instance is the effect of bulk-surface interaction on the SS properties in terms of electron lifetime and dispersion. Such effect of interaction between the bulk and surface bands provides important information to completely understand the unique SS in TIs. However, the evolution of the SS dispersion far from the Dirac point, at energies where the bulk bands coexist with the surface state bands, is still poorly investigated.

Although the SS dispersion and the observed quasiparticle scattering might be affected by the proximity or the hybridization with the bulk bands, the experimental confirmation is still lacking, in part due to the limitations of ARPES which is exclusively restricted to studying the occupied electronic states. Since STM has unrestricted access to the electronic states across the Fermi level, it can provide more comprehensive determinations of the SS dispersion in wide energy range, which would not only serve as a vital complement to ARPES data, but also be indispensible to explore the high energy electronic structures in TI materials.

3.3 Surface sates of Bi_2Te_3

Single crystals of $(Bi_{1-x}Fe_x)_2Te_3$ with x=0 (pristine Bi_2Te_3) and x=0.25% (Fe-Bi_2Te_3) were grown via a modified Bridgman technique. Samples were cleaved in UHV at room temperature and then immediately inserted into the cold STM head where data were obtained at ~4.5 K. STM measurements were carried out with chemically etched tungsten tips annealed at high temperature in the vacuum chamber.

Bi_2Te_3 naturally cleaves between adjacent quintuplet layers along the (111) direction, to expose a triangular lattice of Te atoms seen in STM topographs (figure 3.2(a)). This surface exhibits two main types of defects (figure 3.2(b)): triangular depressions and circular shallow protrusions which could be attributed as electron-donor impurities [69][70] with unknown origin. We note that since the impurity shapes in the topograph of Fe-Bi_2Te_3 were also visible in that of pristine Bi_2Te_3, we were not able to clearly distinguish the signature of Fe-dopants. However, based on the position of the impurities, Te vacancies and Bi anti-site defects could be potentially assigned [69].

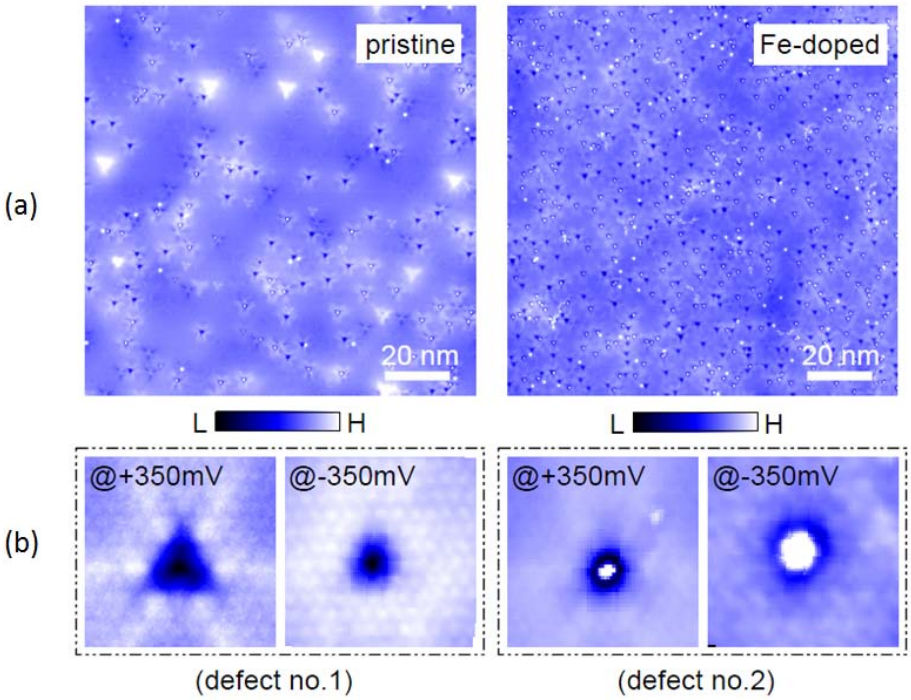

Figure 3.2: Topographs on the surface of pristine Bi_2Te_3 and Fe-doped Bi_2Te_3. (a) Topographic images of the pristine and Fe-doped Bi_2Te_3 samples, mostly showing the same species of impurities but with different densities. Bias voltages were set to be V_B=280 mV for pristine Bi_2Te_3 and V_B=300 mV for Fe-Bi_2Te_3. (b) Zoomed-in topographs for two major common defects observed in (a) acquired under opposite bias polarity (+350 mV and -350 mV respectively).

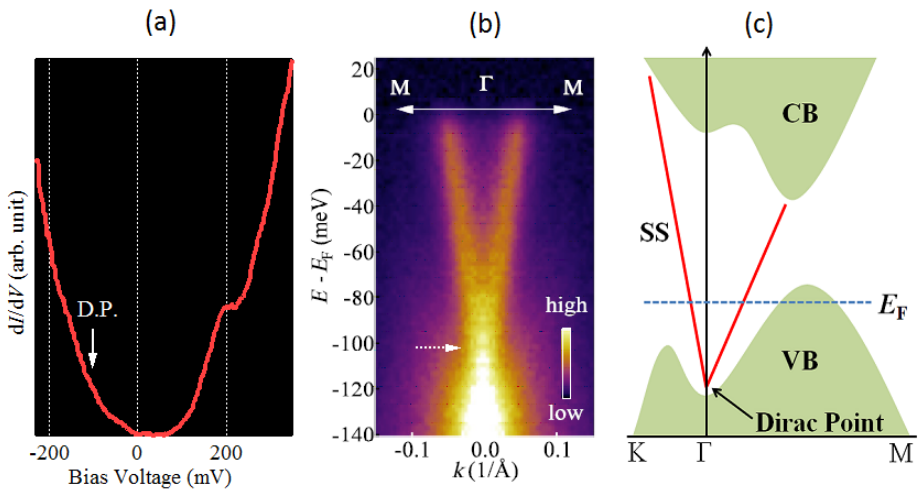

Figure 3.3: Surface density of states of Fe-doped Bi_2Te_3. Spatially averaged spectrum on the surface of Fe-Bi_2Te_3 is plotted in (a). The position of the Dirac point is indicated by an arrow, determined from the ARPES measurements on the same batch of samples shown in (b). Schematic of the bulk bands as well as the SS band in (c) agrees well with our STM data, including the conduction band minima corresponding to the observed shoulder feature in (a).

We investigate the SS of Bi_2Te_3 by STS, to detect electron density of states with using a lock-in amplifier. The d*I*/d*V* differential conductance spectrum, which reflects the LDOS arising from the surface projection of the bulk bands as well as the Dirac SS, is shown in figure 3.3(a). In contrast to some other topological materials where the Dirac point is visible as a spectral minimum [71][72], the Dirac point in Bi_2Te_3 is located below the top of bulk valence band (figure 3.3(c)), therefore is not evident in a d*I*/d*V* spectrum. According to ARPES measurements on the same batch of samples (figure 3.3(b)), we estimate the position of the Dirac point in Fe-Bi_2Te_3 to be approximately 105±15 meV below the Fermi energy [73]. As we will show later, this extrapolation is indeed consistent with our QPI dispersion. Besides this, we find a minimum in

the d*I*/d*V* spectrum close to the valence band maxima and a van Hove feature above the Fermi energy at higher energy associated with the bottom of the conduction band at the Γ point.

3.4 QPI approach on Bi_2Te_3

We track the evolution of Dirac SS in Bi_2Te_3 by mapping the QPI signatures over a significantly wide energy range, and utilize 2D Fourier transforms (FTs) to extract the electronic band structure. The trick of QPI analysis is to take advantage of scattering, which leads to interference patterns in the density of states that can be visualized by scanning tunneling microscopy and spectroscopy. By Fourier transforming the real-space interference patterns, we can access the momentum-space (*k*-space) information in the sample.

The electron-like excitations of a Fermi liquid or a superconductor are called quasiparticles [74]. The standing waves generated by the interference of incoming and outgoing electron waves scattered by surface steps and single defects is called the Friedel oscillations [75]. The physical origin of the QPI pattern in the constant-current STM images is the same as that of Friedel oscillations of electrons in the vicinity of a scatter. The oscillations can be imaged by STM as spatial modulations of local density of states (g(r,E)). In practice, the LDOS modulations are not very strong and are mostly imposed on a background with inhomogeneous LDOS, requiring g(r,E) maps to be taken over large fields of view (>45nm) [76] for sufficient momentum resolution.

The period of these oscillations is a function of the energy relative to the Fermi energy of the sample, which can be tuned in STM experiments with applying different bias voltages. In the FT

image at certain energy, intensity spots will appear that correspond to the scattering vectors q (2π/T). By measuring the wavelengths of the conductance modulations as a function of energy, and using the k-space symmetries of the band structure (as determined by ARPES), we are able to trace back to a quantitative map of the CECs. So the electronic properties of the SS including the information about dispersion can be inferred through the analysis of interference patterns of the electron waves near defects or steps. Indeed, FT-QPI imaging has been successfully applied to many complex systems, from simple metals [11][12], high-temperature superconductors [77][78], heavy-fermion compounds [79], to more recent topological materials [64][65][49][80].

The SS of TI materials Bi_2Te_3 and Bi_2Se_3 can be described by the effective Dirac Hamiltonian $H_0 = \hbar v \hat{z} \cdot (\sigma \times k)$ [with the momentum $k = (k_x, k_y)$] when the Fermi level is close to the Dirac point, which behaves like a massless Dirac fermion with the spin locked to its momentum [81]. However, in Bi_2Te_3, the hexagonal warping makes the CEC of the surface band evolving from a convex circle to a concave hexagon as the energy moves away from the Dirac point. Although the topological property of the SS is not altered, such kinds of CEC deformation do affect the behavior of the SS related to impurity scatterings [82]. As known, the TRS in single Dirac cone TI systems prohibits the dominant backscattering wave vector and thus makes any observation of QPI challenging. Still, the SS warping effect in Bi_2Te_3 can enhance the scattering channels and facilitate the observation of QPI. However, no study to date has been reported on the SS at energies higher than ~600 meV above the Dirac point, so the evolution of the QPI mode in this energy range is still unknown.

3.5 High-energy QPI probed by FT-STS

To map the electronic band structure of this material, we acquire energy-dependent d*I*/d*V* conductance maps over large, atomic flat regions of the pristine Bi_2Te_3 and Fe-Bi_2Te_3 samples. First of all, let's look at one single layer of the 3D conductance maps in low energy regime (300 meV), as shown in figure 3.4(a). The spatial modulation as a result of the quasiparticle scattering by impurities forms hexagonal patterns, and the magnitude is determined by the momentum transfer at this given energy. The QPI patterns are expected to be anisotropic as a consequence of warped CEC in Bi_2Te_3. To obtain the scattering wave vectors (*q*-vectors), we apply two-dimensional Fourier transformation to the d*I*/d*V* map. FT of the simultaneous topograph on the same sample surface exhibits the hexagonal lattice and specifies the high-symmetry directions in *k*-space as well (figure 3.4(b)). On the other hand, the most prominent feature in FT image of the d*I*/d*V* map, which captures *q*-vector connecting different points of the CEC, is the six-fold pattern with intensities centered along the Γ-M direction. Similar *q*-vectors have been previously observed by other STM groups [64][65]. Notice that all the *k*-space figures we present henceforth were rotated such that Γ-M is along the horizontal axis.

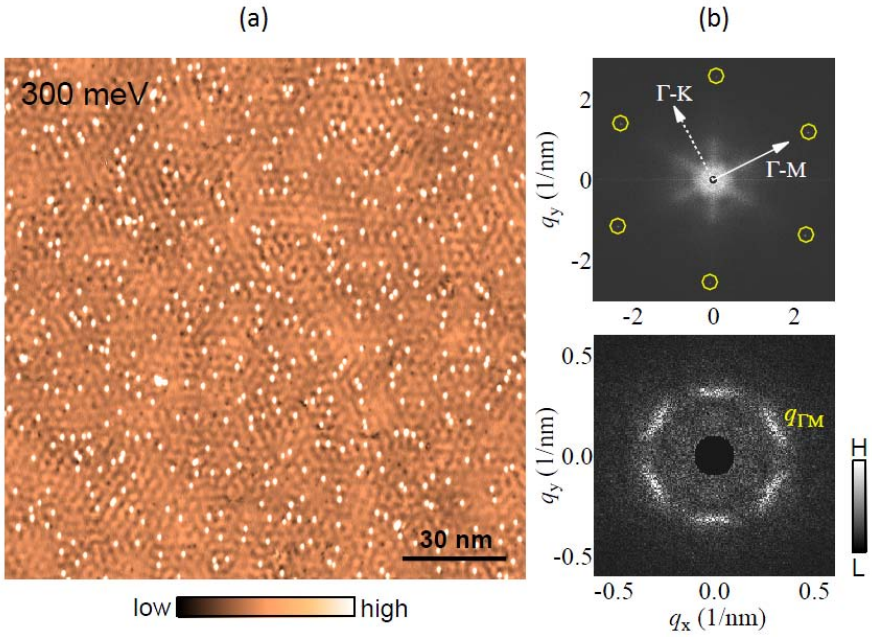

Figure 3.4: Interference patterns on Bi_2Te_3 at low energy. (a) Conductance map obtained within large field of view at energy 300 meV showing clear LDOS modulations centered at impurities. (b) FT image of (a) (lower) and FT image of the topograph on the same surface as (a) (upper). In the latter, Bragg peaks (marked with yellow open circles) indicating a hexagonal lattice structure of the sample are resolved, which also determines the high-symmetry directions Γ-M and Γ-K. A six-fold QPI pattern is visible in the lower FT image and we can identify it as $q_{\Gamma M}$ (q-vectors along the Γ-M direction).

Remarkably, as we go to higher energies, we discover a pronounced change in the QPI pattern. The dispersive QPI mode along the Γ-M direction gradually gets broader, and subsequently, at about 700 meV above the Dirac point, a secondary peak clearly emerges (figure 3.5). In addition, we also begin to see well-defined intensity along the Γ-K direction. By comparing figure 3.5(a) for Fe-Bi_2Te_3 and figure 3.5(b) for pristine Bi_2Te_3, we see that both samples demonstrate qualitatively similar patterns at higher energies. We emphasize here that the Dirac point of the

pristine Bi_2Te_3 sample is estimated to be around 60 meV below the Fermi energy, speculated from its d*I*/d*V* spectra combined with ARPES data. We will discuss the origin and implications of these emergent phenomena in the following paragraphs.

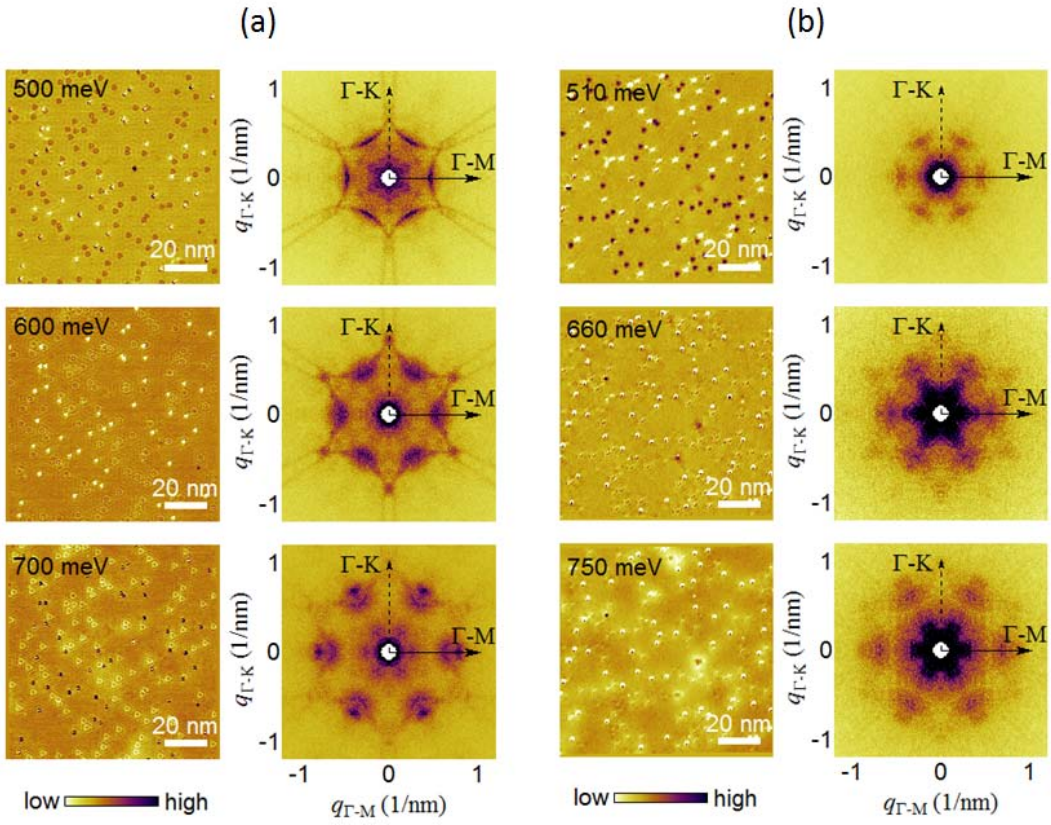

Figure 3.5: Interference patterns on Bi_2Te_3 at higher energies with new scattering channels emerging. Conductance maps for Fe-doped Bi_2Te_3 (a) and pristine Bi_2Te_3 (b) exhibit evident interference fringes at various energies. The corresponding hexagonally symmetrized Fourier transformation images show qualitatively similar QPI patterns emerging at higher energies from ~700 meV above the Dirac point. Here the Dirac point energy is estimated to be around 100 meV and 60 meV below the Fermi level, for Fe-doped Bi_2Te_3 and pristine Bi_2Te_3 samples, respectively.

We begin by plotting the dispersion of the *q*-vectors obtained from FTs along the two high symmetry directions Γ-M and Γ-K (figure 3.6). Along the Γ-M direction, the dispersion has a constant slope at low energies, which eventually deviates at higher energies, accompanied by weaker intensities of the *q*-vectors. ARPES studies indicate that at about 300 meV above the Dirac point, the SS along Γ-M starts to merge into the bulk conduction bands [60]. However, in principle the SS along Γ-M could potentially survive as a surface resonance even beyond these energies. In our data, the contours of FT reflect the topology of the CECs in momentum space. We find that the FT pattern, both in terms of magnitude as well as shape, remains similar to that at lower energies up to approximately 600 meV above the Dirac point, implying a sustained persistence of the SS along Γ-M despite the mixing with the bulk bands. Though, the intensity of the signal in FT shows a steep drop between 300 meV and 400 meV indicating a broadening of the SS, which is consistent with their transformation into a surface resonance due to encroachment of the bulk bands. Along the Γ-K direction, dispersing QPI mode emerges from ~500 meV. One possible factor for this phenomenon is that at high energies where the surface resonance along Γ-M has completely merged into the bulk states, the SS along Γ-K having just entered the conduction bands still continues to survive as a resonance.

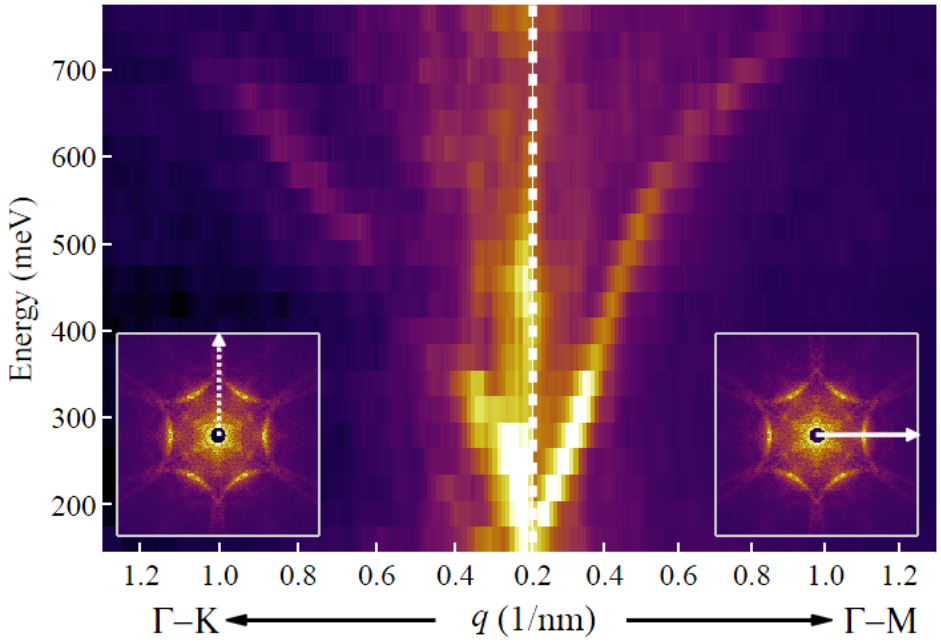

Figure 3.6: Intensity profiles of the FTs (line cuts of FTs along the specified directions, represented as color intensity). This plot displays the evolution of *q*-vectors as a function of energy along Γ-M and Γ-K directions. The slope deviation of the dispersion as well as the intensity drop of the *q*-vector at higher energies might be induced by the encroachment of the bulk bands.

Now we discuss the possible scattering processes at low energies based on the CECs in the reciprocal space. According to scattering geometry, scattering is dominated by the *q*-vectors which connect different points on the CECs with extremal curvatures. In general, the points of extremal curvatures are divided into two groups, arising from the "valleys" (positive curvature) and "tips" (negative curvature) [83]. With strong warping effects, the CEC morphology of Bi_2Te_3 gradually changes from a hexagon to a concave hexagram which appears as distorted snowflake, as energy increases. In the snowflake regime, the scattering processes in the high symmetry

directions may be captured by six sets of q-vectors [66], which connect the stationary points in k-space as labeled by q_1-q_6 in figure 3.7. We note that the backscattering wave vectors (q_5 along Γ-K and q_3 along Γ-M) are prohibited in pristine Bi_2Te_3 because of the time-reversal invariance.

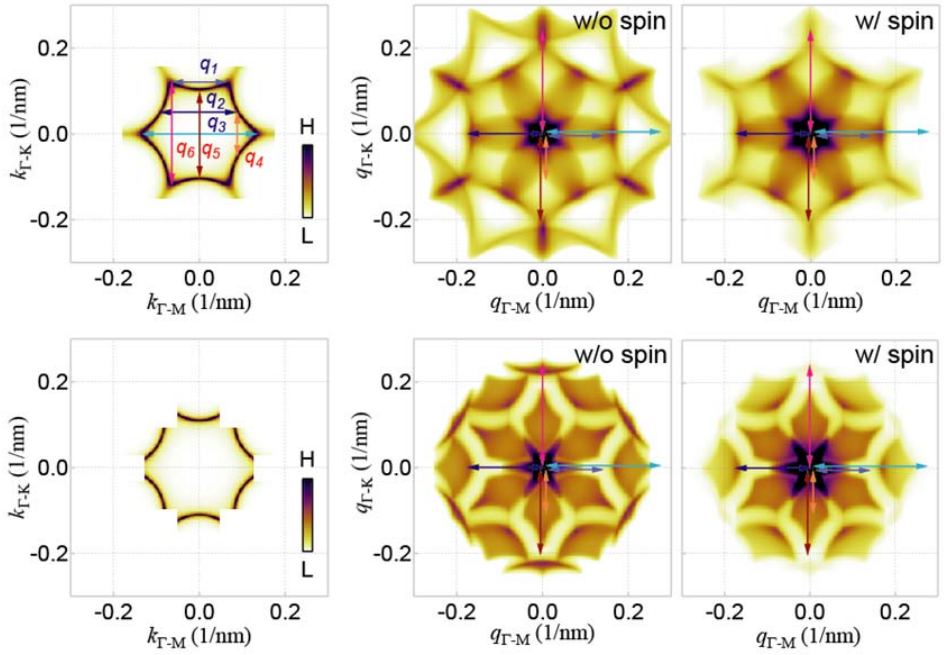

Figure 3.7: Theoretical calculations of the interference patterns. Simulated CECs at a selected energy of 300 meV above the Dirac point are plotted in the first column, without (upper) and with (lower) masking the "tip" intensities along Γ-M. The tight binding band parameters for the CECs were obtained by fitting to ARPES data [60]. Six dominant scattering channels (q_1-q_6) are indicated by arrows. The interference patterns from auto-correlation calculations without and with including the spin-sensitive matrix element are illustrated in the second and third column respectively. The resultant QPI signatures corresponding to the typical scatterings are marked by arrows as well.

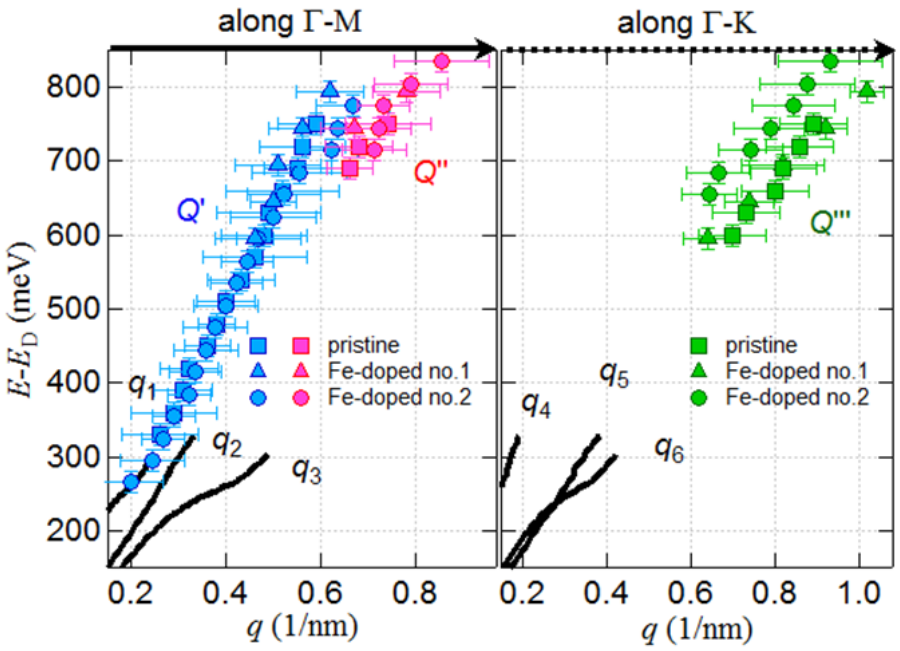

Figure 3.8: Comparison of STM results with ARPES data. Energy dispersions for three characteristic scattering channels from STM data, *Q*', *Q*" along the Γ-M direction and *Q*"' along the Γ-K direction, are plotted. Y-axis is the energy with respect to the Dirac point for each sample. Here we used two different datasets for Fe-doped Bi_2Te_3 samples (dataset no.1 is the one used in figure 3.5). Typical scattering channels (q_1-q_6) defined in figure 3.7 are plotted as well, as a comparison to STM observations. At higher energies, two-component wave vector *Q*' and *Q*" along Γ-M seem to match q_1 and q_2, respectively. Also appeared from 600 meV is the wave vector *Q*"' along Γ-K, which looks close to q_5.

Next we compare the *q*-vectors in STM data with those expected from the CECs obtained from previous ARPES measurements [60][84]. At low energies, the most intense signal in the FTs is along Γ-M. Although this *q*-vector may be associated with either q_1 or q_2, the observation of q_1 is more likely as it represents scattering between CEC regions with higher density of states. In

specific, the weight of q_1 is larger than those of q_2 since the tip points have larger DOS than the valley points, resulting in the even stronger features observed for q_1. Actually q_1 is enhanced at the stationary points of the distorted snowflake CECs [63] and therefore serves as nested set of vectors. Moreover from our previous analysis [73], the discovery of multiple *q*-vectors (along Γ-M and Γ-K) imposes strong constraints such that we are able to unambiguously identify the Γ-M scattering channel as q_1.

We further compare our high-resolution FT data to ARPES results quantitatively, to have a deeper insight into the momentum-space origins of the STM scattering vectors especially those emergent in the higher energy region. We access the ARPES extracted dispersions of the surface state bands for Bi_2Te_3 in the Γ-M and Γ-K directions to calculate the *q*-vectors as a function of energy. Illustrated in figure 3.8 are the resulting ARPES determined dispersions of q_1-q_6 overlaid with the STM data which are shifted rigidly in terms of the Dirac point energy E_D. We find that both slope and magnitude of the simultaneous wave vectors strongly constrain the fit between STM and ARPES, and thus decide conversely the position of Dirac point for pristine Bi_2Te_3 and Fe-Bi_2Te_3 samples respectively.

The agreement of STM and ARPES is quite evident, with good match of low-energy wave vectors *Q* to q_1 along Γ-M. Interestingly, the pattern of FT changes at higher energies. As seen in figure 3.5, at ~700 meV above the Dirac point we detect the appearance of a second *q*-vector along the Γ-M direction. Extrapolating from the low energy dispersion in figure 3.8, we notice that the magnitude of the high-energy wave vectors *Q* moves gradually from q_1 toward q_2. A natural explanation for this shift is that it is a consequence of the suppression of q_1 due to mixing with

the bulk bands. More precisely, according to ARPES measurements [64], the “tips” of the snowflake CEC become increasingly ill-defined at higher energies as the SS enter the bulk bands (figure 3.7), which as a result weakens the q_1 scattering channel but enhance other nearby scatterings such as q_2. In this sense, the drifting of wave vectors from q_1 to q_2 can be possibly understood with consulting the evolution of CECs. Nevertheless, this scenario does not easily catch the splitting of the Γ-M vector into two *q*-vectors. Besides, as displayed in figure 3.5, the appearance of the two *q*-vectors along Γ-M is accompanied by the surprisingly appearance of a scattering channel along Γ-K, whose magnitude is similar to q_5 (figure 3.8). The question now arises is whether the scenario used to explain the transition from q_1 to q_2 can interpret the appearance of this wave vectors *Q* along Γ-K as well. To find the answer, we need to refer to the theoretical calculations.

3.6 Theoretical model and QPI computation on Bi_2Te_3

We simulate the potential interference patterns at a constant energy (300 meV above the Dirac point) by a cross-correlation analysis. The spin-dependent scattering probability

$$P(q) = \int_k A(k)T(q,k)A(k+q)dk \tag{3.1}$$

is used for this calculation, where $A(k)$ is the spectral weight and $T(q,k)$ is a scattering matrix element. We consider a matrix element of the form $T(q,k) = |\langle\phi(k)|\phi(k+q)\rangle|^2$, where ϕ is the eigenfunction obtained in a $\boldsymbol{k}\cdot\boldsymbol{p}$ model [63] with two components (spin up and spin down). This matrix element is spin selective, which leads to a complete suppression of the scattering when the spins of the two states are opposite. Demonstrated in figure 3.7 are the interference

patterns with (third column) and without (second column) including such spin-sensitive matrix element. As seen, at low energies, the cross-correlation including the spin texture successfully captures the main features of our FTs. At high energies, however, the cross-correlation images almost entirely fail to match the FT patterns we observed.

Instead, there is another possible explanation for our data, which is suggested by a theoretical study of the STM interference patterns in Bi_2Te_3 [83]. Through a standard T-matrix formalism, the calculated QPI with considering the additional impurity induced spin-orbit scattering process is remarkably similar to our observations. Moreover, it is particularly striking that this spin-orbit scattering has a tendency to enhance the scattering between quasiparticles with large momenta, which implies that the effect of this additional term on the QPI pattern is expected to be more prominent at higher energies. This is completely consistent with the trends in our data.

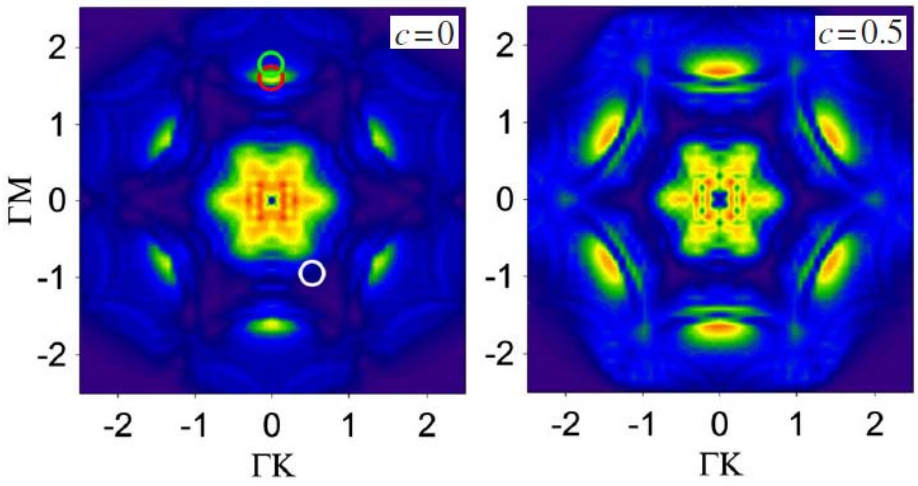

Figure 3.9: Calculated QPI images in Bi_2Te_3 at large momenta without (c=0) and with (c=0.5) including the additional spin-orbit scattering term. In the case of c=0.5, new QPI pattern appears exhibiting prominent features similar to our observations at higher energies, including the splitting q-vectors along Γ-M and the dot-shaped q-vector along Γ-K. Adapted from [83].

The surface Dirac cone in Bi_2Te_3 has the Hamiltonian that can be described by the $\boldsymbol{k}\cdot\boldsymbol{p}$ model

$$H(\vec{k}) = \frac{k^2}{2m^*} + v(1+\alpha k^2)\left(k_x\sigma_y - k_y\sigma_x\right) + \frac{\lambda}{2}(k_+^3 + k_-^3)\sigma_z \tag{3.2}$$

where $k_\pm = k_x \pm ik_y$. This model captures not only the linear dispersion near the Dirac point but also the hexagonal warping effect at higher energies. The characteristic energy and length scale introduced by hexagonal warping are defined as $E^* \equiv v/a$ and $a \equiv \sqrt{\lambda/v}$, respectively. The best fitting parameters we obtained by comparing to ARPES data are: $v = 3.18\ eV\cdot\text{Å}$ and $\lambda = 137\ eV\cdot\text{Å}^3$ [73] which subsequently give the value of E^* to be approximately $450\ meV$.

Referring to the computation on the SS of Bi_2Te_3 [83], the Hamiltonian induced by impurity scattering can be written as

$$H_{imp} = \int d^2k d^2k' V_{\vec{k}-\vec{k}'}\Psi^\dagger(\vec{k}')[\mathbb{I} + ic\vec{k}\times\vec{k}'\cdot\vec{\sigma}]\Psi(\vec{k}) \tag{3.3}$$

The second term corresponds to the spin-orbit scattering with the coefficient *c* describing its relative strength to the potential scattering. The spin-orbit scattering exists in any realistic system and has the tendency to reinforce the quasiparticle scatterings at large momenta. Hence, the effect of this term on the QPI patterns will become more and more obvious as energy increases.

The numerical results was obtained by employing a T-matrix approach and the calculated QPI image for *c*=0.5 with energy $E = 1.5E^*$ shows prominent features which look very similar as in our data at high energies, including the splitting along Γ-M and dot-shaped *q*-vector along Γ-K (figure 3.9). With the appearance of new interferences associated with larger momentum

scatterings brought in by nonzero *c*, our experimental data are in good agreement with the theoretical prediction when spin-orbit scattering is taken into account. Considerable spin-orbit coupling may be naturally created by the Bi anti-site defects in the Te plane for example. In addition, although the signal is relatively weaker, a similar pattern was observed at high energies in pristine Bi_2Te_3 as well, indicating a common impurity such as a Te vacancy or a Bi anti-site defect results in the nontrivial spin-orbit scattering.

3.7 Conclusions

In summary, we have used Fourier-transform STS to investigate the QPI patterns in a three-dimensional TI Bi_2Te_3 over a significantly wider energy range compared to the previous studies. We discover that the linear dispersion along the Γ-M direction persists up to ~700 meV above the Dirac point, demonstrating the robustness of SS against bulk-surface mixing in Bi_2Te_3. At even higher energies, we detect an unusual interference pattern with the appearance of new dispersive QPI modes. We propose a possible explanation for the observation of the two-component QPI peaks along the Γ-M direction, as an additional impurity-induced spin-orbit scattering process, which was theoretically predicted but not experimentally observed so far. Interestingly, we find this unusual pattern is a common feature in samples with Fe dopants which break TRS as well as pristine samples, meaning that such scattering processes are expected in all materials that contain strong spin-orbit coupling impurities. Our experiments undoubtedly reveal the rich physics present in the high-energy electronic structure of three-dimensional TIs, and might serve as a platform for future theoretical models of SS in TIs.

Chapter 4

Visualizing the high-energy band structure in 3D topological insulator Bi_2Te_3

A topological insulator is characterized by an inverted band structure driven by strong spin-orbit coupling. The electronic state transition from topological to non-topological phase is indispensable to understand the unique properties of topological insulators and to realize novel topological phenomena. In this chapter we track the surface states evolution in $(Bi_{1-x}In_x)_2Se_3$ series, with applying Landau quantization approach to extrapolate the band dispersions on the surface for samples with different indium content. We preliminarily suggest that a topological phase transition may occur in this system when x reaches around 5%, based on the experimental signature indicating the transformation of the surface Dirac cone structure at this doping.

4.1 Topological phase transition

As topological insulators are a distinct quantum state of matter which can be viewed as a sea of massless Dirac fermions protected by the TRS, it is of particular interest to study the quantum phase transition (QPT) from the topological to the trivial state. According to theoretical proposals [85][53], a mass acquisition due to the gap opening in the surface states through a QPT process is also essential to realize novel topological phenomena.

Whether a band insulator is topological or not is determined by the nature of their bulk band wavefunctions, which can be described by the Z_2 invariants. A topological insulator is characterized by an inverted band structure driven by strong SOC, and this band inversion mechanism applies to all known TI materials [37][51][86]. However, the successive evolution of the electronic state across the QPT has not yet been well investigated, partially because of the limited suitable materials.

A QPT from a topological insulator to a conventional insulator with a change in topological class can occur only when the bulk band gap closes [87]. Alloying topological insulators with lighter elements is expected to modulate the SOC, and thus lead the bulk band gap to close and invert at a quantum critical point, driving the system going through a topological QPT [30][34]. This has first been realized and observed in the thallium-based ternary chalcogenide alloy $TlBi(S_{1-x}Se_x)_2$ [68][88]. The electronic structure evolution in this system presents a topological QPT at x~0.5, where the bulk gap closes and the band parity is interchanged.

4.2 Quantum phase transition in In-Bi_2Se_3 system

Recently, it was reported that the $(Bi_{1-x}In_x)_2Se_3$ system transforms from a topologically nontrivial state into a trivial state as the indium doping increases and the critical transition point is around x~0.03-0.07 [89][90]. The undoped Bi_2Se_3 (x=0) is a moderately large-gap semiconductor with a rhombohedral crystal structure (space group $D_{3d}^5(R\bar{3}m)$ [91]). The unit cell contains five atoms with quintuple layers ordered in the Se(1)-Bi-Se(2)-Bi-Se(1) sequence, which shares the common crystal structure as in Bi_2Te_3. An intrinsic band gap of approximately 0.3 eV is estimated by

theoretical calculations [92] and is also demonstrated in experiments [93][58]. Bi_2Se_3 possess surface states (SS) that is found to be nearly the idealized single Dirac cone, which makes Bi_2Se_3 a notable 3D TI with the simplest surface spectrum and the largest band gap. As seen from ARPES data in figure 4.1(a), there is a clear V-shaped band pair approach the Fermi level along Γ-K and Γ-M directions on the (111) surface of Bi_2Se_3 [50]. The observed band structure agrees globally with the theoretically calculated spectrum with including the strong SOC, which shows the gapless spin-split SS crossing each other at the Γ point (figure 4.1(b)).

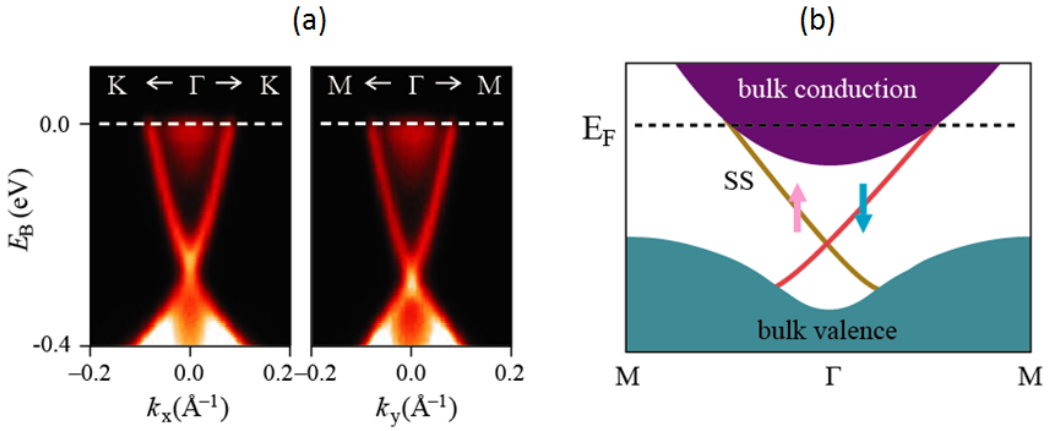

Figure 4.1: Dirac surface states on Bi_2Se_3. (a) ARPES measurements of the surface band dispersion on Bi_2Se_3 (111) along Γ-K and Γ-M directions. A single SS Dirac cone was clearly demonstrated. (b) Schematic presentation of the spin-polarized SS from the corresponding band structure calculations on the surface of Bi_2Se_3 when SOC is included. Adapted from [50].

In_2Se_3, the end member in $(Bi_{1-x}In_x)_2Se_3$ series, is a topologically trivial band insulator with energy gap around 1.3 eV [94]. Still, it maintains the same rhombohedral D_{3d}^5 structure as the topological insulator Bi_2Se_3 [89], which is one of the advantages of $(Bi_{1-x}In_x)_2Se_3$ system for QPT study. The substitution of bismuth (Bi) atoms with lighter indium (In) atoms is supposed to

weaken the SOC strength and contract the lattice constant (4.14 Å for Bi_2Se_3 and 3.95 Å for In_2Se_3), which will consequently induce the emergence of a QPT at some quantum critical point where the bulk bands invert. Moreover, the orbital mixing caused by the changing of bonding orbitals in Bi ($6p^3$) to In ($5s^2 5p^1$) may have an additional effect on the topological transition in this system [95]. In this regard, $(Bi_{1-x}In_x)_2Se_3$ is a unique material which provides a new platform to explore the topological tunability with a structural match to Bi_2Se_3.

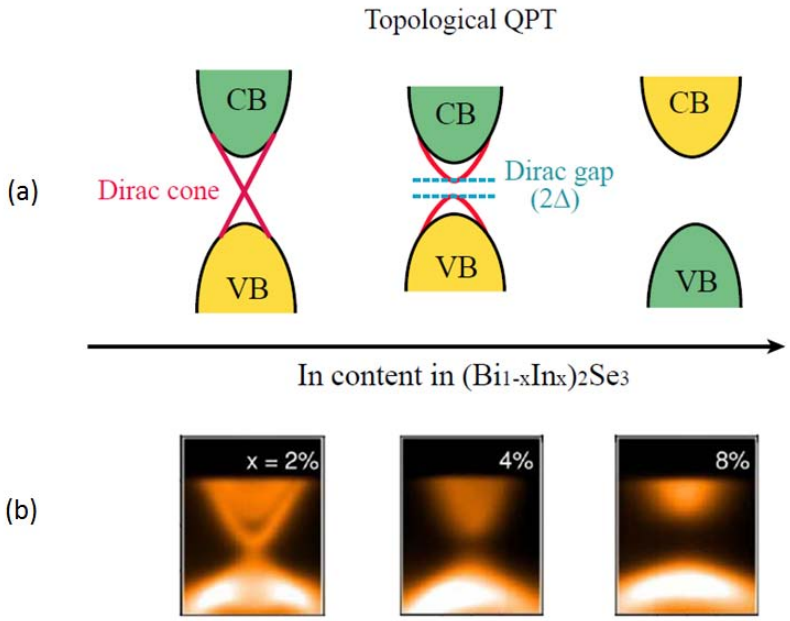

Figure 4.2: Topological quantum phase transition in $(Bi_{1-x}In_x)_2Se_3$. (a) Schematic diagram of the topological phase transition in $(Bi_{1-x}In_x)_2Se_3$. SS (red) gradually disappear from the inverted bulk bands (topological phase) to the non-inverted bulk bands (non-topological phase), accompanied with a small gap opening at the Dirac point on the surface. (b) ARPES data on $(Bi_{1-x}In_x)_2Se_3$ thin films at x=2%, 4% and 8% respectively. The SS evolve from topological phase (x=2%) to non-topological phase (8%). In between a Dirac gap feature was observed. Adapted from [89].

According to the measurements on $(Bi_{1-x}In_x)_2Se_3$ thin films by transport and ARPES [89], as well as by terahertz conductance and optical absorption [90], a signature of topological QPT has been observed at the critical transition point in the range of x≈0.03 to x≈0.07. Demonstrated in the ARPES spectra (figure 4.2(b)), the surface band gradually smears out with increasing x, followed with an inversion of conduction and valance bands, and a Dirac gap on the SS appeared during this transition process.

4.3 Surface states of $(Bi_{1-x}In_x)_2Se_3$ series

Because of the potential applications in fabricating tunable devices, the field of topological phase transition is of great value and has attracted lots of attention in recent years. Practically, the previous experimental studies have shed a light on our STM research work in order to examine more details of the topological QPT procedure in $(Bi_{1-x}In_x)_2Se_3$ series. However, we are more interested in the bulk materials considering their easier preparation and accessibility in real life than thin films. Combined all these factors, we carry out the comprehensive STM and STS investigation on $(Bi_{1-x}In_x)_2Se_3$ with In concentration ranging from x=0 (pristine Bi_2Se_3) up to x=0.05. Our results clearly reveal the nano-scale variation of the surface density of states as x increases, with a qualitative change at x=0.05. By fitting LL spectroscopy data, an evident transformation of the SS band structure at this doping level displayed as well. Our observations are therefore consistent with the trend of topological SS evolution in $(Bi_{1-x}In_x)_2Se_3$ proposed in figure 4.2(a), and we infer that a topological phase transition occurs around x=0.05.

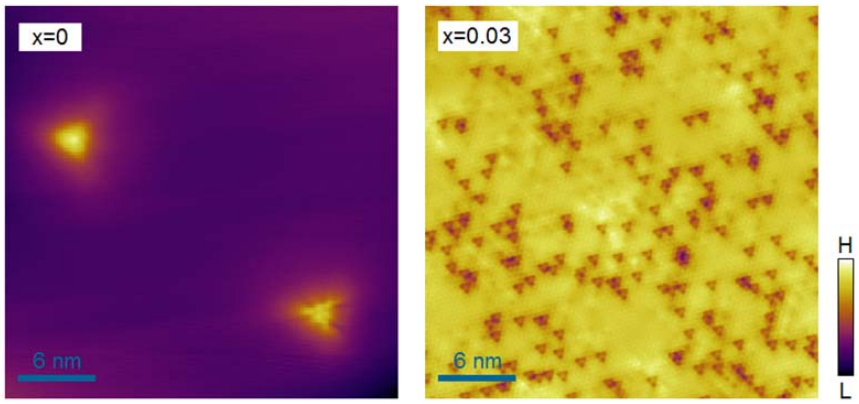

Figure 4.3: Topographs on the surface of undoped Bi_2Se_3 (x=0) and 3%In-doped Bi_2Se_3 (x=0.03). A comparison of two implies the possible signatures of the doped indium atoms which replace the bismuth atoms. We initially attribute the apparent three-dot defects as In-associated.

$(Bi_{1-x}In_x)_2Se_3$ single crystals with various In concentrations were grown by Bridgeman method. All the samples were cleaved in UHV at room temperature. First of all, we show in figure 4.3 the typical STM topographs of pristine Bi_2Se_3 and In-doped Bi_2Se_3 (a sample with relatively lower In doping level is presented here to resolve each impurity more clearly), respectively. The image of undoped Bi_2Se_3 exhibits a small density of defects (approximately one per 15 nm^2) on the surface, which appear as the bright triangular-shaped protrusions [71][57]. These defects may represent Se vacancies and/or Bi defects at the Se sites [96][18]. In In-doped Bi_2Se_3 samples, STM topographs reveal distinct defects that were not observed in native Bi_2Se_3 samples and could be assigned as In-related. The triangle impurities manifesting threefold symmetric feature with three composed dark spots are located on the topmost Se atoms, by carefully examining their atomic positions in the close-up STM images (figure 4.4(a)). Here we emphasize again that the crystal structure of Bi_2Se_3 [51] consists of hexagonal panels of Bi and Se stacked on top of

each other as illustrated in figure 4.4(b). The hexagonal lattice of Se-terminated surface is exposed in STM studies. Thus the defects induced by In substitution are supposed to occupy the subsurface Bi layers, which should be in between the top Se atoms. Therefore, we attribute the observed triangle depressions are substitutional In atoms residing in Bi sites.

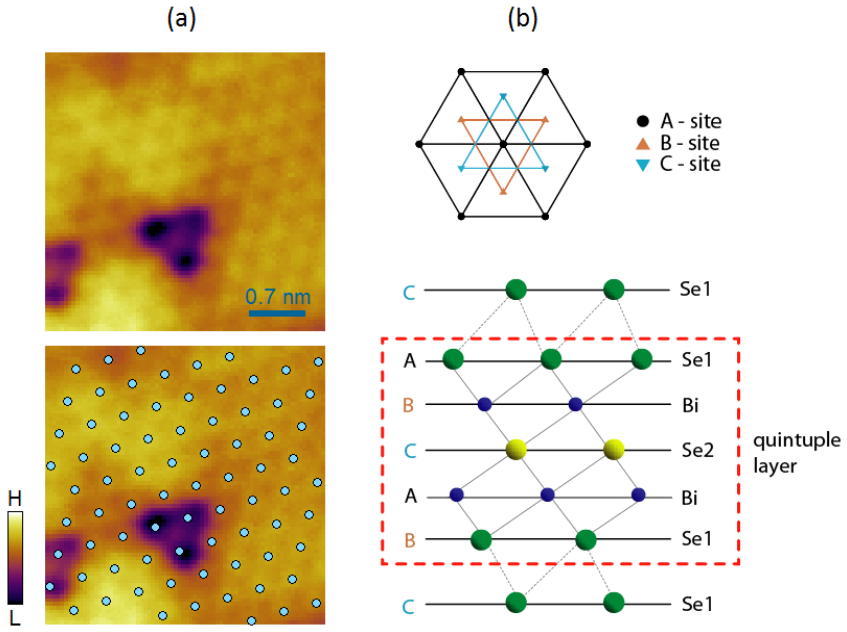

Figure 4.4: Zoomed-in topographs with single atomic defect. (a) High resolution STM images focusing on single defect unambiguously demonstrate its atomic position. Referring to the crystal structure of Bi_2Se_3 [51] illustrated in (b), we further identify the observed impurities as In atoms which are supposed to be located at the subsurface Bi layer.

Now that we are able to identify the In impurities in STM topographs, we can further estimate the real In content. In fact, an accurate knowledge of the actual doping level is crucial for many different experiments and obviously it is especially important for the study of QPT. In specific, we determine the compositions of our $(Bi_{1-x}In_x)_2Se_3$ samples by imaging the distinct In dopants

within large fields of view (50 nm). We actually find that the measured In concentrations are remarkably close to the nominal doping levels for all the samples we have studied.

Next we plot the d*I*/d*V* spectrum at zero magnetic field for each $(Bi_{1-x}In_x)_2Se_3$ sample with different In content x. The direct measurements of the local density of states of a sample surface at various energies will give us important information of the topological surface states. We are most interested in the LDOS near the Dirac point, which can catch the most notable feature of Dirac surface states and thus serve as an essential indication of the critical transformation from nontrivial to trivial states. The typical d*I*/d*V* spectra on lower doped samples (x=0.01 and x=0.03) look very similar to that of pristine Bi_2Se_3 [71][57], as shown in figure 4.5. Each spectrum exhibits a V shape with a minimum at about 300 mV below the Fermi level, which corresponds to the Dirac point of the topological states. The LDOS increases rapidly below about 500 mV and above Fermi level, possibly associated with the contributions from the bulk bands. Given that the V-shape LDOS spectra including the visible reflection of Dirac point agrees well with the Dirac cone structure of the SS, we speculate that these samples with low In concentrations ($x<0.03$) feature nontrivial topological states. On the other hand, in the sample with higher In concentration (x=0.05), the V-shape of the spectrum near the Dirac point disappears where the DOS are largely suppressed and are quite flat. Since the V-shape reflects the topological nontrivial surface states within the bulk band gap, its absence suggests that the Dirac surface sates are not well defined any longer at this concentration. Thus, we initially conclude that the system might transform to the non-topological phase at some critical point around x=0.05, with the occurrence of bulk bands inversion.

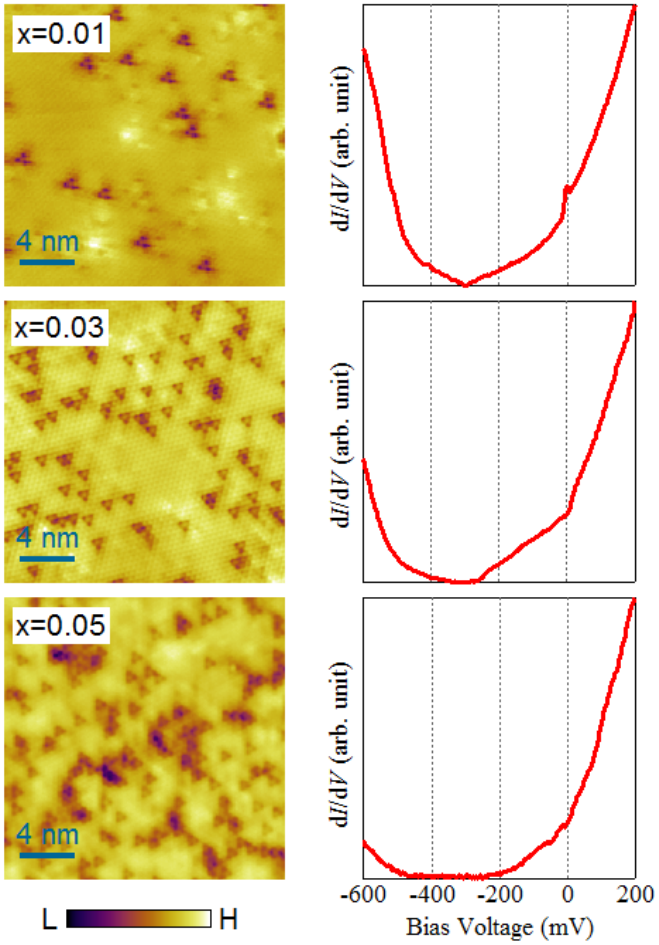

Figure 4.5: Surface states evolution in $(Bi_{1-x}In_x)_2Se_3$. Topographs of different samples at x=0.01, 0.03 and 0.05 (left panel) display an increasing density of impurities. The corresponding d*I*/d*V* spectra (right panel) show a general trend of the DOS evolution as x increases, particularly around the Dirac point (spectrum minimum). At x=0.05, the spectrum exhibits largely suppressed surface DOS indicative of the disappearance of Dirac node, which implies the occurrence of topological phase transition near this doping level.

To confirm this scenario and further investigate the impact of In doping on the topological surface states, Landau level (LL) measurements are performed. Generally, in a magnetic field,

LLs will appear in d*I*/d*V* spectra as field-induced peaks on top of the V-shaped background, and can provide direct access to the SS band structure in *k*-space.

4.4 Landau quantization approach on topological insulator

When magnetic field is applied to a two-dimensional electron system (2DES), the energy spectrum is quantized into discrete LLs as shown in previous experiments on various 2DES [97][16][98]. For topological insulators, the LL spectroscopy is especially important because of the anomalous quantum nature of the massless Dirac fermions [99][100]. In the presence of a perpendicular magnetic field, the Landau orbits of SS electrons are quantized in *k*-space with discrete values of momentum and energy, k_n and E_n ($n = 0, \pm1, \pm2, \ldots$). According to the Bohr-Sommerfeld quantization condition, the area of the nth Landau orbit in *k*-space is given by $S_n = (n + \gamma)2\pi eB/\hbar$ (equation 1.8), where n is the LL index and γ is the phase factor. For an isotropic Dirac cone, the Berry-phase effect eliminates γ and $S_n = \pi k_n^2$. So the momentum can be simply expressed as $k_n = \sqrt{2e|n|B/\hbar}$.

On the other hand, the energy of the nth LL spectrum of the massless Dirac fermions follows the unique square-root dependent sequence on magnetic field and is expressed as

$$E_n = E_{DP} + \mathrm{sgn}(n)v\sqrt{2e\hbar|n|B} \tag{4.1}$$

where E_{DP} is the energy of Dirac point and v is the velocity of electron. Unlike the LLs in a massive 2DES with parabolic dispersion, E_n in a topological insulator is proportional to $\sqrt{|n|B}$ instead of being linear in nB. Since $\sqrt{|n|B}$ represents the momentum k_n, a set of E_n and k_n

with specific n and B from the LL spectroscopy can be obtained, and consequently the *E-k* dispersion can be derived by plotting E_n against $\sqrt{|n|B}$. In addition, different from the conventional electron systems, the 0th LL at E_{DP} is independent of the magnetic field for TIs. These features have been reported earlier on graphene by STS experiments [16][99]. Previous LL measurements on Bi_2Se_3 surface [96][18] have also demonstrated the unique Landau quantization with linear *E-k* dispersion indicating the properties of massless Dirac fermions as in graphene.

For the gapped topological SS with a mass acquisition, the LL energies are then given by

$$E_n = E_{DP} + \mathrm{sgn}(n)\sqrt{2e\hbar v^2|n|B + \Delta^2} \tag{4.2}$$

where $\Delta = JM_z/2\mu_B + \frac{1}{2}g_s\mu_B B$ is the mass term [101]. The first part comes from the magnetic ordering and the second part is the Zeeman term. For $n = 0$, the corresponding LL peak is supposed to deviate from the Dirac point energy by a magnitude of Δ which is field dependent in this case.

4.5 Landau spectroscopy probed by STS

We successfully observed LLs on samples at x=0.01, x=0.03 and x=0.05 by applying magnetic field to 7.5T (figure 4.6). Furthermore, the magnetic field dependence of the tunneling conductance clearly reveals the development of LLs corresponding to the series of peaks (figure 4.7). The absence of LLs below the Dirac point are likely due to the overlapping of the SS with the bulk valance band [50]. Under strong magnetic field (5T and above), unequally spaced LLs

are explicitly resolved. For x=0.01 and x=0.03, there is always one peak residing at the Dirac point position in each LL sequence and the energy of this LL is independent of the magnetic field, consistent with the Dirac fermion model and thus identified as 0th LL. Indeed, the Dirac point signifies the unique nature of the topological SS bands, which continuously span the bulk band gap between the conduction and valence bands. The presence of this topologically protected point is manifested as a non-dispersive peak in d*I*/d*V* spectra located at the DOS minimum, which are not supposed to be observed in trivial regime. Based on this fact, we examine the LL spectra at different In concentrations, and find that the samples with x=0.01 and x=0.03 should be in the topological regime with the existence of such field-independent peak. However, it is missing for x=0.05, which implies the discontinuity of the SS bands in this sample with the possible formation of a gapped Dirac cone.

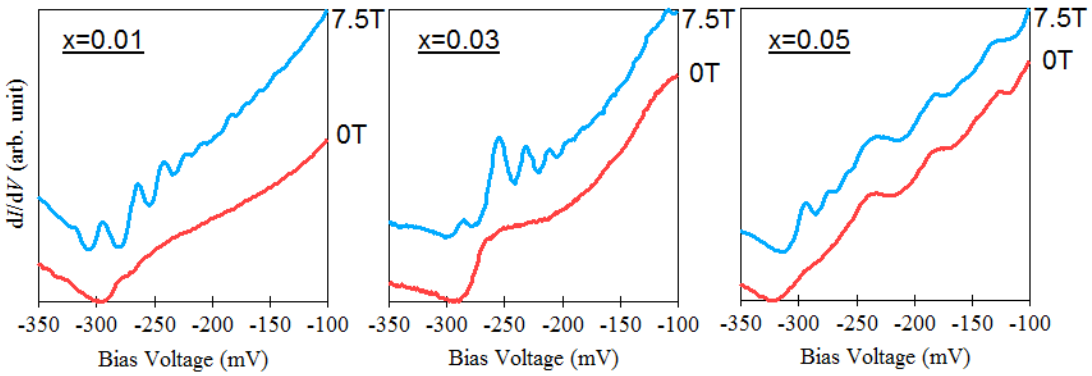

Figure 4.6: Landau level spectroscopy acquired at 0T (red) and 7.5T (blue) over the same area of the sample surface for x=0.01, 0.03 and 0.05, respectively. Extra peaks appear on the d*I*/d*V* curves at 7.5T, observed as Landau quantization induced by the presence of magnetic field.

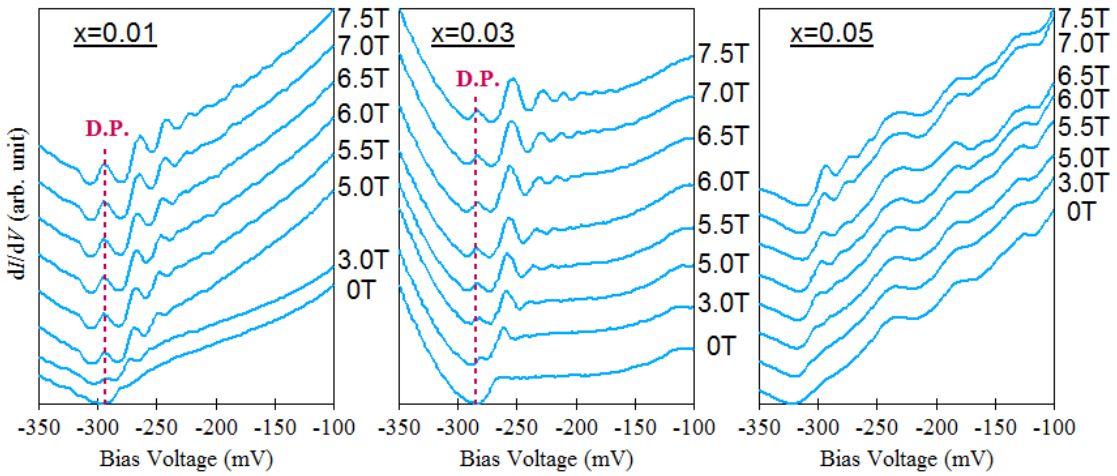

Figure 4.7: Landau level spectroscopy acquired at various magnetic fields from 0T to 7.5T over the same area of the sample surface for x=0.01, 0.03 and 0.05, respectively. For x=0.01 and x=0.03, there is a non-dispersive peak at non-zero fields which is located precisely at the DOS minimum at zero field. Since it does not change with field, it is identified as the 0th LL at Dirac point (D.P.). The higher orders of LLs are found to be dispersing. The non-dispersive peak is absent in sample at x=0.05, indicating the lack of Dirac point and the transformation of Dirac cone structure.

To further access to the SS band dispersion of each sample, we index the observed LLs and then plot the peak energy E_n as a function of $\sqrt{nB}$ related to the momentum. LL indexing is determined by the scaling constraint in order to collapse the dispersion onto a continuous line. The subsequent fitting for the sample at x=0.01 is shown in figure 4.8. Here the LL spectrum is normalized with polynomial background subtraction to get rid of the background density of states. As expected for the dispersion of a topological insulator, the plot of E_n against $\sqrt{nB}$ reveals a nearly linear fit. Interestingly, there is an additional peak (n') appearing between the

$n = 0$ and $n = 1$ LLs. This was also observed before in Bi_2Te_3 [102] and the origin of this peak is still unclear. Next we index the LL peaks on x=0.03 sample with the same assignment and then plot the energy versus $\sqrt{nB}$. A very similar dispersion behavior as in sample at x=0.01 displaying linear feature is obtained (figure 4.9), which is indicative of the topological properties with this doping level.

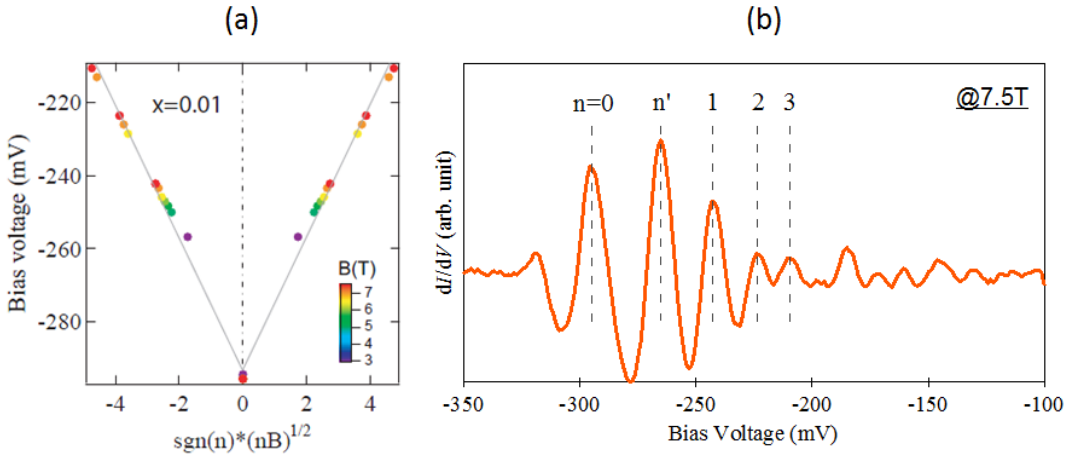

Figure 4.8: Landau level fitting for sample at x=0.01. (a) The gray line schematically depicts the nearly linear SS dispersion which suggests the topological nature of this sample. (b) Normalized d*I*/d*V* spectrum at 7.5T with 20th polynomial background subtraction. LL indices are denoted to plot the dispersion in (a).

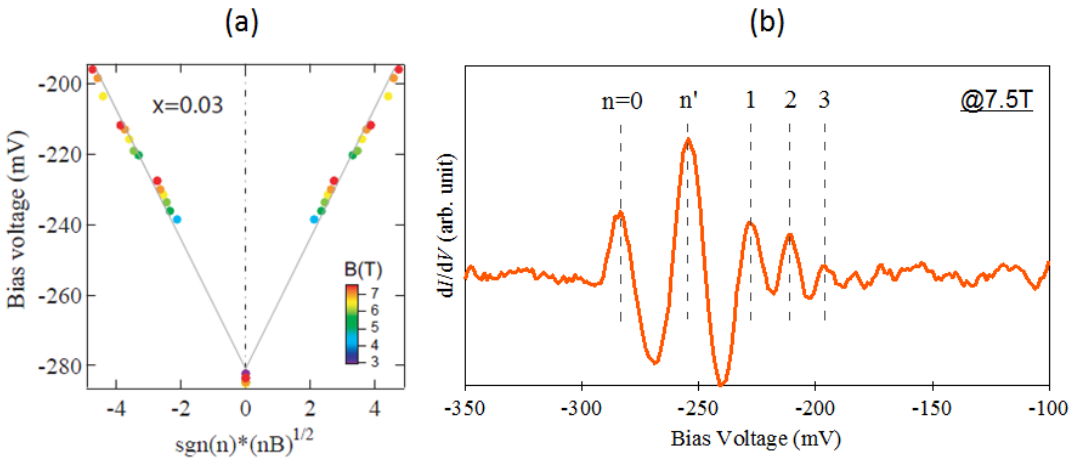

Figure 4.9: Landau level fitting for sample at x=0.03. (a) The gray line schematically depicts the nearly linear SS dispersion which suggests the topological nature of this sample. (b) Normalized d*I*/d*V* spectrum at 7.5T with 20th polynomial background subtraction. LL indices are denoted to plot the dispersion in (a).

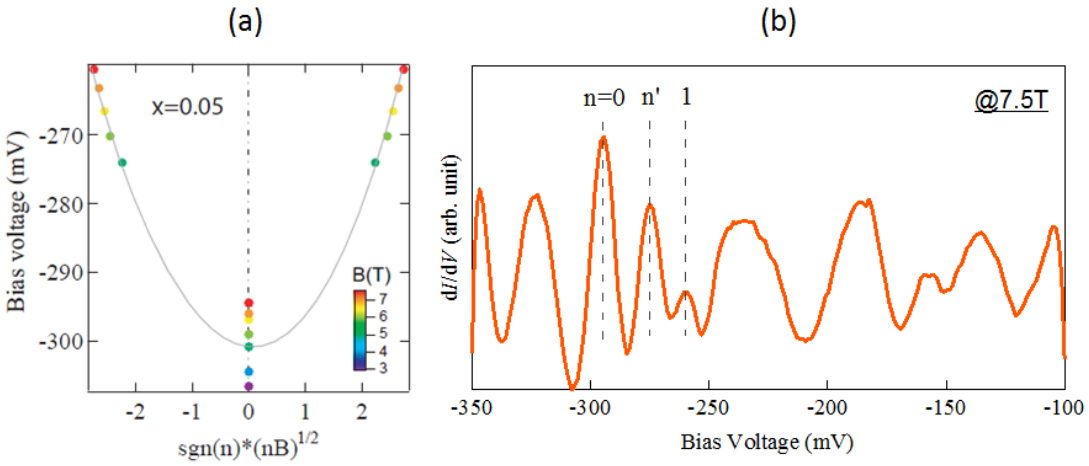

Figure 4.10: Landau level fitting for sample at x=0.05. (a) The gray line schematically depicts the parabolic behavior of the SS dispersion, indicative of the Dirac gap opening and the subsequent transition to non-topological phase around x=0.05. (b) Normalized d*I*/d*V* spectrum at 7.5T with 20th polynomial background subtraction. LL indices are denoted to plot the dispersion in (a).

As for the x=0.05 sample, however, the dispersion behaviors qualitatively different from the other two samples. We follow the same indexing way on the LL spectroscopy of this sample, and assign the first peak apparent in the fields as the 0th LL (figure 4.10). Considering that we did not see many LLs on this sample which may be due to the high density of impurities that would induce considerable scattering events, we are only able to plot the *E-k* relation based on the limited number of dispersive peaks of the d*I*/d*V* spectra. Nevertheless, we still get a reasonably

parabolic-like curve by fitting the LLs with the same scaling method, which to some extent reflect the non-topological SS where a Dirac gap is probably opening.

4.6 Conclusions

By systematically tracking the extracted SS band dispersions from LL fitting, combined with the zero-field spectra for all the samples, we can find an evolution of the surface Dirac cone in terms of the density of states in $(Bi_{1-x}In_x)_2Se_3$ series. At x=0.01 and x=0.03, the SS exhibit well-defined Dirac cone nature with the characteristic band structure of massless Dirac fermions. At x=0.05, however, the non-dispersive LL peaks in magnetic fields corresponding to the topologically protected Dirac point are missing. At zero field a largely suppressed DOS around this point is observed as well. More importantly, we acquire a qualitatively different *E-k* dispersion showing quadratic feature at this doping, compared with the mostly linear dispersive behavior at lower dopings. We therefore propose that the QPT in $(Bi_{1-x}In_x)_2Se_3$ system from topological to non-topological phase occurs around x=0.05, where the surface Dirac cone seems to be gapped out as previously demonstrated by ARPES in the thin films (figure 4.2).

Chapter 5

Spin-orbit coupled Mott insulators: strontium iridates

In the physical picture based on conventional band theory, electrons are described as independent particles and the system can be accordingly classified into insulators with fully-filled energy bands and metals with partially-filled bands. However, in strongly correlated materials, which are generally associated with open *d* or *f*-shells such as transition metal oxides (TMO) and rare-earth compounds, the single-particle framework is not suitable any more since the repulsive Coulomb interaction between electrons plays an overwhelming role. The electronic correlation could be strong enough to prevent the motion of electrons and induce an insulating phase even though the energy bands of the system are not fully filled. Such a material is categorized as "Mott insulator" [103][104].

Recently a new class of 5*d* Mott insulators was discovered in iridates, such as Sr_2IrO_4 [105][106][107] and Na_2IrO_3 [108][109]. Whereas 5*d*-TMO are usually considered as weakly correlated, these materials exhibit insulating states. It was recognized now that the strong spin-orbit interaction plays a crucial role in generating and stabilizing the novel narrow-gap state, and a model of "spin-orbit driven Mott insulator" was thereby suggested. According to this proposal, the cooperative interaction between the electronic correlations and the strong SOC explains the new exotic ground states in 5*d* iridate materials.

5.1 Transition metal oxides and Mott physics

The extraordinary properties of transition metal oxides (TMO) make them worthy of special attention for decades [110]. As a matter of fact, there are a variety of electronic states in TMO ranging from insulating to metallic and even superconducting. The unique nature of the outer *d*-electrons in TMO is the core of realizing numerous oxidation states in these compounds. In addition, the direct overlap between *d*-orbitals is typically very small which leads to the formation of quite narrow electronic bands in the oxides. The electron correlation can then play a significant role in such narrow bands case, which distinguishes TMO from other compounds. More importantly, the physical properties of many TMO can traverse with tuning temperature, magnetic field, pressure, or chemical composition, which generates very rich phase diagrams. The quantum phases exhibited in TMO, such as the high-temperature superconductivity in cuprates [111], colossal magnetoresistance in manganites [112], unconventional superconductivity in ruthenates [113], and the unusual magnetic ordering in iridates [105], have unveiled lots of novel physics in this fascinating class of materials.

Mott physics based on Hubbard Hamiltonian, which explains the insulating nature in materials induced by electron correlation, has been studied for several decades from both theoretical and experimental points of view [114]. It serves as an essential foundation for understanding the emergent properties of strongly correlated TMO systems. According to Hubbard model, the system can be characterized by the ratio U/W, where U is the intra-atomic Coulomb repulsion energy ("Hubbard U") and W is the bandwidth. When $U/W \gg 1$, the system is in an insulating state, the so-called Mott insulator. When $U/W \approx 1$, which is near the border line of the Mott

criteria, the system becomes metallic. Great success has been achieved in 3*d* TMO to support this model, in which the localized 3*d* states yield strongly correlated narrow bands with a large U and a small W. As predicted, most stoichiometric 3*d* TMO are found to be anti-ferromagnetic Mott insulators.

5.2 Mott insulating states in 5*d*-iridates

3*d* and 4*d* TMO have attracted lots of attention in the past years [115][116][117]. With strongly correlated electrons, these compounds can be modified in crystalline structure with changing external temperature, pressure or with suitable doping, resulting in a variety of states associated with novel phenomena. On the other hand, the electronic orbits of 5*d* TMO are spatially more extended with broader bandwidth than in their 3*d* and 4*d* counterparts. Moreover, the on-site Coulomb repulsion is reduced to a mere 1-3 eV comparing to 2-10 eV for 3*d* electrons, so the electron interactions should play a much smaller role. For these reasons, the 5*d* TMO are commonly expected to be more metallic than their 3*d* and 4*d* counterparts, considering a favorable metallic state in these conditions [118]. In fact, many of the 5*d* TMO have metallic ground states that can be described by the band theory [119][120], such as the correlated metal $SrIrO_3$ [121].

However, on the contrary, some 5*d* TMO such as Ba_2NaOsO_6 [122] and many of the other iridates Na_2IrO_3, Sr_2IrO_4, and $Sr_3Ir_2O_7$ [109][123][124] were found to have insulating ground states. Considering the delocalized electrons with weakly-correlated wide band in 5*d* states, the anomalous insulating behaviors in these 5*d* TMO are unexpected and have consequently

prompted the extensive studies. Now it has been realized that to solve this problem the SOC should be taken into account.

In 3*d* TMO, the SOC is substantially small compared with the electronic correlations, and hence it is usually treated as a perturbation. Whereas in 5*d* TMO with heavier atoms, the strength of the SOC is much larger and it needs to be treated equally as the correlation effect. With the spatially more extended orbitals in 5*d* oxides, the comparable energy scales of SOC and the on-site Coulomb repulsion can create the unconventional spin-orbit states. Indeed, the competition of this additional interaction with other energy scales such as the crystal field is capable of modifying the electronic structure of materials [125], resulting in a localized state which is significantly different from those in conventional insulators.

In 2008 Kim et al. [105] proposed a new scenario to understand the insulating behaviors in strontium iridate Sr_2IrO_4 by emphasizing the role of SOC, more specifically, the cooperative interaction between the SOC and the electronic correlations. In this theoretical model, a large spin-orbit interaction splits the 5*d*-band into a fully filled band and a half-filled band, with the Fermi level residing in the latter. The bandwidth of the half-filled band is so narrow that even the greatly reduced Coulomb interaction U is sufficient to open a gap and reach the Mott insulating state. This leads to a novel spin-orbit induced Mott state, and defines a completely new class of materials.

Owing to the octahedral crystal field environment, the outer 5*d* electrons of Ir^{4+} are split into the lower-lying t_{2g} levels and the higher-lying e_g levels, as illustrated in figure 5.1. Given that the

spin-orbit interaction in iridates (λ~0.4 eV) [120] is much larger than that in 3*d* systems (λ~20 meV) [126], it can further split the t_{2g} manifold into the effective total angular momentum J_{eff}=3/2 quadruplet and the effective total angular momentum J_{eff}=1/2 doublet. Moreover, the t_{2g} bands are occupied by five electrons [127], and J_{eff}=3/2 bands are completely filled with four electrons while only one electron remains in the narrow J_{eff}=1/2 bands. As a result, the SOC splits the t_{2g}^5 states of the 5*d*-shell into a half-filled J_{eff}=1/2 and fully-occupied J_{eff}=3/2 states, and the half-filled J_{eff}=1/2 band with narrow bandwidth tends to undergo Mott transition even at a relatively weak Coulomb interaction U.

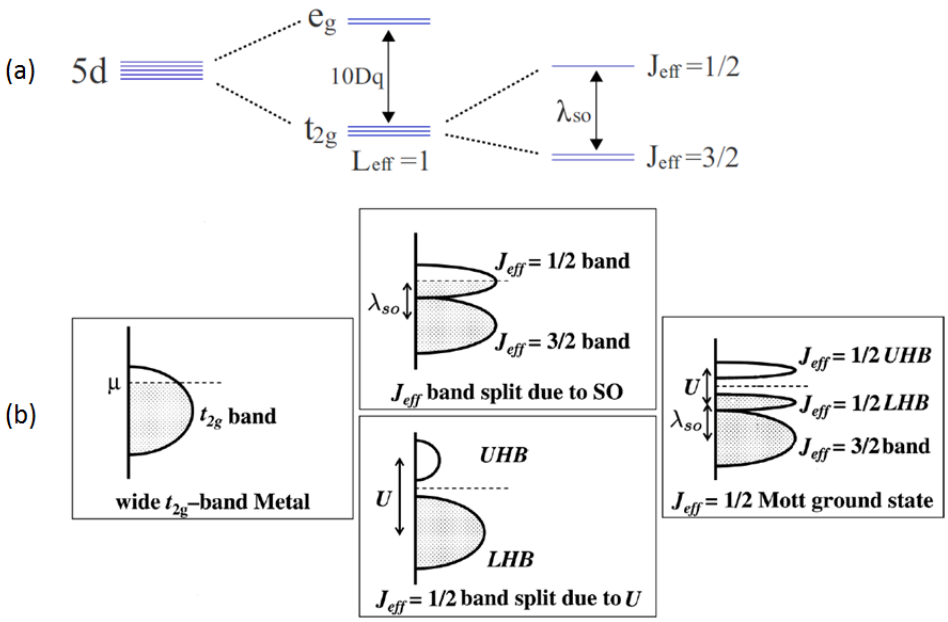

Figure 5.1: Energy diagram and band splitting of 5*d* orbital. (a) Energy splitting of the 5*d*-level due to crystal field and SOC. (b) Schematic diagram for the t_{2g}^5 configuration showing the removal of orbital degeneracy as well as the band splitting process, by SOC λ_{so} or/and Coulomb repulsion U. Adapted from [105].

This picture, called “spin-orbit driven Mott insulator”, was quickly validated by resonant X-ray scattering [106] and has also given a framework to understand the canted-antiferromagnetic phase of Sr_2IrO_4 [128]. By probing the relative phases of the electronic state in experiments, it was reported that the corresponding ground state in Sr_2IrO_4 is actually very close to the J_{eff}=1/2 limit.

When it was shown that the Sr_2IrO_4 compound displayed novel J_{eff}=1/2 Mott phase with weak ferromagnetism ordering, intensive studies on the analogous materials were subsequently carried out. As suggested, the cooperative interaction between electron correlation and the SOC explains the magnetic insulating state of Sr_2IrO_4. Following by this, the electronic structures of some other compounds in 5*d* Ruddlesden-Popper series $Sr_{n+1}Ir_nO_{3n+1}$ can be understood as well.

5.3 Ruddlesden-Popper series of strontium iridates

TMO that are characterized with the perovskite-type crystal structure, such as cuprates, manganites, nickelates, ruthenates, titanates and iridates, are of the most interest to people and have been studied a lot. First described for $Sr_{n+1}Ti_nO_{3n+1}$ by Ruddlesden and Popper [129], a series of structural phases was derived from the perovskite structure which is well known as layered structure. This series can be described by a general formula $A_{n+1}B_nO_{3n+1}$, where A and B are cations, O is the oxygen anion, and n represents the number of octahedral layers that are immediately adjacent in the perovskite stack [130]. The Ruddlesden-Popper (R-P) series of strontium iridates $Sr_{n+1}Ir_nO_{3n+1}$ is depicted in figure 5.2 for n=1, n=2 and n=∞ respectively. The lattice structure consists of n IrO_2 layers with double layers of SrO in between, where the Ir

atoms are hidden inside the oxygen octahedra.

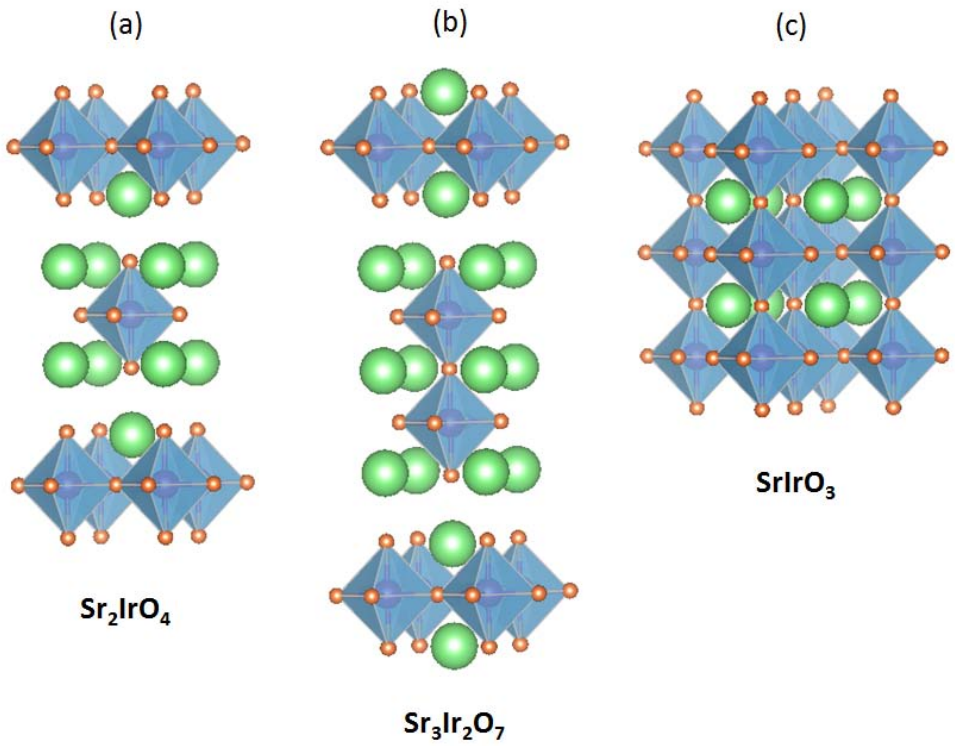

Figure 5.2: Crystal structures of $Sr_{n+1}Ir_nO_{3n+1}$ for (a) n=1, single layer compound Sr_2IrO_4, (b) n=2, bilayer compound $Sr_3Ir_2O_7$ and (c) n=∞, 3D compound $SrIrO_3$ made of IrO_6 octahedra. The green spheres represent for strontium (Sr) and the golden ones represent for oxygen (O), whereas the iridium (Ir) ions are at the center of the octahedra in blue. Models produced using VESTA software.

A progression of n from 1 to ∞ in R-P series corresponds to the change of dimensionality of the compounds. As initially observed in 3*d* TMO such as $(La,Sr)_{n+1}Mn_nO_{3n+1}$ [131] and then 4*d* TMO such as Ca and Sr ruthenates [132], the ground states of R-P series are critically linked to the number of perovskite layers. Similarly, the 5*d* iridates of R-P series $Sr_{n+1}Ir_nO_{3n+1}$ also exhibit a

systematic evolution of electronic properties as a function of the number of IrO_2 layers n. First of all, the single layer compound Sr_2IrO_4 (n=1) is a Mott insulator showing weak ferromagnetism [123], which was understood to stem from a canted antiferromagnetic pattern in the J_{eff}=1/2 states [105]. On the other hand, the charge gap in Sr_2IrO_4 is found to be reasonably large [133]. Next, the bilayer compound $Sr_3Ir_2O_7$ (n=2) remains a Mott insulator but with much smaller insulating gap [107][124] and displays a collinear antiferromagnetic state [134][135]. Finally, the end member of this family with n=∞ is $SrIrO_3$ which is purely three dimensional, and in contrast to the quasi-2D systems, this 3D material is not insulating or magnetic. Indeed, a correlated metallic ground state with non-Fermi-liquid behavior has been found in $SrIrO_3$ [121]. Therefore one can see that the 5*d* systems tentatively follow the general trend of R-P series and become less localized as n increases. In fact, optical spectroscopy and the first principle calculations with SOC included have demonstrated this dimensionality-related insulator-to-metal transition in the R-P series of strontium iridates [107].

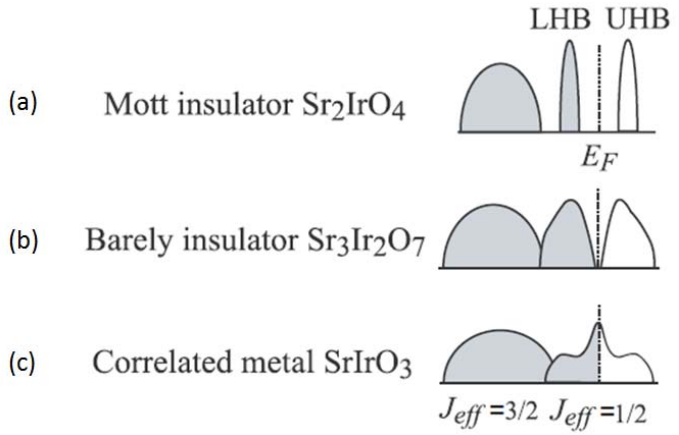

Figure 5.3: Schematic band diagrams of $Sr_{n+1}Ir_nO_{3n+1}$ for (a) n=1, Mott insulator Sr_2IrO_4, (b) n=2, barely insulator $Sr_3Ir_2O_7$ and (c) n=∞, correlated metal $SrIrO_3$. Adapted from [107].

As seen in figure 5.3, the electronic structure of the strontium iridates progresses from highly insulating ground state in Sr_2IrO_4 toward metallic ground state, evidenced by the reducing of the charge gap in $Sr_3Ir_2O_7$ and the metallic state in $SrIrO_3$. Amongst them the intermediate material $Sr_3Ir_2O_7$, displaying barely Mott insulating with a relatively small gap, occupies a unique place which is in close proximity to the Mott transition point. As a result, the bilayer compound $Sr_3Ir_2O_7$ is able to provide a good platform to explore the mechanism of the novel Mott states near the MIT boundary where the competitive interplay between SOC and Coulomb interactions can produce unusual effects. One important approach for this investigation is through appropriate chemical doping, which can generate interesting phenomena and emergent response in physical properties in a lot of materials [136][137][138][139].

5.4 Chemical doping in TMO

In layered compounds of R-P series $A_{n+1}B_nO_{3n+1}$, the nature and size of the cation on either A or B site have significant but distinguished influence on the structure and properties of the material. In general, A-site ion affects the c-axis parameters and the overall structure of the compounds. So the ionic substitution at A site usually leads to drastic change in physical properties associated with the inter-layer coupling. On the other hand, B-site ion is expected to affect the a-axis parameters within the B-O plane. Because of the high susceptibility with introducing of doping elements to replace either A-site or B-site ions, R-P series has offered a fertile ground for studying new physics. In case of materials with novel electronic states such like Sr_2IrO_4 and $Sr_3Ir_2O_7$ displaying Mott insulating behaviors, disturbing the ground states with proper chemical doping that can tune the SOC allows us to test its robustness and infer the possible mechanisms

responsible for these anomalous states as well.

Actually, partial chemical doing in lots of TMO on either A or B site can create some emergent phenomena with interesting physics. For instance, introducing disorders at the Sr site in 3*d* cuprates $Bi_2Sr_2CuO_{6+\delta}$ and $Bi_2Sr_2CaCu_2O_{8+\delta}$ would strongly alter the superconducting transition temperature in these materials [137]. Also, a dilute replacement of Ru by Mn in 4*d* ruthenate Sr_2RuO_4 results in the metal-insulator transition at a critical temperature [138]. All these discoveries have drawn much attention in recent years and promote people to investigate more fully doped TMO, especially for the sequent 5*d* compounds, in the hope of finding new phases and phenomena.

Chapter 6

Electronic phase transition in doped Mott insulator $Sr_3Ir_2O_7$

The bilayer strontium iridate $Sr_3Ir_2O_7$ is in close proximity to the Mott transition point with a low-temperature charge gap, and therefore offers a good platform to examine the carrier-induced electronic structure variation as the system is driven from insulating to metallic phase. In this chapter we investigate the metal-insulator transition (MIT) in $Sr_3Ir_2O_7$ by introducing chemical dopings Ru and La, representing in-plane and out-of-plane dopants, respectively, to determine how defects at particular lattice sites locally affect the Mott ground state. The data demonstrate a drastic difference of the MIT behavior responding to defects at different sites, which reflects the distinct role and influence of these dopants in Mott insulators. Our study can further serve as important indication for the realization of emergent phases at the boundary of a spin-orbit induced correlated oxide.

6.1 Carrier dopings in bilayer iridate $Sr_3Ir_2O_7$

Many experiments have been done on the SOC-assisted Mott insulator $Sr_3Ir_2O_7$ (Ir327), including transport, diffraction, and optical spectroscopy [107][124][135] which demonstrated a variety of correlated order parameters and phase transitions. To data however, the role of Coulomb interactions remains contentious, which in large extent arises from the inherent complexities that Ir327 possess. This bilayer iridate occupies special place in close approximation to a Mott

transition point and thus has the tendency of electronic inhomogeneity often seen in such systems [140][141]. This has created challenges in exploring the actual gap size, the role of correlations, as well as the influence of dopants in Ir327 compounds. Our previous STM/STS studies on parent Ir327 [20] has provided important information for these puzzles by identifying a hard gap of ~130 meV, which comes from a combination of rotated oxygen octahedra, enhanced SOC and Coulomb interactions. In the meantime, this low-temperature charge gap offers a fortuitous opportunity to probe the carrier-induced electronic phase behavior in Ir327 as the system is driven from insulating to metallic, and further determine how defects at particular lattice sites locally affect the J_{eff}=1/2 Mott phase. More practically, prior work has shown that Ir327 single crystals cleave well, making them ideal samples for nanoscale investigations of the doping evolution in a correlated insulator.

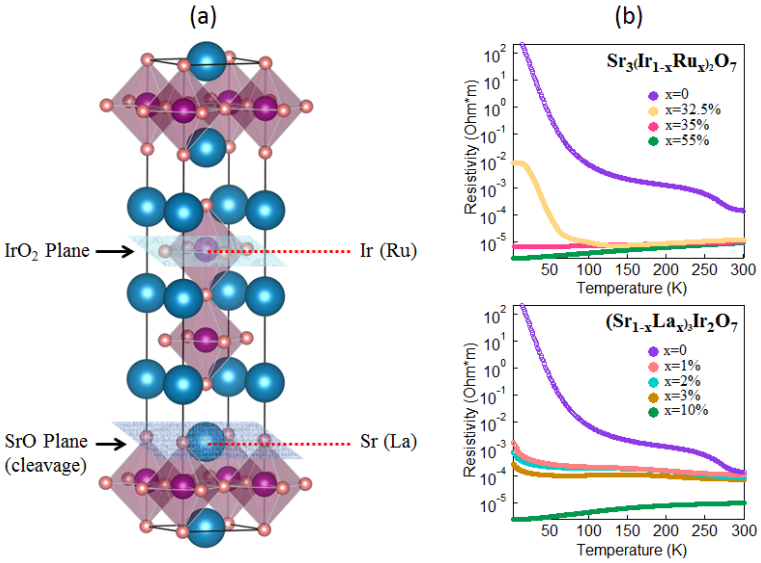

Figure 6.1: Crystal structure and transport data of doped $Sr_3Ir_2O_7$. (a) The crystal cleaves between the two SrO layers. Ru dopants substitute for Ir in IrO_2 plane and La dopants substitute for Sr in SrO plane. (b) Transport results of $Sr_3(Ir_{1-x}Ru_x)_2O_7$ and $(Sr_{1-x}La_x)_3Ir_2O_7$, respectively,

showing significantly different MIT behaviors.

In fact, doping Mott insulators is known to result in a rich phase diagram with exotic charge and spin-ordered phases, especially in layered oxides which offer a variety of sites for doping. The impact of a particular dopant on the electronic properties of the material, however, can vary vastly depending on the doping site. For example, the transition temperature of high temperature superconductors like the cuprates depends sensitively on the position of the dopants with respect to the copper oxide plane [137][136]. Also, doping introduces carriers, strain and disorder all of which play different roles. Here we study the carrier response of the doped strontium iridates $Sr_3(Ir_{1-x}Ru_x)_2O_7$ (Ru-doped Ir327) and $(Sr_{1-x}La_x)_3Ir_2O_7$ (La-doped Ir327), respectively, by probing their electronic properties via STM/STS. $Sr_3Ir_2O_7$ consists of iridium oxide (IrO_2) planes separated by SrO planes providing the possibility of doping in-plane (within the IrO_2 plane) or out-of-plane (within the SrO plane). In our case, Ru is in-plane (B-site) dopant known to substitute for Ir, while La is out-of-plane (A-site) dopant known to substitute for Sr (figure 6.1(a)). Transport measurements indicate that the insulator-to-metal transition takes place in Ru-doped Ir327 at a significant Ru fraction of x=35%, whereas La-doped Ir327 becomes metallic with a substantially smaller La concentration of approximately x=3% (figure 6.1(b)). Motivated by this result, we carried out LDOS measurements in order to understand this drastic difference between the in-plane and out-of-plane dopings in a microscopic scale, which can lead to deeper insights into the role and effects of the dopants in correlated oxides.

Single crystals of $Sr_3(Ir_{1-x}Ru_x)_2O_7$ and $(Sr_{1-x}La_x)_3Ir_2O_7$ were grown using flux techniques similar to earlier reports [139]. All the samples were cleaved in ultrahigh vacuum at about 80 K. From our

previous experiments, cryogenic cleaving is crucial for obtaining high quality surfaces on Ir327 compounds. The natural cleavage occurs between the adjacent SrO planes in perovskite bilayer structure and exposes the (001) surface. Figure 6.2 shows the topographic images of 50%Ru-doped sample and 4%La-doped sample (both in metallic regime) on 50 nm field-of-view. The underlying square atomic lattices are clearly observed, and the lattice spacing is estimated to be 3.9 Å, in good agreement with the in-plane lattice constant of the tetragonal unit cell. Thus we are preferentially imaging either strontium or apical oxygen atoms, and we can unambiguously identify them as Sr atoms based on the prior report [20]. In addition to the primary 1x1 patterns (marked with red circles) reflecting the surface structure, Fourier transforms (FT) of the topographs also show peaks at the $\sqrt{2} \times \sqrt{2}$ positions (marked with green circles) implying the enlarged unit cell. Such $\sqrt{2} \times \sqrt{2}$ structures have also been observed on other TMO surfaces such as $Sr_3Ru_2O_7$ [142][143] and Sr_2IrO_4 [144] which are probably due to the rotations of the RuO_6/IrO_6 octahedra.

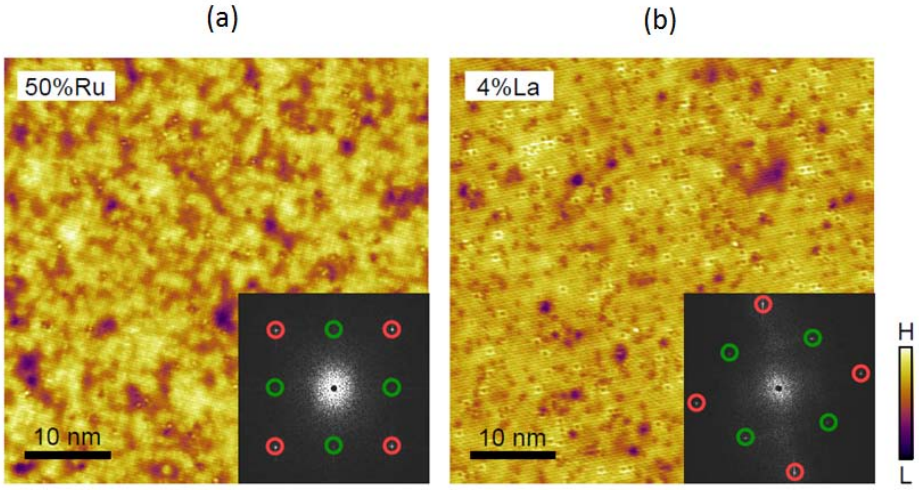

Figure 6.2: Topographs on the surface of 50%Ru-doped $Sr_3Ir_2O_7$ and 4%La-doped $Sr_3Ir_2O_7$. Topographic images are acquired within large field-of-views for (a) 50%Ru-doped Ir327 and (b)

4%La-doped Ir327. La-related defects which manifest as squares centered at Sr atoms are clearly resolved. The insets show the FTs of the corresponding topographs, with bragg peaks denoted by red open circles and root 2 peaks denoted by green open circles.

The topograph on the surface of La-doped sample reveals a small percentage of defects with square-shaped patterns (figure 6.2(b)). We attribute them as La atoms considering their substitution for Sr in the SrO plane, which is consistent with the fact that these observed impurities are centered on Sr sites. On the other hand, the Ru-doped sample surface displays a few disorders of bright dots, but with no clear signature of individual Ru atoms (probably due to the weaker effect on the density of states). The bright dots are likely the adsorbed impurities on top of the surface and can be assigned to either excess strontium or oxygen atoms possibly resulting from the cleaving process. Remarkably, superimposed on the regular atomic lattices, we observed nanoscale corrugations seen as the bright (high) and dark (low) regions, indicating the spatial inhomogeneities in Ru-doped samples. We ascribe these corrugations to a variation of the electronic density of states rather than a topographic effect, since their magnitude strongly depends on the bias voltage. Indeed, as will be discussed later, such a highly inhomogeneous electronic structure with a characteristic length scale of a few nanometers might suggest the electronic phase separation in $Sr_3(Ir_{1-x}Ru_x)_2O_7$.

6.2 Insulator-to-metal transition in Ru-doped $Sr_3Ir_2O_7$

We start with the comprehensive examination of the Ru doping effect on the electronic structure of the Mott parent state in $Sr_3(Ir_{1-x}Ru_x)_2O_7$. By substituting Ru^{4+} ($4d^4$) for Ir^{4+} ($5d^5$), the

system is doped with holes and develops into metallic phase beyond the critical concentration at x~35% [139]. We obtained atomic resolution STM and STS data on $Sr_3(Ir_{1-x}Ru_x)_2O_7$ with various hole concentrations across the insulator-to-metal transition, over a wide range of Ru doings from the parent (x=0) insulator to the metallic (x=50%) compounds. Our first task is to study the topographs and the corresponding density of states of undoped and doped samples (figure 6.3). The square-shaped impurities in the parent compound were previously identified as apical oxygen vacancies in the SrO plane [20], based on the position of these chiral defects in between four neighboring Sr sites. The oxygen vacancies are common defects in layered oxides and are either inherent to the bulk of the samples or potentially enhanced by the cleaving process. In contrast to the parent compound, we find the Ru-doped samples have a far smaller percentage of chiral defects, and within our resolution we cannot resolve any. One possible reason is that the parent Ir327 samples we studied were self-selected to have a higher percentage of oxygen vacancies. On the other hand, we notice the inhomogeneous patches significantly manifesting in zoomed-in topographs for all the Ru-doped samples. To understand the microscopic changes in electronic structure associated with Ru doping, we measure the low-energy density of states across the Fermi level (E_F). Shown in figure 6.3(b) are the representative spectra in dark regions of the topographs far from obvious impurities. The parent compound shows a well-defined gap of ~150 meV, and the 5%Ru sample displays the similar insulating feature. Interestingly, as we go to x=35% (close to the MIT boundary) compound, we continue to find gapped spectrum with a gap size less than 100 meV. Finally, on the sample with x=50% which is above the transition point, the spectrum becomes V-shaped.

With a preliminary idea of what the typical spectra in dark areas look like, let us look at the local effects of Ru dopants on the electronic structure. In figure 6.4, we plot a series of tunneling spectra acquired along a line through the bright and dark regions on the 5%, 35% and 50% Ru-doped compounds. This is a useful starting point to learn the qualitative aspects of their LDOS behaviors. We find that the line cuts exhibit pronounced changes based on the spatial location in 5% and 35% Ru-doped samples, indicating a spatially inhomogeneous electronic structure. The d*I*/d*V* spectra evolve from the "gapped" ones with almost zero LDOS near E_F to more a metallic V-shape with growing density of states within the gap, as approaching to the brighter areas in the topographs. In other words, the spectra in the dark regions are significantly more insulating than the bright regions which correspond to the V-shaped spectra. Move on to the 50% sample, the spectra are globally gapless, which is in stark contrast to the lower dopings studied. However, by looking carefully into the line cut, the spectra also display a substantial degree of inhomogeneity with two distinct shapes in this nominal metal. Comparing to the suppressed V-shaped LDOS obtained at dark spots, the spectra taken at bright spots (the top spectrum of the line cut as the most prominent one) strongly resemble that of ruthenate $Sr_3Ru_2O_7$ [142]. Actually, this inhomogeneity was implied earlier when we showed the topograph in large field-of-view on the same compound, as illustrated in figure 6.2(a). In this sense, while the large concentration of Ru makes it impossible to distinguish individual Ru atoms, we infer that the bright patches on the topograph should be Ru-associated, considering their local electronic feature which is qualitatively similar to $Sr_3Ru_2O_7$.

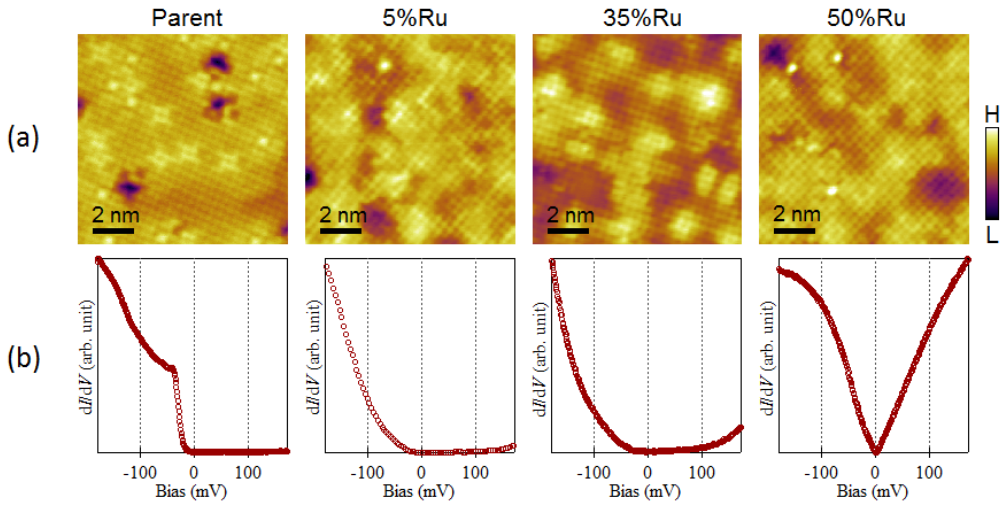

Figure 6.3: Electronic phase evolution in $Sr_3(Ir_{1-x}Ru_x)_2O_7$ with Ru concentrations from x=0 (parent) to x=50%. (a) Topographic images of $Sr_3(Ir_{1-x}Ru_x)_2O_7$. Even without obvious Ru-dopant signatures, inhomogeneous textures to different extent are clearly demonstrated on the patchy topographs. (b) Point spectra acquired in the dark regions (low DOS) of the corresponding sample surfaces for each Ru dopings. The evolution of the spectra qualitatively reflected an insulator-to-metal phase transition.

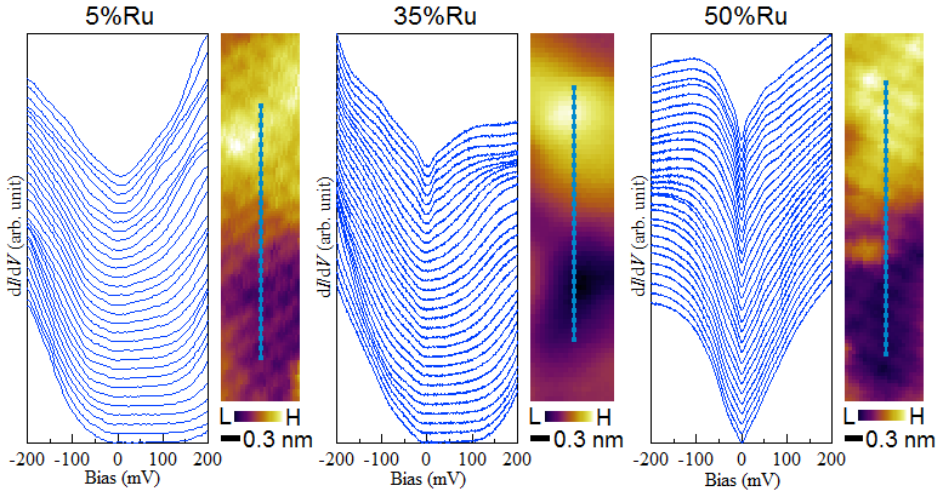

Figure 6.4: d*I*/d*V* line cuts across the MIT in 5%, 35% and 50%Ru-doped $Sr_3Ir_2O_7$. The associated topographic images indicate where the line cuts were obtained. The spectra in 5%Ru and 35%Ru compounds show the evolution from gapped to gapless, with the latter possessing smaller gap and more metallic behavior at the two ends. The spectra of 50%Ru-doped sample, however, exhibit a relatively more homogeneous V-shape along the whole line.

To better track and visualize the evolution of the local electronic structure in $Sr_3(Ir_{1-x}Ru_x)_2O_7$ as it approaching the MIT, we implement the LDOS mapping and calculate the average spectra binned by the gap magnitude for samples with x=5%, x=35% and x=38% (figure 6.5(a)). We see a systematic spectral variation, from mostly insulating for x=5% to barely metallic for x=38%. To quantify the spectral inhomogeneity for each doping, we look at the spatial distribution of d*I*/d*V* spectra at the atomic length scales. In order to achieve this, we locate a clean, atomically-flat area of the sample, and acquire d*I*/d*V* spectra on a densely-spaced pixel grid. By determining the magnitude of the gap at each pixel point, we create the characteristic spectral gap maps where the colors correspond to the spectral shapes (figure 6.5(b)). At x=5%, transport properties indicate very little change from the parent compound. Indeed, the majority of the sample is gapped according to our measurements, with an average gap of 72 meV. Notably, at substantial Ru doping x=35%, surprisingly large areas of the sample are still gapped as presented with blue color. This suggests that the doped holes in IrO_2 planes continue to remain localized even at high Ru concentrations. From x=5% to x=38%, the average gap decreases and the gap histogram shifts to lower energies (figure 6.5(c)). Moreover, the metallic regions (red color) grow in spatial extent until they percolate in the x=38% sample, which is in agreement with the percolation induced MIT proposed in earlier studies [139]. We therefore get the conclusion that the

mechanism of MIT in Ru-doped Ir327 system occurs through an effective filling up of the gap in a spatially inhomogeneous fashion.

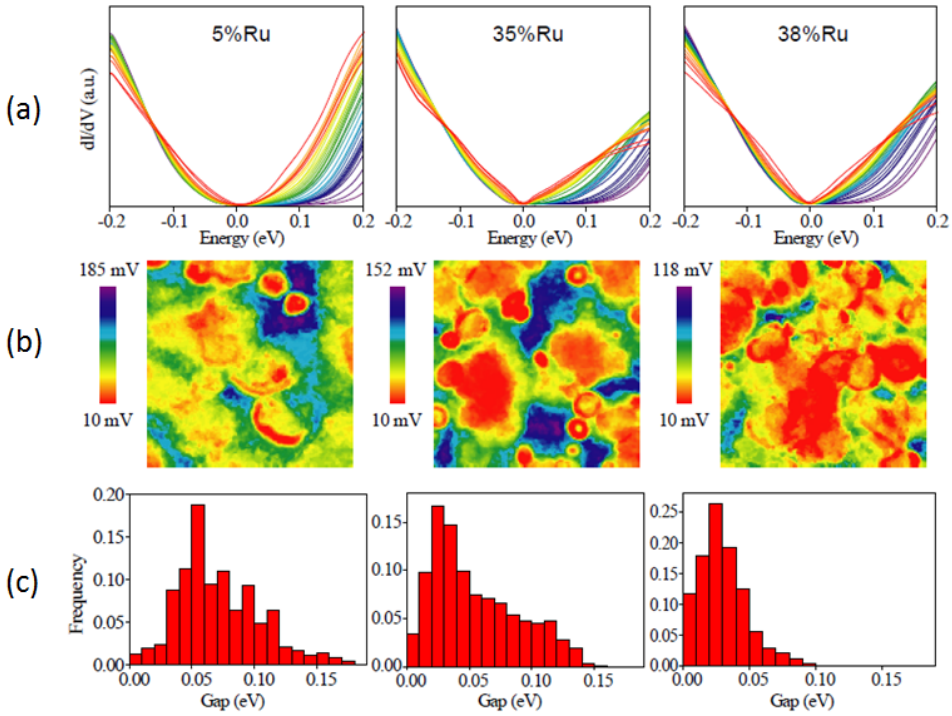

Figure 6.5: Spatial evolution of d*I*/d*V* spectra for 5%, 35% and 38% Ru dopings. (a) Averaged d*I*/d*V* spectra classified by the gap magnitude. The spectra are split into 32 groups with equal population, ranging from the ones with the largest gap (blue) to the ones with the smallest gap (red). (b) Gap maps corresponding to (a) showing the spatial inhomogeneity. Metallic region (red) expands as the Ru doping increases, indicating the trend towards MIT. (c) Histograms of the spectral gap magnitude. The average gap size shrinks with increasing Ru doping.

Now we discuss the physical origins of the inhomogeneity in the intrinsic LDOS of Ru-doped Ir327 system. The spatially inhomogeneous electronic states are inherent to doped Mott insulators, and it has been suggested that such an inhomogeneity is a key factor of high-

temperature superconductivity and colossal magnetoresistance [145][146]. There are two possible scenarios for the explanation of our observed electronic inhomogeneity within the IrO_2 plane. One is a poorly-screened impurity potential [147]. The Ru dopants are supposed to modify the electrostatic potential of the neighboring IrO_2 planes. In ordinary metals, the electrostatic potential is screened by itinerant carriers. While in semiconductors and insulators with poor screening, the effective screening length can be much longer which often induces electronic inhomogeneity. In doped Ir327, the close proximity to the Mott insulator can give rise to a nonlinear screening effect [148][149], hence a nanoscale electronic inhomogeneity may emerge.

Another possible origin of the observed inhomogeneity might be the electronic phase separation, which comes from the competing ordered states. In the naive phase separation picture, two distinct phases should be detected and the ratio of the two should change upon doping. In our case, the measurements on samples with different Ru dopings have demonstrated systematic evolution in both STM images and d*I*/d*V* spectra. We find the nanoscale mixture of high and low LDOS regions regardless of the ground state. The high LDOS (bright) area increases with increasing density of holes (figure 6.5(b)). Additionally, the in-plane doped Ru leads to the formation of metallic puddles and remains largely localized within a fully gapped spin-orbit Mott insulating background. These observations appear to be consistent with the electronic phase separation. Although additional ingredients cannot be completely ruled out and the poor screening impurity potential should be involved as well, a kind of electronic phase separation seems reasonable for the observed phenomena. In any event, we believe that strong

inhomogeneity across nanometer length scales in Ru-doped Ir327 represents the characteristic physics of the in-plane doped Mott insulator.

6.3 Electronic phase structure of La-doped $Sr_3Ir_2O_7$

Now let's turn to La-doped compound $(Sr_{1-x}La_x)_3Ir_2O_7$ with dilute concentration x=4%, which is close to the critical point of the insulator-to-metal transition [150]. Substitution of La^{3+} ions for Sr^{2+} ions in $Sr_3Ir_2O_7$ induces an electron doping in the SrO plane, where there are also defects of apical oxygen vacancies. Consistent with this we observed similar square-shaped impurities centered on Sr sites, which we identify as the La atoms. We first study the local DOS behavior in the vicinity of these defects, by measuring the high-resolution d*I*/d*V* spectra along a line through one single La dopant (figure 6.6(b)). We see that even at such a low doping, all the spectra display metallic shape homogeneously.

To further determine the effects of La dopants as a function of both position and energy, we obtained the LDOS maps with different bias and performed cross-correlation analysis [151], which can establish a statistical connection between the defects and the electronic heterogeneity. We calculated the correlation coefficients between the conductance maps (at bias energy +50 meV and -50 meV, respectively) and the defect distribution images, which are obtained by imposing a 2D Gaussian centered at each defect. The image with the Gaussian full width half maximum (FWHM) set to 1.4 nm is shown in figure 6.6(a). Although the correlation coefficient is not totally independent on the value of FWHM, the plots suggest very little change in it with the conductance at these two energies. In the meantime, the correlation coefficient is

almost zero for all the energies we have measured with setting FWHM to 1.4 nm, indicating a very weak local influence on the electronic DOS nearby these impurities.

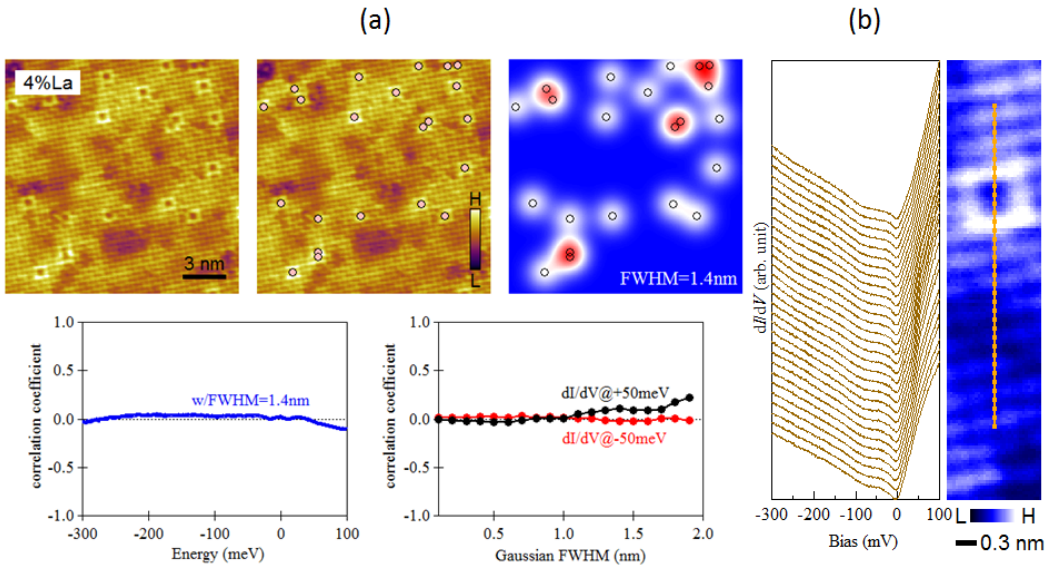

Figure 6.6: Electronic phase behavior of $Sr_3Ir_2O_7$ with slight La doping. (a) Shown in the upper row are the topographic images of 4%La-doped Ir327 with the major chemical defects (La atoms) marked by filled circles, as well as the defect distribution image obtained by integrating 2D Gaussian (FWHM=1.4nm) centered at defects. Correlation results are plotted in the lower row. Correlation coefficients between defect image with 1.4 nm FWHM and conductance maps at various energies, and between conductance images at ±50 meV and defect distribution images with various Gaussian FWHM values, are both found to be extremely small. (b) d*I*/d*V* line cut across one of the La impurities exhibits very homogeneous V-shaped spectra.

Transport results have shown a MIT in $Sr_3Ir_2O_7$ via a dilute electron doping, and that a robust metallic state is readily formed by mere 5% doping of La. From our observation in the line cuts as well as the spectral mapping, a few La carriers doped into the SrO planes can radically alter

the Mott insulating ground phase and render the system achieve metallic state entirely. In particular, we notice that such a behavior is quite different as that with the Ru carriers doped into the IrO_2 planes. A comparison of two, La doping and Ru doping, indicates that the fundamental mechanism of carrier doping effect can be drastically different based on the layer at which doping occurs even within the same compound.

6.4 Mechanism of phase transition induced by dopants at different sites

To start with, the effect of La doping into the SrO plane are far from local and therefore cannot be explained by changes in local rotation of the oxygen octahedra or local tilt (although this could be an effect of the doping). Rather, doping in the SrO plane seems to result in changes of the whole band structure close to the Fermi energy, over large length scales. In fact, A-site doping in perovskite oxides is historically expected to control the filling of *d*-bands by donating their valence electrons to the entire system. The well-established metallic states in Ir327 with slight La doping (A-site substitution) can therefore arise from these additional electrons which would fill the states in the gap and push the Fermi level into the bottom of the upper J_{eff}=1/2 Hubbard band [150]. Consequently, the resulting doping mechanism gives rise to a rapid suppression of the Mott phase via shifting the Fermi energy.

In contrast, doping in the IrO_2 plane has a local effect on the electronic structure with nanoscale regions that continue to show insulating gaps even at a doping level where on the average, every third Ir atom should be replaced by a Ru. This behavior strongly suggests that the holes doped into the IrO_2 plane remain largely localized and a percolation driven metal-insulator

phase transition occurs with Ru doping [152]. The localization of Ru carriers into a phase-separated ground state remarkably parallels the strongly correlated phase diagram of 3*d*-TMO [112][153], revealing that correlation physics can play a dominant role in the electronic phase formation of a doped spin-orbit Mott insulator.

6.5 Electronic phase structure of La-doped Sr_2IrO_4

Besides $Sr_3Ir_2O_7$ (Ir327), we have also studied single crystals of Sr_2IrO_4 (Ir214) doped with ~5% La, $(Sr_{0.95}La_{0.05})_2IrO_4$. Our spatially resolved LDOS measurements on this sample, however, reveal an inhomogeneous electronic landscape. In the topographic image shown in figure 6.7(a), we see the same square-shaped impurities as in La-doped Ir327 which are supposed to be La atoms, but on a more patchy background. Figure 6.7(b) indicates the comparison of the representative d*I*/d*V* spectra averaged over the dark regions and right above the impurity spots across a wide energy range (±600 meV). It is evident that the LDOS in dark region far away from the impurities is substantially more insulating, with a prominent enhancement of the gap magnitude.

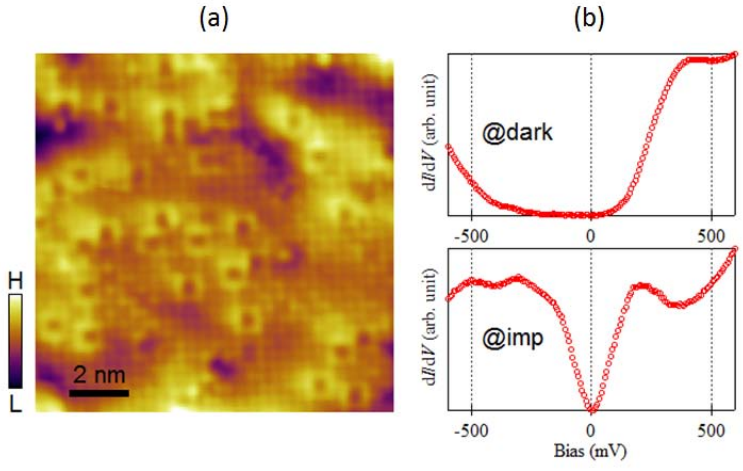

Figure 6.7: Electronic phase behavior of La-doped Sr_2IrO_4. (a) Topographic image on the surface of $(Sr_{0.95}La_{0.05})_2IrO_4$ exhibiting a small percentage of La defects within a patchy background. (b) Averaged spectra in dark areas far away from the impurities and right on the impurity spots seen in (a). The spectra display significantly different shapes, indicating an inhomogeneous electronic structure on this sample surface.

To examine the overall electronic properties of this sample, we further obtained the spectral intensity histogram image of a 128*128 tunneling spectra in a 15nm×15nm area (figure 6.8(a)). As illustrated, large spectral spatial variations with a clear evolution of the line-shape appear between E_F and -200 mV. In order to correlate this spectral evolution with the corresponding topograph, we plot a line cut going through one of the La impurities and find that the spectral line-shape is apparently correlated with the presence of these impurities (figure 6.8(b)). Therefore, we infer that the La dopants have locally created some in-gap spectral weight and thus lead to more metallic phase in Ir214, which coexists with the other fully-gapped insulating ones.

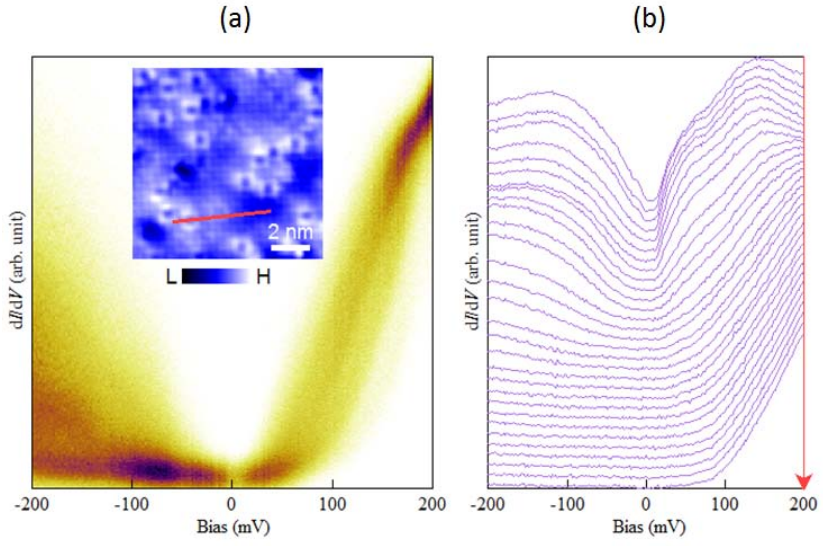

Figure 6.8: Spatially spectral evolution in La-doped Sr_2IrO_4. (a) Histogram of the 128*128 spectra obtained in a 15nm area seen in the inset, demonstrating considerable spatial variation. (b) d*I*/d*V* line cut across one of the La impurities indicated in the inset of (a). The line cut shows an evident correlation between the spectral line-shape and the presence of La impurities.

It is generally recognized that the magnetic ground state for Sr_2IrO_4 and $Sr_3Ir_2O_7$ is antiferromagnetic which is closely associated with the rotation of the IrO_6 octahedra about the c-axis [154]. According to transport results, although a metallic state is established in La-doped Ir214 with quite a few La substitutions [155], the behavior of the magnetic order variation in response to the electron doping sharply contrasts that for La-doped Ir327 [150]. More relevant to our data, comparing to Sr_2IrO_4 owning an intrinsic insulating gap of about 600 meV [156], $Sr_3Ir_2O_7$ has a much smaller gap and is close to the MIT crossover. As a result, the Mott ground state of $Sr_3Ir_2O_7$ is highly susceptible to small external perturbations, such as an effective chemical doping of La. Practically, this sensitivity of the band structure indicates the tunable nature of the Ir327 compounds, which is an important aspect in realizing emergent phases at the boundary of a spin-orbit induced correlated insulator.

6.6 Conclusions

In summary, our STM and STS measurements on Ru-doped Ir327, La-doped Ir327 as well as La-doped Ir214 have revealed pronounced electronic structures near the insulator-to-metal transitions in doped Mott insulators. This study offers a unique opportunity to determine how dopants at particular lattice sites alter the LDOS from insulating to metallic phases. Equally

importantly, our data provide critical information for tuning low-energy electronic structure of iridates, a crucial component for realizing emergent phases such as superconductivity. In any case, we believe that the investigations of real-space physics in doped Mott insulators are very essential to understand the details of metal-insulator transition.

Chapter 7

Concluding remarks and outlook

The In this thesis, we deal with two main categories of materials associated with strong SOC, Bi-based topological insulators and Ir-based transition metal oxides. We concentrate on the spectroscopic investigations of their surface electronic structures as well as ordered phases within atomic scales via STM/STS. A brief summary on the major findings of our research work is given below.

In chapter 3, we utilize Fourier-transform STS to visualize the QPI patterns in the TI material Bi_2Te_3 over a significantly wide energy range. We demonstrate the robustness of SS in this material, with the discovery that the linear dispersion along the Γ-M direction can persist up to ~700 meV above the Dirac point. We further find an unusual interference pattern with the appearance of new dispersive QPI modes at even higher energies, which we propose to be originated from an impurity-induced spin-orbit scattering process possibly associated with some common impurities in this material such as a Te vacancy or a Bi anti-site defect. This additional effect in TIs was theoretically predicted but not experimentally observed so far.

In chapter 4, we probe the SS evolution in $(Bi_{1-x}In_x)_2Se_3$ series in order to understand the microscopic details of the quantum phase transition in this system. We track the surface band dispersions extrapolated from Landau spectroscopy for samples with different composition,

which qualitatively reflect the corresponding transformation of the surface Dirac cone structure. On samples at x=0.05, our LDOS measurements suggest a missing of the topologically protected Dirac point and the resultant variation of well-defined surface Dirac cone, which is in sharp contrast to lower dopings. We also acquire a quadratic-like *E-k* relation instead of the linear dispersion expected in topological phases. Hence we preliminarily infer that a topological phase transition occurs in $(Bi_{1-x}In_x)_2Se_3$ system around x=0.05, where the surface Dirac cone is probably gapped out.

In chapter 6, we explore the electronic phase transitions in the bilayer 5*d*-iridate $Sr_3Ir_2O_7$ which was recently pointed out as a spin-orbit driven Mott insulator, through chemical doping with particular ionic substitution. We examine the carrier-induced electronic phase behavior in doped $Sr_3Ir_2O_7$ as the system is driven from insulating to metallic phase, by introducing in-plane dopant Ru and out-of-plane dopant La, respectively. Our data exhibiting drastic difference of MIT behavior in response to defects at different lattice sites can be explained in regards of the relativity of the local effect on the modification of the parent J_{eff}=1/2 Mott phase. This comprehensive study provides deep insights into the role and influence of the dopants in Mott insulators and can serve as important indication for the realization of emergent phases at the boundary of a spin-orbit induced correlated oxide.

As presented, our experimental work has revealed the rich physics in the distinct surface states of three-dimensional TIs, and has emphasized the pronounced electronic structures near the insulator-to-metal transition in doped Mott insulators. As is well known, the variety of remarkable physical properties inherent to topological insulators and 5*d*-iridates are leading

these unique materials towards promising applications, including new types of spintronic devices [157][158] and Majorana Fermions [159], as well as topological Mott insulators [160][161] and Weyl semimetals [162]. In the meantime, there still remain many challenges which require full addressing theoretically and experimentally. It is our hope that the studies we have done can encourage the development of new theoretical models for these exciting materials to be investigated in the future.

Bibliography

[1] Binnig, G., Rohrer, H., Gerber, C. & Weibel, E. Surface Studies by Scanning Tunneling Microscopy. Phys. Rev. Lett. 49, 57–61 (1982).

[2] Binnig, G. & Rohrer, H. Scanning tunneling microscopy. Surf. Sci. 126, 236–244 (1983).

[3] L. D. Landau and E. M. Lifshits. Quantum mechanics: non-relativistic theory. Butterworth-Heinemann, 1981.

[4] C. Julian Chen. Introduction to Scanning Tunneling Microscopy (Monographs on the Physics and Chemistry of Materials). Oxford University Press, 2007.

[5] Bardeen, J. Tunnelling from a Many-Particle Point of View. Phys. Rev. Lett. 6, 57–59 (1961).

[6] Cohen, M., Falicov, L. & Phillips, J. Superconductive Tunneling. Phys. Rev. Lett. 8, 316–318 (1962).

[7] J. J. Sakurai. Modern Quantum Mechanics. Addison Wesley, 1993.

[8] R. Shankar. Principles of Quantum Mechanics. Springer, 1994.

[9] Ma, J.-H. et al. Coexistence of Competing Orders with Two Energy Gaps in Real and Momentum Space in the High Temperature Superconductor $Bi_2Sr_{2-x}La_xCuO_{6+\delta}$. Phys. Rev. Lett. 101, 207002 (2008).

[10] Niestemski, F. C. et al. A distinct bosonic mode in an electron-doped high-transition-temperature superconductor. Nature 450, 1058–61 (2007).

[11] Crommie, M. F., Lutz, C. P. & Eigler, D. M. Imaging standing waves in a two-dimensional electron gas. Nature 363, 524–527 (1993).

[12] Hasegawa, Y. & Avouris, P. Direct observation of standing wave formation at surface steps using scanning tunneling spectroscopy. Phys. Rev. Lett. 71, 1071–1074 (1993).

[13] David J. Griffiths. Introduction to Electrodynamics. Addison Wesley, 1980.

[14] John H. Davies. The Physics of Low-Dimensional Semiconductors. Cambridge University Press, 1997.

[15] Castro Neto, A. H., Peres, N. M. R., Novoselov, K. S. & Geim, A. K. The electronic properties of graphene. Rev. Mod. Phys. 81, 109–162 (2009).

[16] Miller, D. L. et al. Observing the quantization of zero mass carriers in graphene. Science 324, 924–7 (2009).

[17] Hanaguri, T., Niitaka, S., Kuroki, K. & Takagi, H. Unconventional s-wave superconductivity in Fe(Se,Te). Science 328, 474–6 (2010).

[18] Cheng, P. et al. Landau Quantization of Topological Surface States in Bi_2Se_3. Phys. Rev. Lett. 105, 076801 (2010).

[19] Pan, S. H., Hudson, E. W. & Davis, J. C. 3He refrigerator based very low temperature scanning tunneling microscope. Rev. Sci. Instrum. 70, 1459 (1999).

[20] Okada, Y. et al. Imaging the evolution of metallic states in a correlated iridate. Nat. Mater. 12, 707–13 (2013).

[21] Kardar, M. Statistical Physics of Particles. Cambridge University Press, 2007.

[22] L. D. Landau and E. M. Lifshitz. Statistical Physics. Butterworth-Heinemann, 1980.

[23] Klitzing, K., Dorda, G. & Pepper, M. New Method for High-Accuracy Determination of the Fine-Structure Constant Based on Quantized Hall Resistance. Phys. Rev. Lett. 45, 494–497 (1980).

[24] Tsui, D. C., Stormer, H. L. & Gossard, A. C. Two-Dimensional Magnetotransport in the Extreme Quantum Limit. Phys. Rev. Lett. 48, 1559–1562 (1982).

[25] Kane, C. L. & Mele, E. J. Z_2 Topological Order and the Quantum Spin Hall Effect. Phys. Rev. Lett. 95, 146802 (2005).

[26] Von Klitzing, K. Developments in the quantum Hall effect. Philos. Trans. A. Math. Phys. Eng. Sci. 363, 2203–19 (2005).

[27] Thouless, D., Kohmoto, M., Nightingale, M. & den Nijs, M. Quantized Hall Conductance in a Two-Dimensional Periodic Potential. Phys. Rev. Lett. 49, 405–408 (1982).

[28] Berry, M. V. Quantal Phase Factors Accompanying Adiabatic Changes. Proc. R. Soc. A Math. Phys. Eng. Sci. 392, 45–57 (1984).

[29] Halperin, B. Quantized Hall conductance, current-carrying edge states, and the existence of extended states in a two-dimensional disordered potential. Phys. Rev. B 25, 2185–2190 (1982).

[30] Hasan, M. Z. & Kane, C. L. Colloquium: Topological insulators. Rev. Mod. Phys. 82, 3045–3067 (2010).

[31] Kane, C. L. & Mele, E. J. Quantum Spin Hall Effect in Graphene. Phys. Rev. Lett. 95, 226801 (2005).

[32] Bernevig, B. A. & Zhang, S.-C. Quantum Spin Hall Effect. Phys. Rev. Lett. 96, 106802 (2006).

[33] Wu, C., Bernevig, B. A. & Zhang, S.-C. Helical Liquid and the Edge of Quantum Spin Hall Systems. Phys. Rev. Lett. 96, 106401 (2006).

[34] Fu, L., Kane, C. & Mele, E. Topological Insulators in Three Dimensions. Phys. Rev. Lett. 98, 106803 (2007).

[35] Moore, J. & Balents, L. Topological invariants of time-reversal-invariant band structures. Phys. Rev. B 75, 121306 (2007).

[36] Roy, R. Topological phases and the quantum spin Hall effect in three dimensions. Phys. Rev. B 79, 195322 (2009).

[37] Fu, L. & Kane, C. Topological insulators with inversion symmetry. Phys. Rev. B 76, 045302 (2007).

[38] Moore, J. Topological insulators: The next generation. Nat. Phys. 5, 378–380 (2009).

[39] Suzuura, H. & Ando, T. Crossover from Symplectic to Orthogonal Class in a Two-Dimensional Honeycomb Lattice. Phys. Rev. Lett. 89, 266603 (2002).

[40] Kohmoto, M., Halperin, B. & Wu, Y.-S. Diophantine equation for the three-dimensional quantum Hall effect. Phys. Rev. B 45, 13488–13493 (1992).

[41] Ran, Y., Zhang, Y. & Vishwanath, A. One-dimensional topologically protected modes in topological insulators with lattice dislocations. Nat. Phys. 5, 298–303 (2009).

[42] Fu, L. & Kane, C. Time reversal polarization and a Z_2 adiabatic spin pump. Phys. Rev. B 74, 195312 (2006).

[43] Bernevig, B. A., Hughes, T. L. & Zhang, S.-C. Quantum spin Hall effect and topological phase transition in HgTe quantum wells. Science 314, 1757–61 (2006).

[44] König, M. et al. Quantum spin hall insulator state in HgTe quantum wells. Science 318, 766–70 (2007).

[45] Hsieh, D. et al. A topological Dirac insulator in a quantum spin Hall phase. Nature 452, 970–4 (2008).

[46] Liu, Y. & Allen, R. Electronic structure of the semimetals Bi and Sb. Phys. Rev. B 52, 1566–1577 (1995).

[47] Wolff, P. A. Matrix elements and selection rules for the two-band model of bismuth. J. Phys. Chem. Solids 25, 1057–1068 (1964).

[48] Hsieh, D. et al. Observation of unconventional quantum spin textures in topological insulators. Science 323, 919–22 (2009).

[49] Roushan, P. et al. Topological surface states protected from backscattering by chiral spin texture. Nature 460, 1106–9 (2009).

[50] Xia, Y. et al. Observation of a large-gap topological-insulator class with a single Dirac cone on the surface. Nat. Phys. 5, 398–402 (2009).

[51] Zhang, H. et al. Topological insulators in Bi_2Se_3, Bi_2Te_3 and Sb_2Te_3 with a single Dirac cone on the surface. Nat. Phys. 5, 438–442 (2009).

[52] Fu, L. & Kane, C. Superconducting Proximity Effect and Majorana Fermions at the Surface of a Topological Insulator. Phys. Rev. Lett. 100, 096407 (2008).

[53] Qi, X.-L., Li, R., Zang, J. & Zhang, S.-C. Inducing a magnetic monopole with topological surface States. Science 323, 1184–7 (2009).

[54] Li, R., Wang, J., Qi, X.-L. & Zhang, S.-C. Dynamical axion field in topological magnetic insulators. Nat. Phys. 6, 284–288 (2010).

[55] Tse, W.-K. & MacDonald, A. H. Giant Magneto-Optical Kerr Effect and Universal Faraday Effect in Thin-Film Topological Insulators. Phys. Rev. Lett. 105, 057401 (2010).

[56] Ghaemi, P., Mong, R. S. K. & Moore, J. E. In-Plane Transport and Enhanced Thermoelectric Performance in Thin Films of the Topological Insulators Bi_2Te_3 and Bi_2Se_3. Phys. Rev. Lett. 105, 166603 (2010).

[57] Urazhdin, S. et al. Surface effects in layered semiconductors Bi_2Se_3 and Bi_2Te_3. Phys. Rev. B 69, 085313 (2004).

[58] Black, J., Conwell, E. M., Seigle, L. & Spencer, C. W. Electrical and optical properties of some $M_2^{V-B}N_3^{VI-B}$ semiconductors. J. Phys. Chem. Solids 2, 240–251 (1957).

[59] Thomas, G. et al. Large electronic-density increase on cooling a layered metal: Doped Bi_2Te_3. Phys. Rev. B 46, 1553–1556 (1992).

[60] Chen, Y. L. et al. Experimental realization of a three-dimensional topological insulator, Bi_2Te_3. Science 325, 178–81 (2009).

[61] Hasan, M., Lin, H. & Bansil, A. Warping the cone on a Topological Insulator. Physics 2, 108 (2009).

[62] Mishra, S. K., Satpathy, S. & Jepsen, O. Electronic structure and thermoelectric properties of bismuth telluride and bismuth selenide. J. Phys. Condens. Matter 9, 461–470 (1997).

[63] Fu, L. Hexagonal Warping Effects in the Surface States of the Topological Insulator Bi_2Te_3. Phys. Rev. Lett. 103, 266801 (2009).

[64] Alpichshev, Z. et al. STM Imaging of Electronic Waves on the Surface of Bi_2Te_3: Topologically Protected Surface States and Hexagonal Warping Effects. Phys. Rev. Lett. 104, 016401 (2010).

[65] Zhang, T. et al. Experimental Demonstration of Topological Surface States Protected by Time-Reversal Symmetry. Phys. Rev. Lett. 103, 266803 (2009).

[66] Wang, J. et al. Power-law decay of standing waves on the surface of topological insulators. Phys. Rev. B 84, 235447 (2011).

[67] Hsieh, D. et al. A tunable topological insulator in the spin helical Dirac transport regime. Nature 460, 1101–5 (2009).

[68] Xu, S.-Y. et al. Topological phase transition and texture inversion in a tunable topological insulator. Science 332, 560–4 (2011).

[69] Okada, Y. et al. Ripple-modulated electronic structure of a 3D topological insulator. Nat. Commun. 3, 1158 (2012).

[70] Hor, Y. et al. p-type Bi_2Se_3 for topological insulator and low-temperature thermoelectric applications. Phys. Rev. B 79, 195208 (2009).

[71] Urazhdin, S. et al. Scanning tunneling microscopy of defect states in the semiconductor Bi_2Se_3. Phys. Rev. B 66, 161306 (2002).

[72] Okada, Y. et al. Observation of Dirac node formation and mass acquisition in a topological crystalline insulator. Science 341, 1496–9 (2013).

[73] Okada, Y. et al. Direct Observation of Broken Time-Reversal Symmetry on the Surface of a Magnetically Doped Topological Insulator. Phys. Rev. Lett. 106, 206805 (2011).

[74] C. Kittel. Introduction to solid state Physics. John Wiley & Sons, 1996.

[75] Friedel, J. Metallic alloys. Nuovo Cim. 7, 287–311 (1958).

[76] McElroy, K. et al. Relating atomic-scale electronic phenomena to wave-like quasiparticle states in superconducting $Bi_2Sr_2CaCu_2O_{8+\delta}$. Nature 422, 592–6 (2003).

[77] Hoffman, J. E. et al. Imaging quasiparticle interference in $Bi_2Sr_2CaCu_2O_{8+\delta}$. Science 297, 1148–51 (2002).

[78] Allan, M. P. et al. Anisotropic Energy Gaps of Iron-Based Superconductivity from Intraband Quasiparticle Interference in LiFeAs. Science 336, 563–567 (2012).

[79] Allan, M. P. et al. Imaging Cooper pairing of heavy fermions in $CeCoIn_5$. Nat. Phys. 9, 468–473 (2013).

[80] Zeljkovic, I. et al. Mapping the unconventional orbital texture in topological crystalline insulators. Nat. Phys. 10, 572-577 (2014).

[81] Raghu, S., Chung, S. B., Qi, X.-L. & Zhang, S.-C. Collective Modes of a Helical Liquid. Phys. Rev. Lett. 104, 116401 (2010).

[82] Liu, Q., Qi, X.-L. & Zhang, S.-C. Stationary phase approximation approach to the quasiparticle interference on the surface of a strong topological insulator. Phys. Rev. B 85, 125314 (2012).

[83] Lee, W.-C., Wu, C., Arovas, D. P. & Zhang, S.-C. Quasiparticle interference on the surface of the topological insulator Bi_2Te_3. Phys. Rev. B 80, 245439 (2009).

[84] Hsieh, D. et al. Observation of Time-Reversal-Protected Single-Dirac-Cone Topological-Insulator States in Bi_2Te_3 and Sb_2Te_3. Phys. Rev. Lett. 103, 146401 (2009).

[85] Qi, X.-L., Hughes, T. L. & Zhang, S.-C. Topological field theory of time-reversal invariant insulators. Phys. Rev. B 78, 195424 (2008).

[86] Yan, B. et al. Theoretical prediction of topological insulators in thallium-based III-V-VI_2 ternary chalcogenides. EPL (Europhysics Lett.) 90, 37002 (2010).

[87] Qi, X.-L. & Zhang, S.-C. Topological insulators and superconductors. Rev. Mod. Phys. 83, 1057–1110 (2011).

[88] Sato, T. et al. Unexpected mass acquisition of Dirac fermions at the quantum phase transition of a topological insulator. Nat. Phys. 7, 840–844 (2011).

[89] Brahlek, M. et al. Topological-Metal to Band-Insulator Transition in $(Bi_{1-x}In_x)_2Se_3$ Thin Films. Phys. Rev. Lett. 109, 186403 (2012).

[90] Wu, L. et al. A sudden collapse in the transport lifetime across the topological phase transition in $(Bi_{1-x}In_x)_2Se_3$. Nat. Phys. 9, 410–414 (2013).

[91] DiSalvo, F. J. Thermoelectric Cooling and Power Generation. Science 285, 703–706 (1999).

[92] Larson, P. et al. Electronic structure of Bi_2X_3 (X=S, Se, T) compounds: Comparison of theoretical calculations with photoemission studies. Phys. Rev. B 65, 085108 (2002).

[93] Mooser, E. & Pearson, W. New Semiconducting Compounds. Phys. Rev. 101, 492–493 (1956).

[94] Watanabe, Y., Kaneko, S., Kawazoe, H. & Yamane, M. Imperfections in amorphous chalcogenides. IV. A model of electrical conduction processes in amorphous and crystalline In_2Se_3. Phys. Rev. B 40, 3133–3142 (1989).

[95] Wang, Z. Y. et al. Superlattices of Bi_2Se_3/In_2Se_3: Growth characteristics and structural properties. Appl. Phys. Lett. 99, 023112 (2011).

[96] Hanaguri, T., Igarashi, K., Kawamura, M., Takagi, H. & Sasagawa, T. Momentum-resolved Landau-level spectroscopy of Dirac surface state in Bi_2Se_3. Phys. Rev. B 82, 081305 (2010).

[97] Morgenstern, M. et al. Low temperature scanning tunneling spectroscopy on InAs(110). J. Electron Spectros. Relat. Phenomena 109, 127–145 (2000).

[98] Becker, S., Liebmann, M., Mashoff, T., Pratzer, M. & Morgenstern, M. Scanning tunneling spectroscopy of a dilute two-dimensional electron system exhibiting Rashba spin splitting. Phys. Rev. B 81, 155308 (2010).

[99] Li, G., Luican, A. & Andrei, E. Y. Scanning Tunneling Spectroscopy of Graphene on Graphite. Phys. Rev. Lett. 102, 176804 (2009).

[100] Zheng, Y. & Ando, T. Hall conductivity of a two-dimensional graphite system. Phys. Rev. B 65, 245420 (2002).

[101] Jiang, Y. et al. Mass acquisition of Dirac fermions in Cr-doped topological insulator Sb_2Te_3 films. arXiv: 1305.3766 (2013).

[102] Okada, Y. et al. Visualizing Landau Levels of Dirac Electrons in a One-Dimensional Potential. Phys. Rev. Lett. 109, 166407 (2012).

[103] Mott, N. F. The Basis of the Electron Theory of Metals, with Special Reference to the Transition Metals. Proc. Phys. Soc. Sect. A 62, 416–422 (1949).

[104] Mott, N. F. & Peierls, R. Discussion of the paper by de Boer and Verwey. Proc. Phys. Soc. 49, 72–73 (1937).

[105] Kim, B. et al. Novel J_{eff}=1/2 Mott State Induced by Relativistic Spin-Orbit Coupling in Sr_2IrO_4. Phys. Rev. Lett. 101, 076402 (2008).

[106] Kim, B. J. et al. Phase-sensitive observation of a spin-orbital Mott state in Sr_2IrO_4. Science 323, 1329–32 (2009).

[107] Moon, S. et al. Dimensionality-Controlled Insulator-Metal Transition and Correlated Metallic State in 5d Transition Metal Oxides $Sr_{n+1}Ir_nO_{3n+1}$ (n=1, 2, and ∞). Phys. Rev. Lett. 101, 226402 (2008).

[108] Shitade, A. et al. Quantum Spin Hall Effect in a Transition Metal Oxide Na_2IrO_3. Phys. Rev. Lett. 102, 256403 (2009).

[109] Ye, F. et al. Direct evidence of a zigzag spin-chain structure in the honeycomb lattice: A neutron and x-ray diffraction investigation of single-crystal Na_2IrO_3. Phys. Rev. B 85, 180403 (2012).

[110] C. N. R. Rao and B. Raveau. Transition Metal Oxides: Structure, Properties, and Synthesis of Ceramic Oxides. John Wiley & Sons, 1998.

[111] Geballe, T. H. & Hulm, J. K. Superconductivity--the state that came in from the cold. Science 239, 367–75 (1988).

[112] Dagotto, E., Hotta, T. & Moreo, A. Colossal magnetoresistant materials: the key role of phase separation. Phys. Rep. 344, 1–153 (2001).

[113] Maeno, Y. et al. Superconductivity in a layered perovskite without copper. Nature 372, 532–534 (1994).

[114] Imada, M., Fujimori, A. & Tokura, Y. Metal-insulator transitions. Rev. Mod. Phys. 70, 1039–1263 (1998).

[115] Bednorz, J. G. & M ller, K. A. Possible high T_c superconductivity in the Ba-La-Cu-O system. Zeitschrift für Phys. B Condens. Matter 64, 189–193 (1986).

[116] Fujimori, A. et al. Evolution of the spectral function in Mott-Hubbard systems with d^1 configuration. Phys. Rev. Lett. 69, 1796–1799 (1992).

[117] Lee, J. et al. Optical investigation of the electronic structures of $Y_2Ru_2O_7$, $CaRuO_3$, $SrRuO_3$, and $Bi_2Ru_2O_7$. Phys. Rev. B 64, 245107 (2001).

[118] J. Singleton. Band theory and electronic properties of solids. Oxford University Press, 2001.

[119] Mattheiss, L. Band Structure and Fermi Surface of ReO_3. Phys. Rev. 181, 987–1000 (1969).

[120] Mattheiss, L. Electronic structure of RuO_2, OsO_2, and IrO_2. Phys. Rev. B 13, 2433–2450 (1976).

[121] Cao, G. et al. Non-Fermi-liquid behavior in nearly ferromagnetic $SrIrO_3$ single crystals. Phys. Rev. B 76, 100402 (2007).

[122] Erickson, A. et al. Ferromagnetism in the Mott Insulator Ba_2NaOsO_6. Phys. Rev. Lett. 99, 016404 (2007).

[123] Cao, G., Bolivar, J., McCall, S., Crow, J. & Guertin, R. Weak ferromagnetism, metal-to-nonmetal transition, and negative differential resistivity in single-crystal Sr_2IrO_4. Phys. Rev. B 57, R11039–R11042 (1998).

[124] Cao, G. et al. Anomalous magnetic and transport behavior in the magnetic insulator $Sr_3Ir_2O_7$. Phys. Rev. B 66, 214412 (2002).

[125] Rossnagel, K. Spin-orbit coupling in the band structure of reconstructed 1*T*-TaS_2. Phys. Rev. B 73, 073106 (2006).

[126] Mizokawa, T. & Fujimori, A. Electronic structure and orbital ordering in perovskite-type 3d transition-metal oxides studied by Hartree-Fock band-structure calculations. Phys. Rev. B 54, 5368–5380 (1996).

[127] Goodenough, J. Spin-Orbit-Coupling Effects in Transition-Metal Compounds. Phys. Rev. 171, 466–479 (1968).

[128] Jin, H., Jeong, H., Ozaki, T. & Yu, J. Anisotropic exchange interactions of spin-orbit-integrated states in Sr_2IrO_4. Phys. Rev. B 80, 075112 (2009).

[129] Ruddlesden, S. N. & Popper, P. New compounds of the K_2NIF_4 type. Acta Crystallogr. 10, 538–539 (1957).

[130] Ruddlesden, S. N. & Popper, P. The compound $Sr_3Ti_2O_7$ and its structure. Acta Crystallogr. 11, 54–55 (1958).

[131] Moritomo, Y., Asamitsu, A., Kuwahara, H. & Tokura, Y. Giant magnetoresistance of manganese oxides with a layered perovskite structure. Nature 380, 141–144 (1996).

[132] Cao, G., Korneta, O., Chikara, S., DeLong, L. E. & Schlottmann, P. Non-Fermi-liquid behavior in single-crystal $CaRuO_3$: Comparison to ferromagnetic $SrRuO_3$. Solid State Commun. 148, 305–309 (2008).

[133] Kini, N. S., Strydom, A. M., Jeevan, H. S., Geibel, C. & Ramakrishnan, S. Transport and thermal properties of weakly ferromagnetic Sr_2IrO_4. J. Phys. Condens. Matter 18, 8205–8216 (2006).

[134] Boseggia, S. et al. Antiferromagnetic order and domains in $Sr_3Ir_2O_7$ probed by x-ray resonant scattering. Phys. Rev. B 85, 184432 (2012).

[135] Dhital, C. et al. Spin ordering and electronic texture in the bilayer iridate $Sr_3Ir_2O_7$. Phys. Rev. B 86, 100401 (2012).

[136] Lee, P. a. & Wen, X.-G. Doping a Mott insulator: Physics of high-temperature superconductivity. Rev. Mod. Phys. 78, 17–85 (2006).

[137] Eisaki, H. et al. Effect of chemical inhomogeneity in bismuth-based copper oxide superconductors. Phys. Rev. B 69, 064512 (2004).

[138] Mathieu, R. et al. Impurity-induced transition to a Mott insulator in $Sr_3Ru_2O_7$. Phys. Rev. B 72, 092404 (2005).

[139] Dhital, C. et al. Carrier localization and electronic phase separation in a doped spin-orbit-driven Mott phase in $Sr_3(Ir_{1-x}Ru_x)_2O_7$. Nat. Commun. 5, 3377 (2014).

[140] Dagotto, E. Complexity in strongly correlated electronic systems. Science 309, 257–62 (2005).

[141] Pan, S. H. et al. Microscopic electronic inhomogeneity in the high-Tc superconductor $Bi_2Sr_2CaCu_2O_{8+x}$. Nature 413, 282–5 (2001).

[142] Iwaya, K. et al. Local Tunneling Spectroscopy across a Metamagnetic Critical Point in the Bilayer Ruthenate $Sr_3Ru_2O_7$. Phys. Rev. Lett. 99, 057208 (2007).

[143] Lee, J. et al. Heavy d-electron quasiparticle interference and real-space electronic structure of $Sr_3Ru_2O_7$. Nat. Phys. 5, 800–804 (2009).

[144] Li, Q. et al. Atomically resolved spectroscopic study of Sr_2IrO_4: experiment and theory. Sci. Rep. 3, 3073 (2013).

[145] Kivelson, S. A., Fradkin, E. & Emery, V. J. Electronic liquid-crystal phases of a doped Mott insulator. Nature 393, 550–553 (1998).

[146] Burgy, J., Mayr, M., Martin-Mayor, V., Moreo, A. & Dagotto, E. Colossal Effects in Transition Metal Oxides Caused by Intrinsic Inhomogeneities. Phys. Rev. Lett. 87, 277202 (2001).

[147] Kohsaka, Y. et al. Imaging Nanoscale Electronic Inhomogeneity in the Lightly Doped Mott Insulator $Ca_{2-x}Na_xCuO_2Cl_2$. Phys. Rev. Lett. 93, 097004 (2004).

[148] Wang, Q.-H., Han, J. & Lee, D.-H. Pairing near the Mott insulating limit. Phys. Rev. B 65, 054501 (2001).

[149] Boeri, L., Cappelluti, E., Grimaldi, C. & Pietronero, L. Poor screening and nonadiabatic superconductivity in correlated systems. Phys. Rev. B 68, 214514 (2003).

[150] Li, L. et al. Tuning the J_{eff}=1/2 insulating state via electron doping and pressure in the double-layered iridate $Sr_3Ir_2O_7$. Phys. Rev. B 87, 235127 (2013).

[151] Okada, Y. et al. Ripple-modulated electronic structure of a 3D topological insulator. Nat. Commun. 3, 1158 (2012).

[152] Shante, V. K. S. & Kirkpatrick, S. An introduction to percolation theory. Adv. Phys. 20, 325–357 (1971).

[153] Machida, A., Moritomo, Y., Ohoyama, K., Katsufuji, T. & Nakamura, A. Phase separation and ferromagnetic transition in B-site substituted $Nd_{1/2}Ca_{1/2}MnO_3$. Phys. Rev. B 65, 064435 (2002).

[154] Kim, J. W. et al. Dimensionality Driven Spin-Flop Transition in Layered Iridates. Phys. Rev. Lett. 109, 037204 (2012).

[155] Ge, M. et al. Lattice-driven magnetoresistivity and metal-insulator transition in single-layered iridates. Phys. Rev. B 84, 100402 (2011).

[156] Dai, J., Calleja, E., Cao, G. & McElroy, K. Local density of states study of a spin-orbit-coupling induced Mott insulator Sr_2IrO_4. Phys. Rev. B 90, 041102 (2014).

[157] Žutić, I. & Das Sarma, S. Spintronics: Fundamentals and applications. Rev. Mod. Phys. 76, 323–410 (2004).

[158] T. Dietl, D. D. Awschalom, M. Kaminska, and H. O. Spintronics. Elsevier Science, 2008.

[159] Fu, L. & Kane, C. Probing Neutral Majorana Fermion Edge Modes with Charge Transport. Phys. Rev. Lett. 102, 216403 (2009).

[160] Pesin, D. & Balents, L. Mott physics and band topology in materials with strong spin–orbit interaction. Nat. Phys. 6, 376–381 (2010).

[161] Yang, B.-J. & Kim, Y. B. Topological insulators and metal-insulator transition in the pyrochlore iridates. Phys. Rev. B 82, 085111 (2010).

[162] Wan, X., Turner, A. M., Vishwanath, A. & Savrasov, S. Y. Topological semimetal and Fermi-arc surface states in the electronic structure of pyrochlore iridates. Phys. Rev. B 83, 205101 (2011).